

**Understanding the Effects of Multi-scale Surface Roughness on the Contact Properties of
Hard-Material Interfaces**

by

Luke A. Thimons

Bachelor of Science, University of Pittsburgh, 2016

Submitted to the Graduate Faculty of the
Swanson School of Engineering in partial fulfillment
of the requirements for the degree of
Doctor of Philosophy

University of Pittsburgh

2021

UNIVERSITY OF PITTSBURGH

SWANSON SCHOOL OF ENGINEERING

This dissertation was presented

by

Luke A. Thimons

It was defended on

October 27, 2021

and approved by

Jung-Kun Lee, Ph.D., Professor, Department of Mechanical Engineering and Materials Science

Kurt Beschorner, Ph.D., Associate Professor, Department of Bioengineering

Qihan Liu, Assistant Professor, Ph.D., Department of Mechanical Engineering and Materials
Science

Dissertation Director: Tevis D.B. Jacobs, Ph.D., Assistant Professor, Department of Mechanical
Engineering and Materials Science

Copyright © by Luke A. Thimons

2021

Understanding the Effects of Multi-scale Surface Roughness on the Contact Properties of Hard-Material Interfaces

Luke A. Thimons, Ph.D.

University of Pittsburgh, 2021

Adhesion between rough surfaces is an important property of interfaces and is one that has far-reaching implications. Decades of experimental and theoretical work on the topic of adhesion between rough surfaces has been carried out. Yet no comprehensive understanding has emerged of the complex relationship between surface roughness and adhesion. From early measurements and models treating surfaces as nominally smooth to modern attempts to capture the fractal nature of real surfaces, we have yet to develop a robust connection between roughness and adhesion. This work focuses on clarifying the complicated relationship between surface roughness and dry adhesion, specifically in hard materials with tech-relevant applications. Experimental measurements of large-scale adhesion on a custom micro-mechanical tester are paired with extensive roughness characterization, spanning many orders of magnitude in size. Together, these give insight into fundamental parameters of interfacial interactions, and shed light on which scales of roughness play the most significant role in adhesion in different conditions.

There are three primary scientific contributions from this body of work. *First*, an in-depth analysis is presented of how to describe and characterize multi-scale roughness. Specifically, an analysis was performed (described in Chapter 3) of three commonly used metrics (the power spectral density, the autocorrelation function, and variable bandwidth methods), and their advantages and disadvantages of describing surfaces for the purpose of prediction of surface properties. *Second*, an experimental analysis was performed into the roughness-dependent adhesion between technologically relevant coatings, nanocrystalline diamond and aluminum oxide

(ruby), to determine which length scales most strongly control adhesion. Specifically, this work has revealed a larger-than-expected interaction range for these surfaces, and a limited range of size scales that contribute most significantly to adhesion. *Third*, the scientific understanding of roughness-dependent adhesion is advanced by lithographically patterning surfaces into silicon to intentionally vary different size scales and determine the contribution of each. The results from this last investigation underscore the importance of size scale in linking topography to adhesion and demonstrate how interatomic interactions determine the range of size scales that impact adhesion.

Table of Contents

Preface..... xix

1.0 Introduction..... 1

**1.1 The Critical Role of Surface Roughness and Adhesion in Engineering Applications
 3**

1.2 The Relevance of Surface Roughness 4

1.3 Origins of Adhesion 5

1.3.1 Atomic Bonding.....5

1.3.2 Electrostatic Forces.....6

1.3.3 Van der Waals Forces7

1.3.4 Capillarity8

1.4 Modelling of Adhesion and Roughness..... 10

1.4.1 Hertz and the Foundation for Contact Mechanics11

1.4.2 DMT, JKR and the Description of Adhesive Contact12

1.4.3 Greenwood and Williamson and the Description of Rough Surfaces15

1.4.4 Other Descriptions of Rough Contacts16

1.5 Roughness as a Multi-scale Phenomenon..... 19

1.6 State of the Art: Adhesion Measurement and Roughness Characterization..... 21

1.6.1 Multi-scale Surface Roughness Characterization21

1.6.2 Adhesion.....23

1.6.2.1 AFM Adhesion 23

1.6.2.2 Adhesion Testing Using the Surface Force Apparatus 26

1.6.2.3 Centrifugal Adhesion.....	27
1.7 Open Research Questions	27
1.8 Novelty of this Work	29
1.8.1 Optimizing Roughness Length-scale Sensitivity	29
1.8.2 Multi-scale Roughness Characterization	30
1.8.3 Creation of Intentionally Rough Surfaces	31
1.9 Hypothesis and Objectives.....	32
2.0 Methods.....	33
2.1 Micromechanical Measurements	33
2.1.1 Micromechanical Testing with a MEMS-Based Force Probe.....	33
2.1.2 Custom Micromechanical Tester.....	36
2.1.3 Test Environment.....	37
2.1.4 Testing Procedure	38
2.2 Interpretation of Results.....	39
2.3 Roughness Characterization.....	40
3.0 Describing Multi-scale Roughness: Power Spectral Density, Autocorrelation, and the Variable Bandwidth Method	42
3.1 Chapter Overview	42
3.2 Introductions and Motivation	43
3.3 Relating Multi-scale Roughness to Contact Properties	45
3.4 Analysis Methods.....	46
3.4.1 VBM	46
3.4.1.1 Intro and Schematic	46

3.4.1.2 Calculations	47
3.4.2 ACF	48
3.4.2.1 Intro and Schematic	48
3.4.2.2 Calculations	48
3.4.3 PSD	49
3.4.3.1 Intro and Schematic	49
3.4.3.2 Calculations	50
3.5 The Use of These Methods to Extract Roughness Parameters.....	51
3.5.1 Hurst Exponent	51
3.5.2 Extracting RMS Roughness Parameters	52
3.6 Results and Discussion: Applying Scaling Analysis to Synthetic and Real Surfaces and Profiles.....	54
3.6.1 Characterizing Self-Affine Topography: Extracting Hurst Exponents, and Detecting the Short- and Long-Wavelength Limits	54
3.6.2 Detecting the Start and End of Self-Affinity: The Long-Wavelength “Roll- Off” and the Short-Wavelength “Cut-Off” Region	57
3.6.3 Evaluation of the Hurst Exponent.....	59
3.7 Characterizing Other Common Topographic Factors: Crystallographic Facets, Surface Steps, and Reentrant Surfaces	60
3.7.1 The VBM.....	61
3.7.2 The ACF.....	63
3.7.3 The PSD	64
3.8 Step Functions.....	64

3.8.1 The PSD:	65
3.8.2 The ACF:	65
3.8.3 The VBM:	66
3.9 Accurately Describing Reentrant Surfaces	68
3.10 Characterizing Common Topographic Artifacts: Measurement Noise and Tip-Radius Artifacts	68
3.10.1 Synthetic Surfaces with Intentionally Designed Measurement Noise and Radius Artifacts.....	68
3.10.2 Real Experimental Surfaces with Measurement Noise and Radius Artifacts	70
3.11 Conclusions	73
4.0 Hard-Material Adhesion: Which Scales of Roughness Matter?	75
4.1 Chapter Overview	75
4.2 Introduction	76
4.3 Diamond Substrates	78
4.4 Methods	80
4.4.1 Experimental Adhesion and Topography Measurements.....	80
4.4.2 Numerical Analysis of Results.....	84
4.5 Experimental Results	86
4.6 Discussion	90
4.6.1 Effective Work of Adhesion and the Application of Classical Rough-Adhesion Models	90
4.6.2 Intrinsic Work of Adhesion and Range of Adhesion	91

4.6.3 The Role of Permanent Shape Change in Adhesion of These Contacts.....	96
4.6.4 Determining the Most Relevant Length-Scales of Roughness	98
4.6.5 Implications of the Present Findings.....	102
4.7 Conclusions	105
5.0 Controlling Dry Adhesion Through Multi-Scale Surface Texturing Via Grayscale	
Lithography	106
5.1 Chapter Overview	106
5.2 Introduction	107
5.3 Limitations of Prior Work and Remaining Open Questions.....	107
5.4 Methods	109
5.5 Results.....	111
5.5.1 Topography Results	111
5.5.2 Adhesion Results, Measured and Numerical Calculations	112
5.5.3 Roughness Parameters Extracted from Measured Surfaces	114
5.6 Discussion	115
5.6.1 Correlating Adhesion Force to Conventional Roughness Metrics	115
5.6.2 Fundamental Properties of the Interface	116
5.6.3 Understanding the Length Scales Governing Macroscopic Adhesion	118
5.6.4 Probing the Effects of Small-scale Roughness.....	120
5.7 Conclusions	122
6.0 Conclusions from Published Works	123
6.1 The Importance of Multi-scale Roughness Analysis	123
6.2 In Some Cases, a Specific Range of Scales Controls Adhesion	124

6.3 Fundamental Material Properties of Interfacial Interactions and Contact Properties	
Determine Length Scales Relevant to Adhesion	125
7.0 In Process and Future Work.....	126
7.1 Study of Permanent Shape Change in Patterned Surfaces	126
7.2 Friction: Sphere on Flat.....	127
7.3 TEM Analysis of Patterned Surfaces.....	128
7.4 Future Directions.....	129
Appendix A Single Sheets of Graphene for Fabricating Fibers with Enhanced	
Mechanical Properties	131
Appendix A.1 Chapter Overview	131
Appendix A.2 Introduction.....	132
Appendix A.3 Results and Discussion.....	135
Appendix A.4 Conclusions.....	140
Appendix A.5 References.....	147
Appendix B Custom micromechanical tester probe calibration	152
Bibliography	153

List of Tables

Table 1	microdevices classification. Produced with information from [2]	2
Table 2	Hurst exponents used to generate the synthetic profile above and the Hurst exponent extracted for each profile by each method	59
Table 3	Hurst exponents extracted from the euclidian profile using each of the VBM, ACF, and PSD. *the extracted value for the VBM depends on detrending (discussed in section 3.7.1). The theoretical or ideal Hurst exponent is also given	61
Table 4	Hurst exponents extracted from real surfaces	72
Table 5	RMS roughness values calculated from AFM data only (top) and also from the full-spectrum roughness data, including topography data from stylus, AFM, and TEM measurements of the same surfaces	87
Table 6	Adhesion values for the sinusoidal patterns with corresponding standard error .	113
Table 7	Results of ANOVA test with Tukey HSD post hoc test. Adhesion from each surface is compared and the correponding p-value is reported.... Error! Bookmark not defined.	
Table 8	RMS parameters extracted from the PSD of each of the sinusoidal patterns	114
Table 9	Designed amplitudes and wavelengths for each of the sinusoidal patterns	119

List of Figures

Figure 1	Examples of liquid capillarity in the presence of liquid at an interface and elastocapillarity at a dry interface. The elastocapillary length, L_s, is related to γ_s, surface energy and E, the elastic modulus.....	10
Figure 2	Schematic representation of DMT-like and JKR-like contacts.....	13
Figure 3	Schematic representation of a rough surface according to the Greenwood and Williamson model.....	15
Figure 4	Comparison between the Rumpf model (left) and the modifications by Rabinovich assuming that the asperity is part of a sinusoidal surface (right). Reproduced from [23].....	18
Figure 5	schematic representation of the multi-scale nature of roughness.	19
Figure 6	Schematic representation on an adhesion test using a standard AFM tip (LEFT) and a colloidal probe tip (RIGHT).....	24
Figure 7	Schematic of the MEMS-based force probe and the XYZ control stage with a microsphere attached to the end of the probe	33
Figure 8	The test setup used in adhesion testing. A simple schematic of the tip on substrate geometry (A), an optical image of a mounted sphere (B), a schematic of the typical shape and scale of an array of adhesion tests (C), and a typical force-displacement curve	35
Figure 9	Testing setup for contact tests depicting the thumbscrew stage (A), the piezoelectric actuator (B), the cantilever with spherical probe attached (C), the capacitive sensor (D), and the corresponding controls (E).	36

Figure 10 Example of adhesion dependence on time (left) and position (right). The results shown show no clear changes over the course of the 12 hour testing session..... 39

Figure 11 Schematic representation of the variable bandwidth method applied to a surface profile 47

Figure 12 Schematic representation of the autocorrelation function applied to a surface profile 48

Figure 13 Schematic representation of the power spectral density applied to a surface profile 50

Figure 14 Synthetic, self-affine profiles with varying Hurst exponents..... 56

Figure 15 The VBM (left), PSD (middle), and ACF (right) applied to each of the four synthetic profile shown in figure 15 57

Figure 16 The euclidian profile analyzed and the corresponding VBM (left), PSD (middle), and ACF (right)..... 61

Figure 17 The height profile for the synthetic surface with $H = 0.5$, original (black) and with steps introduced (red) and the VBM, ACF, and PSD for a stepped profile (RED) and the unstepped profile (black) 67

Figure 18 The height profile for the synthetic surface with $H = 0.75$ (black) and the same profile with white noise added (red) and the VBM, ACF, and PSD for surfaces with white noise introduced..... 69

Figure 19 A representative AFM image of ultranocrystalline diamond (top left) with a linescan extracted along the dashed black line, the extracted height profile (top right), and the VBM (lower left), the PSD (lower middle), and ACF (lower right). 71

Figure 20 Schematic diagram of the growth of diamond films using CVD. Reproduced from [97]..... 79

Figure 21 AFM measurements of the four polycrystalline diamond substrates (a-d) and one instance of a ruby sphere (e). The ruby sphere is also shown with its spherical geometry subtracted (f) to allow for direct comparison of roughness against the other surfaces..... 82

Figure 22 Experimental pull-off data is shown for the four substrates across different testing sessions (different colors) on a linear scale (a1-d1). The same data from panel a is combined into a single dataset and shown on a log-log plot (a2-d2), with log-normal distribution fitted to the data. 89

Figure 23 Computed pull-off forces were calculated by integrating an interaction potential over the combined roughness of the sphere and substrate (a). The best-fit value of range of adhesion was found by fitting to ratios of pull-off force (b), to eliminate the 93

Figure 24 The computed deformation for a single adhesion test is shown in panel (a) with the red and blue lines representing x and y direction line scans respectively. The actual deformation of the ruby sphere after an array of adhesion tests is measured using AFM images taken at the sphere apex before (b) and after (c) testing. The images have been precisely located at the apex of the tip where contact took place, and fiducial markers have been used to orient the image. The after-test image confirm the presence of permanent deformation, as is assumed in the numerical modeling, seems to be in order-of-magnitude agreement with what would be expected after 400 tests in different locations, each with the deformation shown in (a)..... 97

Figure 25 The contribution to pull-off force from various length scales can be directly demonstrated by recalculating pull-off force after filtering out small (a) and large (b) scales of roughness. Specifically, the pull-off force calculated from the filtered surfaces is normalized by the pull-off force calculated from the unfiltered surfaces. In panel (a), the x-axis indicates a short-wavelength cutoff, where all roughness below this size scale has been removed. A value near 1 indicates that there is almost no effect on pull-off force of filtering out roughness below that size scale. In panel (b), the x-axis indicates a long-wavelength cutoff, where all roughness above this size is removed. Here, a value of 1 indicates no contribution to pull-off force from roughness above that size scale 100

Figure 26 Lines scans from AFM of each patterned surface (A1-4), AFM scans of each patterned surface (B1-4), and the corresponding PSD for each (C1-4) 111

Figure 27 Adhesion measurements for the four sinusoidal patterns 112

Figure 28 RMS roughness parameters vs. pull-off force for the 4 sinusoidal patterns..... 115

Figure 29 Computed pull-off forces were calculated by integrating an interaction potential over the combined roughness of the sphere and substrate. The best-fit value of interaction range was found by fitting to ratios of pull-off force, to eliminate the absolute value of work of adhesion..... 117

Figure 30 Pull-off force between a smooth sphere of 250- μm radius (dashed black line) and a sinusoidal surface with peaks of different radius (solid black line). The far right of the plot represents contact between a sphere and a nearly flat sinusoid. The far left represents contact between a sphere and a very rough, but low amplitude sinusoid, essentially returning to a flat substrate..... 121

Figure 31 Normal force vs. friction force. The data is fitted with a linear trendline and the slope (the COF) is summarized in the legend. 128

Figure 32 Schematic of folding process for PMMA-coated graphene in an accordion-like pattern. Glass plates were treated with UV/O₃ prior to use. Wrinkles formed in the graphene sheet during compression along the width of the graphene sheet and remained folded as the sheet was compressed further. 141

Figure 33 SEM images of two graphene fibers. A suspended graphene fiber is shown after annealing on a copper substrate to remove its polymer backing. B, zoom in of graphene fiber from panel A (location marked with an arrow) is shown at a higher magnification and has a diameter of approximately 25 μm. C, a broken graphene fiber after tensile testing. Conductive silver paste was used to coat the mounting adhesive for SEM imaging. D, zoom in of graphene fiber from panel C, (location marked with arrow) showing the fracture edge after tensile testing. 142

Figure 34 Macroscale graphene fiber tested in uniaxial tension. A, optical image of graphene fiber ($A_{\text{graphene}} = 3.18 \mu\text{m}^2$, $L_{\text{fiber}} = 2952 \mu\text{m}$). B, Force-displacement plot of uniaxial tensile test (puller displacement rate $r_p = 0.50 \mu\text{m/s}$). This fiber exhibited brittle fracture, with a tensile strength of 0.475 GPa. 143

Figure 35 Uniaxial tensile testing of graphene fiber exhibiting ductile fracture. ($A_{\text{graphene}} = 1.84 \mu\text{m}^2$, $r_p = 0.50 \mu\text{m/s}$) Top: Three frames (1-3) of a graphene fiber uniaxial tensile test. (Frame 1) Graphene fiber ($L_{\text{fiber}} = 550 \mu\text{m}$) after straightening the macroscopic bends in the fiber; (Frame 2) Fracture initiation ($L_{\text{fiber}} = 612 \mu\text{m}$), (Position B); (Frame 3) Post-fracture ($L_{\text{fiber}} = 561 \mu\text{m}$). Bottom: Force-Distance plot (Left) of graphene fiber depicted in Top. A-B represents region of the stress-strain

curve (right plot) used to calculate the fiber modulus $K_{\text{fiber}} = 61.48 \text{ GPa} \pm 2.26 \text{ GPa}$. Point B refers to the fracture initiation of the graphene fiber. The maximum force at point C can be used to calculate breaking strength. The graphene fiber fractured in an unzipping pattern (see Video S2), which is also evident by the gradual (rather than immediate) reduction to zero force. Point D refers to the plateau region of force during unzipping of fiber. 144

Figure 36 Breaking strength of graphene fibers as a function of fiber length. Dotted arrows indicate order of sequential uniaxial tensile tests on the same fibers with $A_{\text{graphene}} = 3.2 \mu\text{m}^2$ (A) and $A_{\text{graphene}} = 5.2 \mu\text{m}^2$. (B). Green arrow indicates a measurement where ductile fracture behavior was observed during tensile testing..... 145

Figure 37 Breaking strength of parent and fragment fibers. Three fiber fragments exhibited ductile behavior and exhibited the largest measured breaking strengths. Brittle fracturing behavior was observed for most fibers. 146

Figure 38 Possible mechanism for the observed plateauing behavior in ductile fibers. The folded graphene region in is at high stress (left), causing crack formation. This crack arrests when it approaches the local low-tension region-- which is not folded and therefore under lower stress at the same extension. It is only after significant further extension of the puller (right), that the graphene reaches a sufficient stress to continue the propagation of this crack. During that extension, the load is thought to be constantly rebalancing between kinked portions, preventing catastrophic failure.146

Preface

I would like to thank my advisor Dr. Tevis D.B. Jacobs for his years of guidance and unending patience for experiments gone wrong, unexplainable data, and the rare late night spent fighting with that data.

I would also like to thank Dr. Lars Pastewka from the University of Freiburg for his close work on so many of my projects and his countless and meaningful insights. Our semi-weekly conference calls were a reliable source of motivation and inspiration. I am also deeply appreciative of all of the work Antoine Sanner, a member of Dr. Pastewka's group, has done over these years to aid me in all of my projects.

I would also like to thank the members of Dr. Jacobs' research group who have helped me so much and have been so willing to lend a hand. Thank you, Andrew, for all of the last-minute TEM images! Thank you, Nate, and Arushi for the endless supply of expertly taken AFM images.

I am thankful for the insights from my committee members and their willingness to offer guidance over these past months.

Finally, I would like to thank those friends and family members who might conceivably make it this far past the abstract. I will guess those few to be my mom and dad and my fiancé Carleigh. Thank you for your support!

I'll conclude with a favorite quote of mine from Wolfgang Pauli that I have come very much to agree with

“God made the bulk; the surface was invented by the devil.”

1.0 Introduction

The relevance of well-designed surfaces reaches every facet of modern life. Well-designed surfaces and interfaces are responsible for no small fraction of the comforts we enjoy today. Surfaces and interfaces are virtually ubiquitous. This fact alone warrants the meticulous design and careful study that has gone into surfaces. In the bronze age, weapons, jewelry, and metal vessels were polished to enhance their durability and luster [1]. This surface modification is highly effective in improving many properties. Coarse modifications such as these are sufficient to alter the properties of surfaces significantly. Thousands of years later, systems have grown significantly more complex and often much smaller. They require ever more control over the finest details of the interactions at and between surfaces. If we can understand how to tune surface properties efficiently and effectively, we can enable the creation of more reliable and longer lasting devices in a wide variety of fields. One area in critical need of optimized surfaces is the growing field of micro- and nanodevices.

Microdevices have seen significant adoption in mainstream applications and continue to penetrate new markets. A modern vehicle, for example, might have as many as 70 microdevices [2] and this number continues to grow. Many of these devices improve on the reliability and performance of older analog devices, other enable entirely new functionality. However, the functionality of many other novel microdevices is hindered by a few critical factors. Typical microdevices that have achieved full commercialization fall under the categories of class 1 and class 2. These classes are explained below in table 1. The information in this table is reproduced from [3].

Table 1 microdevices classification. Produced with information from [2]

Device class	features
I	no moving part
II	moving parts without rubbing or impacting surfaces
III	moving parts with impacting surfaces
IV	moving parts with impacting and rubbing surfaces

Devices which have seen high commercialization do not have surfaces that rub together or impact one another. Devices that do have such interactions often fail due to surface forces. These forces cause them to wear out too quickly or never function at all due to problems in fabrication [4]. These devices are held back by the overwhelming power of surface forces at small scales, and the problem only grows more dire as the scale of these devices continues to shrink. With smaller and smaller devices, we see surface forces becoming dominant factors in how these devices operate. Microdevices can be so small that their components may seem to be more surface than they are body! This leads to problems unique to these small systems. Stiction, for example, is the phenomenon of adhesion being so large that the driving force behind a component cannot overcome it, leading to the component locking in place and the failure of the device. This type of failure can come about after a run-in period or even during the fabrication process. How can this issue be eliminated? The answer is not clear. Numerous studies looking to connect surface roughness to adhesion have produced different, and often conflicting results [5]–[8].

This problem must be addressed by controlling the interactions between surfaces. By understanding how this interaction can be controlled, we can understand of how these devices can be optimized to function at the smallest scales possible. With this knowledge we can enable the creation new classes of devices on the small and large scales.

1.1 The Critical Role of Surface Roughness and Adhesion in Engineering Applications

While small-scale devices are poised to benefit greatly from optimized surface properties, there are many other fields that can share these benefits. And just as there are many fields that can benefit from optimal surface properties and interactions, there are many avenues towards controlling surface interactions. This work is focused on the connection between surface roughness and adhesion, specifically in hard materials. Hard materials like silicon, diamond, carbides, and oxides are used in applications such as bearings, seals, wear-resistant coatings, micro- and nanodevices, and many more. These hard coatings and components differ fundamentally in behavior from soft materials, which are not addressed in this work. While a soft material will conform to a countersurface and has large elastic deformation and often hysteretic behavior, hard materials will not. Harder materials will tend to have minimal deformation during contact and thus lack the ability to conform to a countersurface. This fundamental difference in contact behavior means that the two regimes of materials (a continuum in reality, the distinction is not always so clear between “hard” and “soft”) will have fundamental differences in how they interact with surface roughness.

All real surfaces exhibit some level of roughness, whether it is on the atomic-scale or is visible to the naked eye. In fact, many surfaces have roughness at both extremes and many scales in between. The problem of rough contacts is one that has sparked debate over the decades, as it is often far more complex than it might seem at first glance. The interfaces that govern everyday life are themselves controlled by the interactions of the surfaces on small scales. The question of how roughness affects contact properties has high relevance in any field where surfaces contact one another. This describes such a huge number of applications that solving the problem of relating surface roughness to contact properties is of incredible importance. The importance of the problem

of rough adhesion is only part of this larger picture, a complex part of an even more complex puzzle. The problem of adhesion in hard, rough contacts is a multi-faceted problem with no simple solution.

1.2 The Relevance of Surface Roughness

Surface roughness can arise from any number of sources, both controllable and uncontrollable. In small-scale applications such as wafer-level fabrication, complex shapes are created, and various topographies can be imparted onto the silicon surface. Some examples include nanopillar arrays, pyramids, and channels. These are examples of controllable roughness. On a slightly smaller scale, however, this control is lost. Are the surfaces of the etched silicon perfectly smooth, or do they have some roughness, and should we care what they look like? It has been demonstrated that different etching techniques do impart various levels of roughness on the wafer they etch [4]–[6]. One of the key questions this work proposes to answer is the relevance of such small-scale roughness. Is it truly critical that the smallest scales of surface topography be controlled, or does roughness have a diminishing effect on contact properties as it scales down? Whether it arises from controlled or unpredicted sources, small-scale roughness is present on all surfaces and its effects are the topic of ongoing exploration in the field.

Of course, it seems obvious that we should also place some focus on the scales of roughness that we can control. But do these larger scales have as significant an impact as the smaller scales? Perhaps they have an even greater impact. Given the extreme stiffness of hard materials, it seems feasible that the smallest scales of roughness will be sufficient to dominate the area of the contact (or the reduction of that area). If we assume that the contacts are nearly rigid, then would an atomic

scale bump not suffice to separate the surfaces from intimate contact and reduce adhesion? Throughout this work, the effects of different scales of roughness on adhesion will be interrogated and conclusions will be drawn as to which scales really matter in dry adhesion.

1.3 Origins of Adhesion

The fundamental physics of interatomic adhesion is a multi-faceted phenomenon. There are many different physical and chemical factors at play, all of which can influence adhesion. Some of these factors are the formation of bonds or capillary bridges at an interface, the presence of electrostatic forces, or the influence of Van der Waals forces. In this work, the contributions from Van der Waals forces are isolated, as these forces are the only ones that cannot ever be ruled out completely. Other factors must be taken into consideration, however. The following sections give a brief overview of the different attractive forces that contacting surfaces might feel.

1.3.1 Atomic Bonding

Bonding occurs between atoms in intimate contact. One type of bonding that can occur at contacts is covalent bonding. Covalent bonds form when the outer electron clouds of nearby atoms fully overlap, and the atoms share valence electrons. A perfectly covalent consists of atoms with identical electronegativity and thus has no polarity. These bonds are very strong and act over very short ranges. When bodies come into contact, they can form these bonds if their compositions allow for it. For example, in adhesion and friction tests involving silicon carbide on diamond (sp^3 carbon), it has been observed that the two surfaces formed carbon-carbon bonds at the interface,

leading to increased adhesion and friction [9]. This phenomenon is often reported with polymer contacts [10]. The attractive forces arising from covalent bonding act over very short range, on the order of atomic radii. These forces are considered to act only in areas of intimate contact between two surfaces.

Ionic bonding is similar to covalent bonding, in that the bond represents a very short-range interaction. This type of bonding occurs between atoms with very different electronegativities. Instead of the electron cloud being distributed evenly between the two atoms, the more electronegative atom pulls the electrons strongly towards it, resulting in a polar molecule. This type of bonding is not often reported in the field of contacts and their properties, but has been reported in the case of metal-ceramic contacts [11].

Another type of polar bonding that can occur at interfaces is hydrogen bonding. This type of bonding arises when a hydrogen atom is covalently bound to a more electronegative atom. A hydrogen bond generally forms between two hydrogen-containing dipolar molecules. In general, hydrogen bonding is only a real concern when specific measures are taken to impart a certain chemistry onto a surface [12] and when certain polymers are included in the contacts [13].

1.3.2 Electrostatic Forces

Electrostatic forces can also contribute to adhesion. This force arises from a charge differential between two surfaces. A typical example of this type of force can come from rubbing two insulating surfaces together and observe the effects of static electricity. These interactions are of significantly longer range than covalent bonding. There is generally no ‘rubbing’ involved in adhesion measurements, but such charges can still arise. The phenomenon known as contact charging (or tribocharging) occurs when insulating materials are brought into contact with one

another [14]–[17]. If there is a difference in work function between the two materials (or nearby atoms on each surface) there can be a transfer of charge. Although this transfer of charge may be extremely small, after repeated contacts in many sections of the surface, the effect may be measurable.

1.3.3 Van der Waals Forces

Unlike electrostatic forces or bonding, Van der Waals forces act between two atoms or molecules regardless of the composition or charge. These are induced-dipole forces. This means that two neutral atoms or molecules can interact with one another via Van der Waals forces. Spontaneous attraction arises when the electron clouds of the two atoms/molecules begins to interact with one another. The oscillation of electron fields around nearby nuclei creates fluctuations in charge in space. The result is a “syncing up” of the oscillations of the two electron clouds. If the two electron clouds are in sync with one another, they require some energy to pull apart. This phenomenon occurs not just between two atoms, but between all atoms of interacting surfaces. Most other sources of adhesion can be eliminated by various methods, but generally not Van der Waals forces. For this reason, many studies focus on this force, as it is the baseline force that must be dealt with in all cases. Van der Waals forces typically act over range of less than one nanometer.

A phenomenon known as Casimir forces, or retarded or relativistic Van der Waals forces, arises from the interaction described above. The interaction between the two electron clouds is travelling at the speed of light between the atoms. When the atoms are in close proximity, this interaction can be considered instantaneous. This instant interaction is described by standard Van der Waals interactions. As the atoms move apart, however, the finite speed of the interaction plays

a role. The electron clouds are not in perfect sync with one another. There is some lag, or a phase difference, between the oscillation of the two electron clouds. This results in a much weaker, but still present, attractive force that has been measured out to tens of nanometers on silicon-based devices [18].

1.3.4 Capillarity

Capillary forces arise from the presence of a liquid at an interface. When there is some liquid present, it can form capillary bridges between two surfaces. Depending on the surface energy of the liquid-gas-solid interfaces, these capillary forces can be attractive or repulsive. Without specific surface preparation, however, they are usually attractive in nature [19].

In practice, it can be difficult to eliminate capillary bridges. Ambient air typically has a relative humidity in the range of 20 – 50%. At these values, hydrophilic surfaces will have some adsorbed water layer. This layer can contribute to contact properties like adhesion by adding an additional attractive force between the interfaces. In typical adhesion experiments, capillarity is not desired as it complicates interpretation of the results. There are a few common methods used to eliminate this factor. The test can be carried out in a dry atmosphere. This will eliminate the adsorbed water layer to a degree but might leave some of the layer behind. A more reliable method would be to combine the dry atmosphere with a baking-out process to drive off any remaining water on the surfaces. Another common method is to perform measurements within a fluid. This eliminates the gas from the solid-liquid-gas interface and eliminates the possibility of capillary bridges forming. Testing in a fluid adds the complications of screening the Van der Waals interactions. Another form of capillarity that can arise between solids is called electrocapillarity.

Elastocapillarity is a phenomenon where an elastic material is deformed due to surface forces. It is similar to what happens when a liquid forms a capillary. In the case of liquids, the material can flow easily and thus is readily deformed by surface tensions. Similar processes can occur in solids. At an interface, two surfaces interact according to their respective surface tensions (or surface energies in the case of solids). Because solids can resist deformation, they cannot form such large capillaries as fluids. They can, however, form capillaries in some capacity. A solid's ability to form capillaries is described by its elastocapillary length. This value defines the length over which a material can be deformed by its surface energy and form a liquid-like capillary. This deformation would increase the contact area between two materials beyond what continuum mechanics would predict. A schematic of capillarity in rough contacts is shown in figure 1.

While liquid capillarity can be eliminated in experiments and in applications, elastocapillarity cannot. It is a property of the materials in the interface and will always be present to some degree. In the case of hard materials, this effect becomes negligible. The elastocapillary length describes the size of capillary bridges that can be formed. This length, L_s , depends on a material's surface energy and its elastic modulus.

Stronger surface energy and lower elastic modulus leads to longer capillary formation. Materials with very high elastic moduli have extremely low elastocapillary length. The elastocapillary length for ruby (a material used in this work) will be between $3\text{E-}13$ and $3\text{E-}12$ meters, well below the size of a single atom (around 0.1 nm or $1\text{E-}10\text{ m}$).

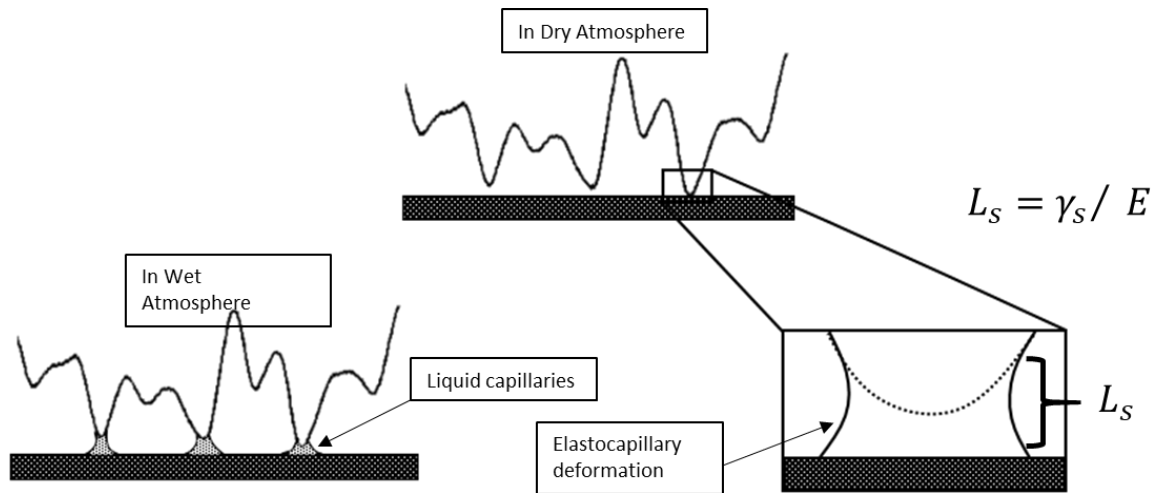


Figure 1 Examples of liquid capillarity in the presence of liquid at an interface and elastocapillarity at a dry interface. The elastocapillary length, L_S , is related to γ_s , surface energy and E , the elastic modulus.

Liquid capillarity is relatively easy to control. Elastocapillarity is a property of the interface. In the case of hard materials, elastic deformation due to surface energy is minimal. The present work uses extremely hard materials and as such, elastic deformations due to surface energy are not expected to play a role.

1.4 Modelling of Adhesion and Roughness

With these fundamental interactions in mind, we can begin to construct an understanding of how adhesion looks in real, rough surfaces. Starting from the earliest solutions for smooth contacts based in continuum mechanics to highly complex models based on fractal geometry, there have been many great contributions to the field. Each attempt at connecting surface roughness and adhesion relies of certain assumptions, some more physically reasonable than others. Throughout these next sections, some important contact models will be introduced and discussed in the context

of adhesion and multi-scale roughness. The first successful, quantitative attempts at modelling contacts came about with the solution to the problem of the contact between smooth, adhesionless spheres.

1.4.1 Hertz and the Foundation for Contact Mechanics

In 1882, Heinrich Hertz solved the problem of elastic contact between spheres. His classical solution forms the basis for the field of contact mechanics and is an integral part of many modern contact models [20]. Hertz' model gives us relationships between the applied load, contact area, normal and shear stresses, and deformations. Some results of the model are given in equations 1-1 through 1-3. These relationships form the basis for many future works on contact mechanics.

The model assumes contact between spheres; the problem of two spheres of radii R_1 and R_2 is shown to be equivalent to a flat surface in contact with a single sphere with an effective radius

$$R_{eff} = \left(\frac{1}{R_1} + \frac{1}{R_2} \right)^{-1} \quad (1-1)$$

The contact area between these spheres is defined by the contact radius

$$a = \left(\frac{3F_{applied}R_{eff}}{4E^*} \right)^{\frac{1}{3}} \quad (1-2)$$

The effective modulus, E^* , is defined by

$$E^* = \left(\frac{1 - \nu_1^2}{E_1} + \frac{1 - \nu_2^2}{E_2} \right)^{-1} \quad (1-3)$$

where ν_1 and ν_2 are the Poisson's ratios for each material in contact and E_1 and E_2 are their respective elastic moduli. The model gives simple, analytical equation for the radial and shear stresses and contact stiffness as well.

This model is based on continuum mechanics; therefore, it relies on certain assumption about the contacting bodies. The materials are assumed to be homogenous and isotropic in their material properties. The deformations must be smaller relative to the size of the bodies so that behavior can be approximated as scaling linearly with applied load. Finally, deformations must be elastic, as any irreversible deformation will not be predicted by the model. The model applies to sphere-on-sphere and sphere-on-flat geometries. It can be applied to crossed-cylinder in contact as well, which is equivalent to sphere-on-sphere contact.

1.4.2 DMT, JKR and the Description of Adhesive Contact

One contact property of consistent interest over the past decades has been dry adhesion. This property describes how surfaces attract one another in the absence of an intervening liquid. The Hertz model of elastic contact was extended by Derjaguin, Mueller, and Toporov [21] and by Johnson, Kendall, and Roberts [22]. These two groups offered extensions of the Hertz model that included adhesive forces in the contact. The DMT model was derived assuming Van der Waals attractions create adhesion contributions outside of the area of intimate contact. The JKR model, on the other hand, uses fracture mechanics to account for adhesion, balancing the energy expense of creating a new surface during pull-off with the energy gained from the deformed bodies returning to a zero-strain state. As such, adhesion occurs only in the area of intimate contact, unlike the DMT assumption where adhesion comes from the non-contacting regions. A simple schematic of these two types of contacts is shown in figure 2. Remarkably, although these two models take very different approaches in modeling adhesion, they arrive at the strikingly similar conclusion. Given below in equation 1-4 is the result of the two models that relate the pull-off force to the work of adhesion.

$$F_{pull-off} = C\pi R_{eff}W_{adh} \quad (1-4)$$

The functional form of the two models is identical. The only difference is that the DMT model has the constant C equal to 2, while the JKR model has it equal to 1.5. Here, $F_{pull-off}$ is the adhesive, or pull-off, force, C is a prefactor that depends on the model used, the effective radius, R_{eff} , describes the radii of contacting bodies, and W_{adh} is the work of adhesion between the two materials in the contact. Work of adhesion describes the energy per unit area needed to separate two surfaces. The force required to separate the surfaces can be converted conveniently to a work of adhesion assuming Hertz-like contact and that within the contact area, there is perfect contact.

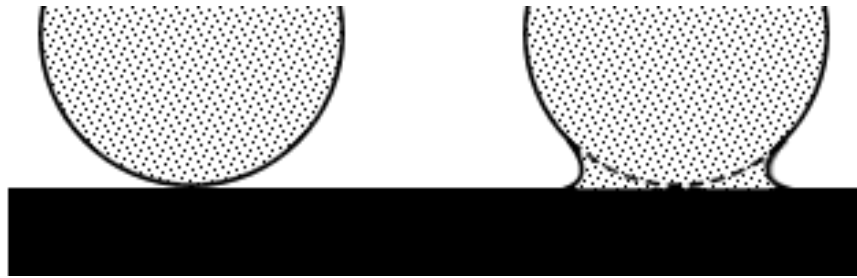


Figure 2 Schematic representation of DMT-like and JKR-like contacts

A debate arose as to which of these models correctly described the origins of adhesion and the behavior of adhesive contacts. Since the models describe adhesion in drastically different ways, it seemed unlikely that both of them described those same contacts. In 1992, Daniel Maugis argued that these two models are not at odds with one another, but rather represent the two extremes of a spectrum of contact behavior [23]. DMT represents behavior of very hard contact, while JKR describes softer contacts. The factor C varies monotonically between the two limits, 1.5 to 2 [24]. The models represent the first steps toward understanding adhesive contacts and allowed for a huge body of research to evolve from them.

The problem still existed, however, that these geometrically ideal models assumed perfectly smooth surfaces. These surfaces did not even atomic-level corrugation on the surface. While there was much experimental work that supported these new models, the problem remained that these models could not adequately describe rough contact. The problem arises that the area of contact is rarely a homogeneous area of intimate contact. Due to surface roughness, the true area of contact often differs greatly from the apparent area of contact that would be measured optically or calculated from one of these models. Calculating the work of adhesion from equation 1-4 assumes that the contacting materials are perfectly smooth. These smooth-contact models are adequate for describing contacts that are intentionally very smooth or are very large relative to their roughness. Real world surfaces are rarely, if ever, perfectly smooth. In order to advance the practical application of contact mechanics, a model that accounts for surface roughness was needed.

An important feature of large-scale adhesion studies is that they often report an effective work of adhesion. That is a value that is calculated from some model, the DMT or JKR for example, that does not take into account surface roughness. The effective work of adhesion, therefore, is dependent on surface roughness and will change between surfaces of the same chemistry but different topography. This value gives an idea of how the surfaces behave on the larger scale. A smoother surface, for example, might produce a larger adhesive force and thus will have a larger effective work of adhesion. This surface would appear “stickier” than a rougher surface having the same chemistry. In order to measure or calculate a true, or intrinsic, work of adhesion, the roughness must be accounted for.

1.4.3 Greenwood and Williamson and the Description of Rough Surfaces

Perhaps the most popular explanation of how real surface roughness affects contact was given by Greenwood and Williamson in 1966 [25]. The authors proposed a model for contact between a rough surface and a flat counter-surface. The model describes a surface as a series of bumps on an otherwise flat surface. These bumps, called asperities, are assumed to have hemispherical geometry at their peaks that is identical for every asperity on the surface. The height of each asperity is allowed to vary in this model. They are assumed to have heights defined by a normal, or gaussian, distribution. A schematic of a rough surface according to this model is shown below in figure 3.

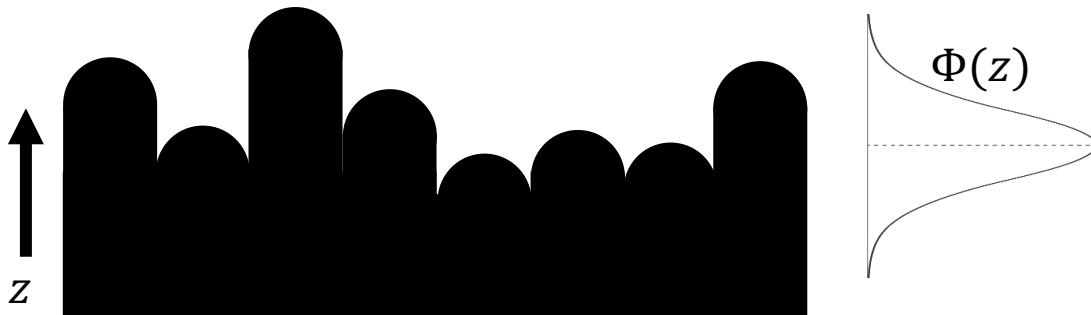


Figure 3 Schematic representation of a rough surface according to the Greenwood and Williamson model

The model assumes non-interacting asperities. That is, when one asperity is deformed, the neighboring asperities are not deformed. This assumption is reasonable when the tips of asperities are relatively far apart, an assumption which turns out to be reasonable for many real surfaces. The model relates loading, displacement, and contact area using various material and roughness parameters. The relationships described below in equations 1-5 and 1-6 are a direct result of the model.

$$P = \frac{4}{3}NE^*\beta^{\frac{1}{2}} \int_d^{\infty} (z - d)^{\frac{3}{2}}\Phi(z)dz \quad (1-5)$$

$$A = \pi N\beta \int_d^{\infty} (z - d)\Phi(z)dz \quad (1-6)$$

Where P is the total load, N is the number of asperities in contact, β is the radius of the asperities. z is the surface height and d is distance between surface mean planes. The function $\Phi(z)$ is the normal distribution that describes the asperity height distribution. In equation 1-6, A is the total contact area.

Equations 1-5 and 1-6 define the probability of finding an asperity at some height giving interplanar spacing. As the surfaces are brought closer into contact, more and more asperities come into contact. The roughness parameters that this model requires can be somewhat difficult to measure experimentally. The RMS height is defined as the standard deviation of surface heights and is a widely used and reported quantity. The asperity radius can be related to the RMS curvature of a surface. The RMS curvature is more difficult to determine experimentally. These models describe rough contact, but not rough, adhesive contacts. Greenwood and Williamson's description of rough contacts was extended to describe adhesive contacts in later years, however. In 1975, Fuller and Tabor applied the model to surfaces with JKR contacts [26] and in 1995, Maugis applied the model of surfaces with DMT contacts [27].

1.4.4 Other Descriptions of Rough Contacts

In 1992 Bush, Gibson, and Thomas introduced a model of rough contact that allowed for variation in asperity radius (often called the "BGT model") [28]. Instead of a surface having only

asperities of identical radii, this model allows for a distribution of asperity radii. The model also makes different arguments as to the relevant parameters for contact area predictions. While the G&W model requires that RMS height and curvature be known, the BGT model predictions rely primarily on RMS slope. Like the value for curvature, this value depends strongly on small-scale roughness. The analysis presented by the authors give a simple relationship between load and contact area for contacts at large interplanar spacing shown in equation 1-7.

$$\frac{F(d)}{A(d)} = \sqrt{\frac{m_2}{2}} E' \quad (1-7)$$

Where E' is the effective elastic modulus for the contact, m_2 is the second spectral moment of the surface profile, $F(d)$ is the load as a function of interplanar spacing, and $A_c(d)$ is the true area of contact as a function of interplanar spacing. This model requires integration not only across the distribution of summit heights, but also across the distribution on asperity radii. Thus, it is more difficult to apply and to determine the relevant inputs. The RMS slope is equal to the square root of m_2 ; this parameter depends most strongly on the smallest scales of roughness. This model, then, would predict contact properties that depend most strongly on that same smallest-scale roughness.

In 2000, Rabinovich published a pair of papers that addressed the issue of the difficulty of defining inputs for one specific contact model. He analyzed the Rumpf model, that makes prediction for nano-scale adhesion between a spherical tip and a hemispherical asperity. Rumpf's model assumes adhesion arises from two factors. The first comes from the contact between the tip and the asperity. The second comes from the interaction between the tip and the flat plane that the asperity sits on. Rumpf's original model requires the input of asperity radius, like other models do. This value is very difficult to determine for natural surfaces. Rabinovich offered a modification to the model that allowed for the asperity radius to be calculated from the easier-to-measure RMS

height (see figure 4). Below is a comparison between the original model and Rabinovich's proposed modification.

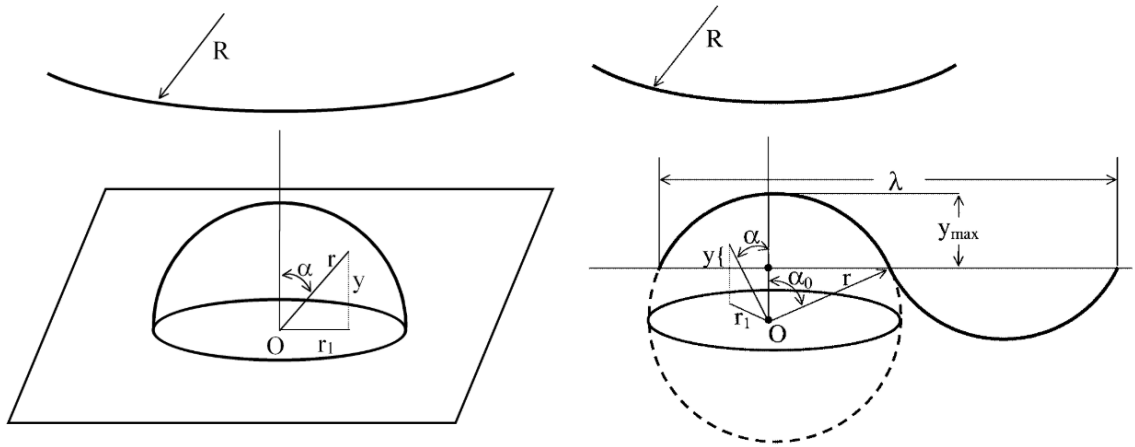


Figure 4 Comparison between the Rumpf model (left) and the modifications by Rabinovich assuming that the asperity is part of a sinusoidal surface (right). Reproduced from [23]

By approximating the asperity as part of a sinusoidal surface, the radius is conveniently related to the height of the asperity. Rabinovich goes on to describe how the model can be extended to account for multiple scales of roughness. By superimposing a smaller sine wave onto the larger one, a somewhat more realistic picture of surface roughness can be created. The issue is that the height of the smaller asperities must be known along with the larger one. In practice, it is not straightforward to try and separate a surface into two scales of roughness when in reality, there are many scales of roughness present. The determination of input parameters is a complicated problem. Real surfaces have roughness that is often not described well by hemispherical asperities. It has been shown that many naturally occurring surfaces have complex topographies that cannot be described by elliptical asperities (as proposed by Nayak [29]) or defined even by scalar parameters at all.

1.5 Roughness as a Multi-scale Phenomenon

Most complex surface topographies cannot be described by scalar parameters at all. When looking at surface roughness with, say, an optical microscope, you might see one picture of the shape of that surface. Under an electron microscope, the roughness may look entirely different. Which of these scales of roughness describes the surface then? As it turns out, many real-world surfaces have roughness that looks quite similar on very small scales as it does on larger scales. This property is called self-similarity. When we increase the magnification with which we look at something, the features that arise have the same shape as larger features. This concept defines the key feature of a fractal. The concept of fractal surface roughness was introduced by Benoit Mandelbrot in 1984 [30]. Figure 5 below gives a simple schematic representation of what multi-scale roughness might look like. A surface might look smooth to the naked eye, or even under a microscope. If the magnification is increased, features might start to arise and take the place of the smooth topography. Increase the magnification again, and still more features arise!

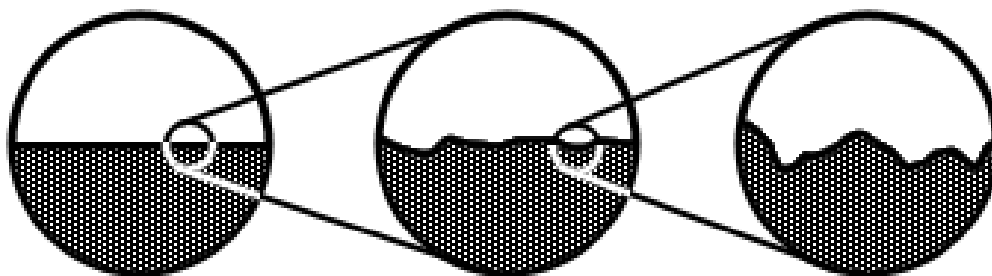


Figure 5 schematic representation of the multi-scale nature of roughness.

Traditionally, surfaces were described in terms of scalar parameters such as RMS height, RMS slope, and RMS curvature, but of course the computed values of those parameters would vary depending of which scale of Fig. 5 was used to compute them. Which of these images above gives the “correct” value of roughness? The answer lies not in merely choosing the correct

magnification, but in understanding surface roughness as being multi-scale in nature. With the introduction of multi-scale descriptions of roughness, our picture of rough surfaces becomes quite a bit more complicated. The critical takeaway from fractal-surface descriptions is that roughness on real surfaces is not confined to single scales. Many investigations have attempted to link surface properties to a single parameter, such as RMS height, or RMS slope, or possibly a combination of parameters [31]–[35]. However, the idea of multi-scale roughness calls that whole practice into question; any measurement of a scalar parameter will depend very strongly on which methods are used to measure the surface and to which length scales the measurement is sensitive.

For soft materials on multi-scale rough surfaces, B. Persson introduced a theory of rough adhesive contact based on fractal surfaces. This model is complex to apply, but essentially utilizes an energy balance between adhesive forces and elastic restorative forces [36]. This model applies to materials that can deform elastically and significantly during contact. Persson’s model should be applied to materials like polymers and not for hard materials like diamond and ruby.

For hard materials, there does not exist such a comprehensive, analytical model to describe the effect of multi-scale roughness on properties. Instead, it is common to use numerical analysis, where the true geometry of the surface is measured and then the interactions can be calculated. For example using limiting assumptions, such as that materials are rigid [37],[6] or that surfaces plastically deform fully [38], [39]. It is also common to assume that the surfaces will deform elastically and can be described by continuum mechanics. The contact deformation can then be implemented through a finite element method or boundary element method solver, as done in the work of Lars Pastewka and Mark Robbins and many others [40]. However, important questions remain about measuring surface roughness across all length scales and determining how to extract the relevant properties and connect this complex description of roughness to adhesion.

1.6 State of the Art: Adhesion Measurement and Roughness Characterization

The current field of adhesion measurements as well as roughness measurements is quite mature. There have been continual improvements and advancements in both fields over the past century, and these advancements have made new and exciting research possible. The following sections will introduce how adhesion and roughness are measured. Then we will look at how the present work aims to utilize and extend the state-of-the-art practices and instruments to gain new insight into the field of roughness and adhesion.

1.6.1 Multi-scale Surface Roughness Characterization

Atomic force microscopy (AFM) is the workhorse instrument for surface characterization. Offering extremely fine vertical and lateral resolution. An AFM can easily resolve features below 1 nm in height. The lateral resolution is limited by the radius of the tip. A typical lower limit for tip radius is around 10 nm, though they can be made much sharper and in some cases use single molecule tips to give extremely fine resolutions [41]. The vast majority of studies that aim to link adhesion to surface roughness use only AFM imaging [42]–[46]. This is a reasonable approach, given the general ease of access to AFMs and the wide range of surface features they can measure. However, an AFM in general cannot scan large enough sections of the surface to capture large-scale roughness. This is where an instrument like the stylus profilometer becomes very powerful.

Stylus profilometry offers the ability to scan over much larger areas than AFM. Most stylus profilometers can scan up to around 1 cm profiles. Many are limited to single line scans, but some offer 3D scanning capabilities. A primary drawback to this method is the fairly large tip radius. A larger tip radius means you must sacrifice sensitivity to small scales of roughness. Some

studies use only stylus data to analyze their surfaces [47][48]. These studies focus on larger scale roughness. Stylus profilometry is typically considered to measure a reasonable upper bound for scales of roughness. Much of the work in this field involves small-scale devices and interfaces. Although controlling roughness can be very difficult, controlling roughness on the mm to cm scale is very achievable. While stylus can be sufficient to measure a parameter like RMS roughness, much richer data can be extracted from any set of experiments when considering more scales of roughness.

Optical Profilometry is another popular choice for characterization of surfaces on larger scales. This method typically uses white light interferometry to measure changes in surface height. These machines offer extremely fine vertical resolution of around a few angstroms. Their primary drawback is the poor lateral resolution of 300-500 nm at best. Optical profilometry is very useful for determining step heights, but not so useful in determining lateral and vertical extents of small features. The diffraction limit of light determines the scales of roughness that can accurately be measured with this method.

Measuring roughness below what traditional AFM can measure becomes quite difficult. There have been many advancements made in AFM imaging and researchers have been pushing the edges of what an AFM can measure for some time. Still, most work linking contact properties to roughness use traditional AFM setups that offer great resolution, but do not offer information on single nanometer scales. In order to investigate smaller-scale roughness, probe-based methods must be abandoned. These methods are limited by the radius of the tip. Sharper tips give better resolution, but are prone to damage and wear, which complicate the data. A novel method for small-scale roughness characterization is used in this work and is described in section 1.8.2 and in refs [49][50].

1.6.2 Adhesion

1.6.2.1 AFM Adhesion

AFM studies are an excellent way to develop an understanding of asperity level interactions between two surfaces. The tip of an AFM probe will typically have a radius of a few tens of nanometers to a few hundreds of nanometers. A typical AFM adhesion study would involve bringing the AFM cantilever into contact with a material and then removing it, measuring the force experienced by the tip. This AFM tip contact is often considered to be free from the effects of roughness. Roughness below the scale of a sharp AFM tip would be extremely small. This allows for highly precise measurement of what might be called the true work of adhesion between two materials, as the entire area between the AFM tip and the substrate can be considered to be in intimate contact. This is very useful when determining fundamental material and interface properties but does not scale up very well. A material's true work of adhesion could be recreated by placing two atomically flat surfaces into contact, but this is rarely, if ever, the case in any large or even micro-scale application. In order to capture the behavior of real engineering materials and interfaces, larger contacts must be used.

Larger contacts came to AFM with the introduction of colloidal AFM experiments. In 1991, Ducker et al. [51] and Butt et al. [52] developed colloidal probe AFM by attaching small microspheres to the end of AFM cantilevers. The advantage this gives is a larger sampling area along with the inclusion of more length scales of roughness. In sampling a larger area, more than one asperity might be contacted. This allows for the measurement of an effective work of adhesion, that is, one that is affected by the surface roughness. Roughness will tend to sharply reduce the real area of contact in hard contacts. The advantages this technique offers are two-fold. First, it shifts small-scale adhesion measurements toward engineering applications. The larger contacts

capture a more statistical picture of the contact as opposed to a single asperity contact with traditional AFM. Second, the colloidal probes offer a method to evaluate the effects of roughness, which cannot readily be done when investigations focus single asperity contacts. A schematic comparison between a standard and a colloidal probe AFM is shown in figure 6.



Figure 6 Schematic representation on an adhesion test using a standard AFM tip (LEFT) and a colloidal probe tip (RIGHT)

Colloidal AFM studies involved affixing a small sphere, typically having a radius of a few microns to a few tens of microns, to an AFM cantilever. In 2005, Tormoen et al. showed how colloidal probe radius affects rough adhesion [53]. They found that adhesion behavior became more tightly defined as probe radius increased. This suggests that with larger spheres we see larger areas of contact. This in turn leads to capturing more statistics of the surface, which will draw the adhesion data toward the mean adhesion behavior. The study, however, only increased probe radius up to 40 microns. It is possible that much larger probes would measure a tighter range of adhesion as we begin to sample a more averaged contact region.

Similar experiments by Laitinen et al. in 2013 measured the effects of small-scale roughness on adhesion between alumina contacts [8]. Surface roughness was simulated by depositing alumina nanoparticles. It was found that increasing RMS roughness from 1.5 nm to 12 nm caused a five-fold decrease in adhesion. Tip radii in their work ranged up to 15 microns, on the same order as the particle diameter of the deposited powder. A primary limitation of this study

and many like it is that the tip radius is on a very similar scale as the asperity radius of the substrate. Although for very smooth surface, many asperities might be in contact, to gather more meaningful statistic on contact properties, even larger tests will be useful.

There are other studies that avoid this issue by controlling roughness by depositing nanoparticles onto a flat substrate. Ramakrishna et al. showed multi-asperity contact between a 20 micron diameter polymer sphere and a substrate coated with varying areal density silica nanoparticles ($d = 12 \text{ nm}$)[54]. This work showed similar finding to previous studies where decreasing particle density led to increasing adhesion. Studies like this reveal a fundamental limitation of colloidal AFM measurements. The small tip radius sets a limitation on the substrate roughness. If the roughness is too large (i.e. Beyond nanoparticle-on-flat levels) then multi-asperity contact cannot be established, and “statistical” contact cannot be measured. While we might or might not expect to see multi-asperity contact in larger-scale contacts, we do not want single-asperity contact to arise due to experimental limitations. Rather we would prefer to see it arise due to the properties of the contacting materials and their topographies.

More recently, sharp tip AFM adhesion has been extended to investigate the smallest-scale contacts. By inserting a sharp tip into a TEM, the mechanics of the contact can be interrogated in extreme detail. Such an investigation was done by Jacobs et al. in 2013 when nanoscale, in-situ adhesion measurements were performed in a TEM [55]. This allowed for unparalleled insight into the shape of the contacts and the nanomechanics within the contacting bodies. The type of experiment represents one extreme of contact testing, with clear focus on single-asperity contact and revealing asperity-level contact behavior. This knowledge is critical in predicting larger-scale contact behavior. Contacts on the large scale are, after all, governed by a series of asperities supporting the contact.

1.6.2.2 Adhesion Testing Using the Surface Force Apparatus

The surface force apparatus (SFA) provides a means to perform sensitive measurements on scales larger than those that an AFM can achieve. This test rig was first used by Tabor and Winterton [56] to measure Van der Waals forces between crossed cylinders. The crossed cylinder geometry is popular because thin-flat surfaces can be easily tuned for roughness and then bend into a cylindrical shape. The SFA predates AFM by about 15 years and enabled measurement of forces with displacement resolution down to a few angstroms. It achieved this through the use of multiple beam interferometry (MBI). Typical experiments involve sphere on flat contact tests or crossed cylinder tests. The SFA made its mark by allowing measurement of forces between surfaces at extremely small separations. Forces at separations as low as 1.5 nm have been measured using the SFA [57]. Because of the small separations, the surfaces typically used in SFA experiments must be extremely smooth. Atomically smooth mica surfaces are the go-to substrate for SFA experiments.

In Tabor and Winterton's work, the SFA that they devised allowed the surfaces to have a 1 cm radius of curvature with approximately 90 degrees of a full cylinder. This type of experiment represents a large increase in working size versus AFM. Isrealachvili made further advancements with the SFA (in the SFA Mk I – III) when he pioneered work modifying the SFA for use in liquid environments, allowing the measurement of lateral forces, allowing variable ranges of motion, and many more improvements [58]. The modern version of the SFA can achieve around 10 nN force resolution and single-angstrom vertical position resolution. These machines represent a very high standard of sensitivity and flexibility that enables measurement of surface forces for a wide variety of surfaces.

1.6.2.3 Centrifugal Adhesion

Many small-scale adhesion tests rely on controlling roughness by depositing nano- or microparticles on a flat substrate, another example of using powders to create roughness [59]–[62]. An important field of adhesion studies is that of powder adhesion. These studies aim to determine how the powders themselves adhere to different substrates rather than utilizing powders to create roughness. One popular method for measuring adhesion of powders is through the use of a spinning substrate. The substrate is spun, and the centrifugal force causes powder particles to spin off. The results often are reported in the form of angular velocity versus particles remaining on the substrate.

These studies offer built-in adhesion statistics because of the huge number of particles used in each test. Just like the colloidal AFM studies, however, these tests have limitations on the particle size. It is unclear at the time of writing if literature on centrifugal adhesion can be applied to the current project. The results reported for centrifugal adhesion do seem to have many similarities to the present work's results, especially in terms of the adhesion distribution measurements. Further investigation into possible connections between centrifugal adhesion and larger-scale tests is warranted.

1.7 Open Research Questions

Based on the aforementioned investigations four critical research questions emerge.

First, what are the best characterization approaches and metrics to provide accurate input data for the investigation and prediction of roughness-dependent adhesion? There has been a great deal of work that has gone into testing classical models of rough contact. The vast majority of

these investigations into the effects of roughness on contact properties opt for a single method of roughness characterization, most often a larger-scale technique such as stylus or optical profilometry. Based on what we know about the multi-scale nature of roughness, is a single method sufficient to capture the true shape of the surface? What range of scales needs to be covered to capture both atomic-scale interactions and macroscale contact geometry? Even beyond the best techniques to use, what are the optimal metrics for describing roughness and entering it into mechanics models for scientific understanding, model validation, or prediction of performance? It is clear from the introduction that simple scalar metrics (such as R_a and R_q) will typically be insufficient, but what are the advantages and disadvantages of the different multi-scale descriptors: the power spectral density, the autocorrelation function, and the variable bandwidth method?

Second, which length scales have the most significant impact on roughness? A recurring theme in most contact modeling is the requirement of scalar roughness parameters. These parameters depend very strongly on which length scales of roughness are used to calculate them. There is an underlying assumption in these models that the correct length scales are chosen when calculating input parameters. However, it is not always clear: Should we be more concerned with the nanoscale bumps on the surface, or with the larger features that those bumps sit atop? What length scales of roughness actually control contact properties?

Third, what are the micro- or nano-scale physical processes that are governing macro-scale contact behavior and thus determining which length scales of roughness are most significant? Why do certain scales of roughness matter? It is certainly of interest to understand if a certain scale of roughness matters, but this insight is much more powerful if we understand why it is the case. How do surfaces interact with each other, and how does roughness affect these interactions?

1.8 Novelty of this Work

This work builds on the standard roughness and adhesion measurements discussed in the previous section and extends and modifies them to offer new avenues toward understanding adhesion and roughness. The following sections discuss the novelty of this project in terms of instrumentation and experimental setups.

1.8.1 Optimizing Roughness Length-scale Sensitivity

Typical AFM adhesion studies measure interfaces on the scales of a few nanometers. Colloidal AFM studies are capable of measuring interfaces between spheres of up to a few tens of micrometers. Devices like the SFA are capable of measuring much larger interfaces while maintaining good force resolution, but lack the flexibility to perform sequential measurements on a variety of surfaces. The custom apparatus used in this work combines the flexibility of AFM measurements with the larger size scale of SFA. The probes used can handle up to millimeter-scale spheres while offering nanonewton force resolution. This gives us force resolution similar to AFM experiments while significantly expanding the length scales we are sensitive to. While some larger scale studies do offer a greater range of roughness length scale sensitivity, they often do so by sacrificing force resolution. The experimental setup in this work is designed to optimize length-scale sensitivity and force resolution.

1.8.2 Multi-scale Roughness Characterization

Not only do our measurements need to be sensitive to as many length scales as possible, but we also need to have information on those length scales in order to draw meaningful conclusions as to their effects. This is where most previous studies fall short. The vast majority of investigations into the effects of roughness on contact properties do not account for all scales of roughness. Most will choose one method of roughness characterization and report results from that method. This is a reasonable choice, but the conclusions from those studies might only be applicable to the specific range of roughness that was sampled in that measurement technique. The extensive roughness characterization in this work goes beyond what any previous adhesion studies have included. Roughness measurements on the AFM scale and larger are quite common. This work investigates not only these larger scales, but also much smaller, taking advantage of TEM-based measurements of angstrom-scale roughness. These measurements involve sectioning a sample and thinning it down to electron transparency. The process is described in ref [49].

This work combines adhesion measurements with extensive surface roughness characterization. Specifically, we aim to overcome the limitations of classical roughness measurements by considering the multi-scale nature of surface roughness. It has been shown that surface exhibit roughness across many length scales. When trying to calculate roughness parameters required for classical models, such as RMS height, slope and curvature, different length scales of roughness play different roles. The RMS curvature, for example is very strongly influenced by the smallest scales of roughness. This means that if you measure a surface with a stylus profilometer, you will calculate one value of curvature. If you were to measure the same surface with an atomic force microscope, you would calculate a very different, likely much larger value of curvature. Similarly, the height variation you would measure with these different

techniques would likely vary significantly. This work avoids the shortcomings of these single-technique roughness measurements by accounting for all scales of roughness and using a range of measurement techniques.

Multiple measurement techniques are used to compile comprehensive roughness data. Previous studies have not gone into such depth on roughness characterization, opting to use, in most cases, AFM to characterize their substrates. Through the measurement of all length scales of roughness, we are uniquely poised to interrogate the effects of each of the length scales that are present. The present work sheds light on the question of which length scales are relevant to rough adhesion

1.8.3 Creation of Intentionally Rough Surfaces

This work makes extensive use of the rational variation of topography for surfaces with similar chemistry. The two primary methods of surface roughness modification are: chemical vapor deposition (CVD) growth of nanocrystalline diamond, where growth conditions govern grain size, and therefore surface topography; and electron-beam lithography, where a computer-generated pattern of topography can be etched into a silicon wafer. These two methods can create a wide range of different types of roughness. The many different types of roughness analyzed in this work give the advantage of allowing us to interrogate the effects of different roughness shapes and scales and to develop broad insights into how roughness influences adhesion

1.9 Hypothesis and Objectives

The underlying hypothesis of this project is that adhesion is governed by roughness on many different scales and that there are certain critical scales that influence adhesion most strongly. Adhesion can be most efficiently and effectively tuned by the addition or removal of these critical scales. Furthermore, these critical scales can be predicted and depend on the fundamental material properties of the surfaces in contact.

This work aims to test that hypothesis by accomplishing the following objectives:

1. Test the ability of single-scale roughness parameters to predict dry adhesion
2. Determine specifically which scale or scales of roughness influence dry adhesion most strongly
3. Determine the fundamental properties of interfaces relevant to critical scales of roughness
4. Experimentally assess the role of different scales of roughness in influencing adhesion in hard materials

2.0 Methods

2.1 Micromechanical Measurements

2.1.1 Micromechanical Testing with a MEMS-Based Force Probe

Adhesion tests between spheres and flat substrates have been carried out using a force sensing probe coupled with a high-precision 3-axis linear actuator. The majority of adhesion characterization work was carried out using a MEMS-based probe (FT-S microforce sensing probe, FemtoTools, Buchs, Switzerland). The probe was mounted to the linear actuator (FT-MA02, FemtoTools, Buchs, Switzerland). The combination of the force probe and actuator offer completely modular test setups. The probe offers normal force measurements with nanonewton resolution, and the actuator offers x-y-z motion with nanometer resolution. A simple schematic of a typical test is shown in figure 7. For a typical adhesion test, a microsphere is glued to the end of the force probe.

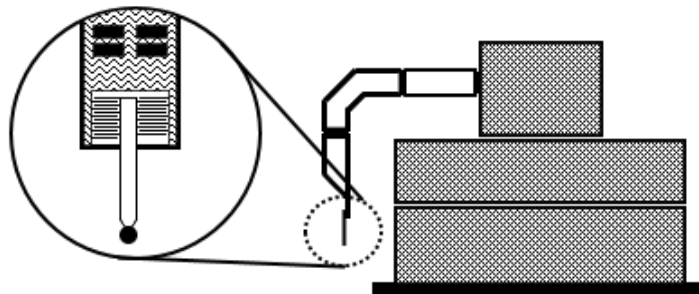


Figure 7 Schematic of the MEMS-based force probe and the XYZ control stage with a microsphere attached to the end of the probe

The tester shown uses a MEMS force sensing chip that relies on electrostatic forces between a comb-drive-like capacitor. The arm has three degrees of freedom, each one actuated by a piezoelectric stick-slip actuator. It should be noted that all motion done during measurements is restricted to the ‘sticking’ portion of the actuator’s motion. The motion is limited to just under 2 microns of travel. Larger scale movement, such as that between testing sites, is accomplished by the traditional stick-slip motion.

The spheres used in testing are polished prior to any adhesion measurements. From the manufacturer, the spheres usually have roughness on the order of a few tens of nanometers RMS height. The spheres are polished down to an ultrasmooth finish using an alumina slurry (0.05 μm). Once polished, the spheres maintained their original radius but had an RMS height of below 1 nm, as measured in an AFM over a scan size of 5 μm . This polishing was critical for measuring adhesion values. The roughness of an unpolished tip is far larger than the roughness of many of the substrates tested. The spheres are glued into the end of the force probe, shown in figure 8b using Crystalbond (Crystalbond 509, Aremco, Valley Cottage, Ny, USA). The sphere shown in figure 8b is a ruby sphere (B0.50R, SwissJewel, Philadelphia, PA) with radius 250 μm .

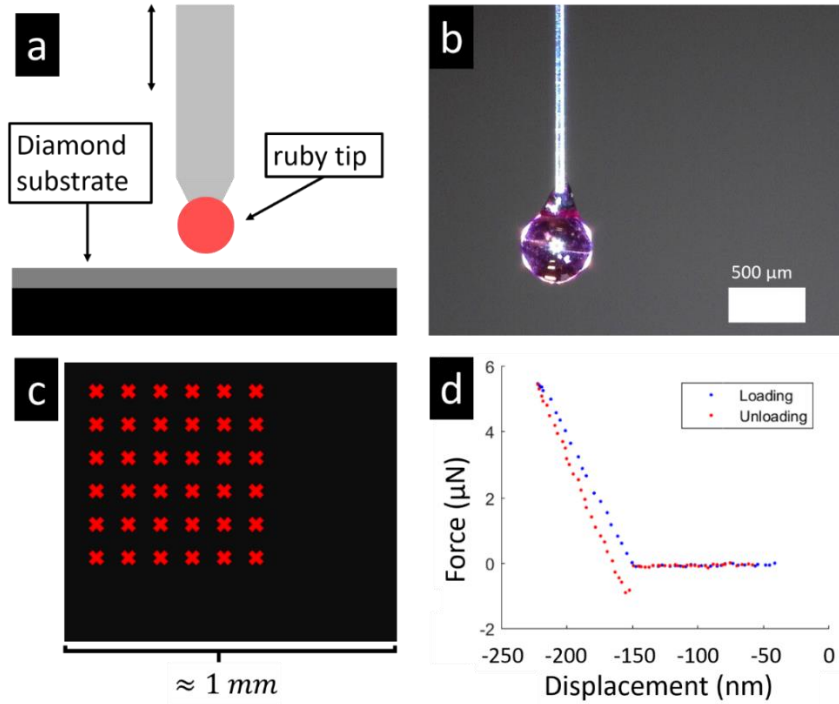


Figure 8 The test setup used in adhesion testing. A simple schematic of the tip on substrate geometry (A), an optical image of a mounted sphere (B), a schematic of the typical shape and scale of an array of adhesion tests (C), and a typical force-displacement curve

Once positioned over the substrate, the tip is brought into contact (see figure 8a and 8b). The arm is lowered until the sensor reaches some user-defined preload. After this, the vertical scanning motion is started and a displacement controlled, load-limited test is done. The tip is loaded onto the substrate up to some load, and is then withdrawn, producing data on the force, time, and position in all three axes during the loading and unloading segments (figure 8d).

A critical aspect of the tests in this research is the reproducibility of the data. Given the extremely small forces being measured, any unaccounted-for time-dependent effects had to be eliminated. Such drift effects can arise from deformation on the tips or the substrate, from humidity or temperature fluctuations, or different noise levels throughout the day. Adhesion measurements were repeated many times for each substrate in a way that did not depend only on time.

2.1.2 Custom Micromechanical Tester

In addition to the MEMS-based force sensing setup, another tester is used at various points in the work. This micromechanical tester is built from the most basic components and is completely customizable in terms of its shape and capabilities. Below, figure 9 gives a schematic representation of the tester.

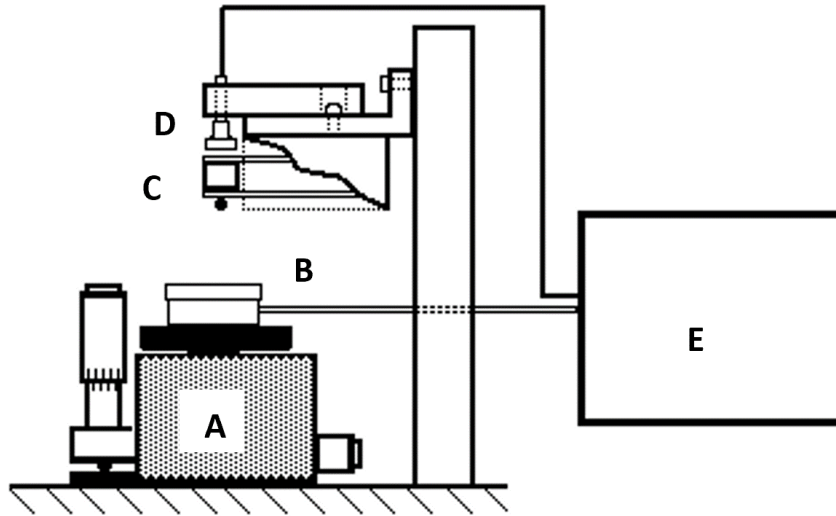


Figure 9 Testing setup for contact tests depicting the thumbscrew stage (A), the piezoelectric actuator (B), the cantilever with spherical probe attached (C), the capacitive sensor (D), and the corresponding controls (E).

This test rig offers the distinct benefits of extreme flexibility and high durability (the MEMS-based force probes are exceptionally fragile and cannot tolerate any lateral loading). This micromechanical tester functions in a similar way to the MEMS-based tester. Tensile and compressive loads can be measured with micronewton sensitivity. The tester consists of a piezoelectric stage (figure 9b) that controls fine motion with sub-nanometer position resolution. The piezoelectric stage is placed on top of a coarse positioning stage (figure 9a), a manual thumbscrew stage or a linear actuator. The force sensor consists of a cantilevered beam (figure 9c)

that sits just below a capacitive displacement sensor (figure 9d). The piezoelectric stage and capacitive sensor provide feedback to the LabView-based control software. See appendix B for details on probe calibration.

The flexibility of this tester allowed for diverse mechanical testing to be carried out beyond adhesion measurements. For example, Appendix A details a separate investigation performed during my PhD work that investigated the tensile strength of graphene ropes. This custom tester was used in conjunction with linear actuators and custom LabView-based control software to measure the tensile properties of these ropes. While that investigation is tangentially related to the primary topic of this thesis (in that interfacial defects and fracture play a role in both the adhesive separation of contacting surfaces and the cohesive failure of graphene structures), it is included only in an Appendix to avoid distraction from the primary scientific advancements in the field of roughness-dependent adhesion.

2.1.3 Test Environment

All adhesion testing was carried out in an environmental control chamber. The chamber consists of metal walls, acrylic windows, and various feedthroughs for electrical components. The windows of the chamber were covered in aluminum foil to create a faraday cage. This ensured that our sensitive measurement equipment was not influenced by stray electromagnetic signals. The chamber sits on a large air-table. This helps to eliminate vibrational noise from the building. Finally, the chamber is filled with dry air prior to all testing. While the effects of humidity on adhesion have been studied, and are of considerable interest, they are not within the scope of the present work. The goals of this work are to quantify the effects of roughness on dry adhesion, eliminating as many confounding variables as possible. To eliminate the influence of capillary

forces, the tests were carried out in a dry atmosphere. Dry air was flowed into an environmental control chamber and the humidity was monitored continuously. The tests were performed once the humidity fell below 1%, the measurement floor of the sensor. However, it was confirmed in separate testing that adhesion tests performed slightly above that range had little effect on the results.

2.1.4 Testing Procedure

Prior to testing, each of the substrates is cleaned in various alcohols. The substrates are sonicated in isopropyl alcohol, acetone, and then methanol. After sonication they are blown off with dry nitrogen and then placed into the chamber. The cleaning of the tip is a less reliable process. The needle-like force sensing probe is extremely fragile. Once the tip is mounted onto the force probe, it cannot be cleaned easily without risking breaking the tip. The spherical tip is cleaned by sonication in alcohol prior to mounting. After mounting, the tip is imaged with optical profilometry to ensure the absence of residues. The force sensing probe is placed in the test chamber, which is then sealed with a small outlet left open to allow for dry air to be flowed into and out of the chamber.

Once the chamber is sealed and filled with dry air and the humidity reading is at or below 1%, the tip is lowered onto the substrate. The test is carried out according to the process described in section 2.1.1. A set of 400 contacts will typically span over about 12 hours.

2.2 Interpretation of Results

The data for a single contact is shown in figure 8d (above). From the Force-Displacement or the force-time plot, we extract the pull-off force. This is the only piece of data we are interested in for this work. Since the tests span over several hours, we want to ensure that there are no time-dependent effects. Looking at pull-off force vs. time data or pull-off force vs. position data can shed light on any time-dependent effects. Figure 10 shows typical test data, where the adhesive force shows no consistent trends with time or position on the sample.

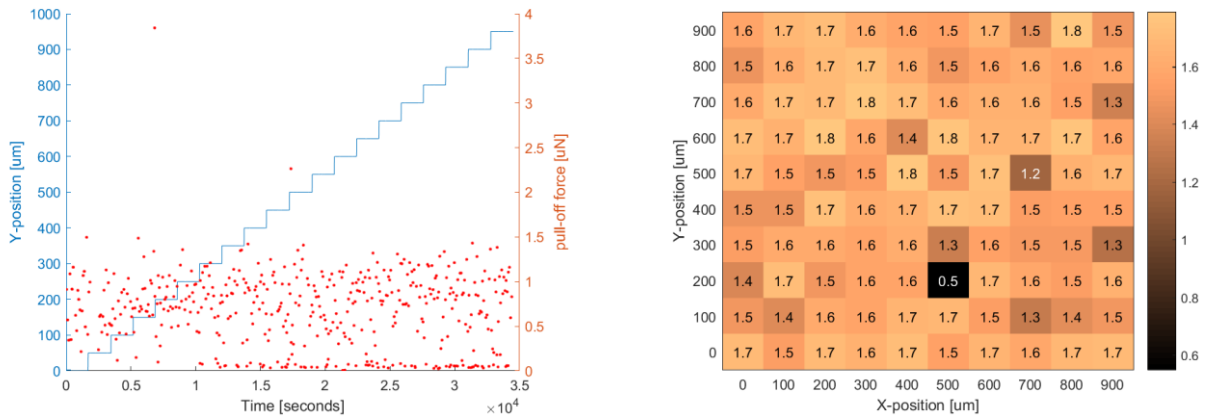


Figure 10 Example of adhesion dependence on time (left) and position (right). The results shown show no clear changes over the course of the 12 hour testing session.

The absence of position dependent effects is also a good indicator that we are in fact, sampling enough of the substrate to capture an averaged contact. This confirms that we are capturing larger areas than small-scale tests would.

2.3 Roughness Characterization

The surfaces were characterized using stylus profilometry, atomic force microscopy (AFM), and transmission electron microscopy (TEM). Stylus profilometry, along with atomic force microscopy, are contact-based techniques, in which a sharp tip is scanned across the surface and senses relative height variations. Stylus profilometry allows for line-scans to be taken of surfaces of interest with lengths up to tens of millimeters. This is the largest scale of characterization we investigate in this work. While larger scales could be analyzed, the surfaces analyzed do not have any roughness features above these scales. This technique is limited on the small-scale by the size of the tip. The stylus will generally have a tip radius of around 5 μm . This means that any features with curvature smaller than approximately 5 μm cannot be sampled by a tip of that radius.

The AFM has become a workhorse of surface measurements. It operates on principles similar to the stylus profilometer. It has the key advantages of offering 2D imaging, using much sharper tips, and thus offering far greater resolution than the stylus. The AFM can scan areas of up to a few hundred microns and can achieve resolutions down to a few nanometers. One very important advantage of combining techniques is the ability to self-check our multi-scale characterization methods. Between the tens-of-microns stylus tip and the hundreds of microns AFM scan size, we have significant overlap. This allows us to confirm that the two measurements give overlapping results. On the small-scale end, the AFM, like the stylus, is limited by tip radius. This method allows us to achieve resolutions down to a few nanometers.

Finally, we use TEM to characterize the absolute smallest scales of roughness. The AFM alone will not suffice if we want to be able to make concrete statements about precisely which scales of roughness are relevant to certain contact properties. Unlike the two previous methods,

the TEM is not typically used for measurements of surface roughness. In this work we use the TEM to look at cross sections of each of our surfaces. The results of this characterization are reported in works by Khanal, Gujrati, and Vishnubhotla [49], [63]–[65]. This method gives us roughness data ranging from a few nanometers down to the angstrom scale and gives us the most complete insight into the multi-scale nature of surface roughness. Note that while the analysis of TEM results was performed by the present author, the TEM measurements themselves were performed by other collaborating graduate students in the Jacobs Research Group.

3.0 Describing Multi-scale Roughness: Power Spectral Density, Autocorrelation, and the Variable Bandwidth Method

3.1 Chapter Overview

A predictive understanding of roughness-dependent surface properties requires a complete description of the surface topography. Real surfaces have multi-scale surface topography, with smaller-scale roughness superimposed on top of larger-scale roughness – in many cases, extending from the component scale (centimeters) down to the atomic scale (angstroms). However, this multi-scale roughness *does not* typically obey the simple scaling relationships of fractals, such as self-similarity or self-affinity. Therefore, such surfaces cannot typically be described by a single parameter (such as average roughness or fractal dimension). Instead, these surfaces require spectral characterization, where the magnitude of roughness is measured independently at every size scale. The present investigation evaluates three common spectral analysis techniques: (1) the variable bandwidth method (VBM); (2) the autocorrelation function (ACF); and (3) the power spectral density (PSD). These analyses are performed on a collection of multi-scale experimental measurements of topography on ultrananocrystalline diamond as well as on several synthetic profiles. The purpose of this analysis is to review all three techniques and compare their strengths and weaknesses. All three techniques offer similar information on the fractal characteristics of roughness, extracting similar hurst exponents for real and synthetic surfaces. The PSD is best equipped to identify geometric features, such as facets and surface steps, and can be used on 1D data (line scans) and 2D data (area scans). The VBM and ACF generally cannot provide as much insight into areal, 2D data, typically being limited to line scans in a certain direction. The VBM

has the advantages of simpler interpretation and the ability to be applied to reentrant surface profiles, whereas the PSD and ACF require well-defined functions (one height value for every spatial position). However, the VBM focuses only on RMS height, while the PSD and ACF enable the calculation of RMS slope and curvature as well. Finally, the ACF seems to give the best estimate of the scales above which there is no roughness, or the roll-off region. Overall, there is no single method that gives a wholly complete and accurate analysis for all surfaces; instead, each multi-scale analysis technique has different strengths and shortcomings. By applying all three techniques and comparing extracted scaling quantities, we can learn about the type of roughness present and distinguish between truly fractal surfaces and other common, special cases of roughness.

3.2 Introductions and Motivation

Surface interactions control performance in many engineering applications, from atomic bonding at interfaces in coatings and machine contacts to large-scale friction in vehicle brakes. Surface topography plays a critical role in determining surface properties, and thus in controlling performance in applications from microfabrication [66][67] to energy storage [68] to optics [69][70] to biological surfaces[71], and others [72]. Recent advances in improving performance in these areas are closely tied to understanding and controlling surface topography. However, while the ability to measure, describe, and model surface topography has become quite advanced, there are still many unanswered questions. A comprehensive understanding of surface topography requires not only theoretical understanding of the surface topography, but also descriptions of complex, real-world surfaces that are accurate and comprehensive.

Most surfaces, if not all, have topographic features on many different length scales, which is referred to as multi-scale roughness. Early work by Mandelbrot [30], [73] examined real surfaces using fractal geometry and showed that many surfaces appear to be self-similar or self-affine over some range of length scales. This behavior manifests, for example, as a power spectral density that is a power-law of the wavevector [74]. However, more recently, it has been shown that many real surfaces appear self-affine only over a certain range of sizes, and typically have more complex size scaling when the whole range of sizes are considered. For example, at large scales, a roll-off regime may be observed where the PSD is relatively constant, while at smaller sizes other scaling regimes arise due to crystallographic faceting or nanoscale morphology. A comprehensive description of topography over all scales is required in order to describe friction [75], [76], fluid sealing [77], [78], and surface adhesion [79][80].

A comprehensive characterization of a surface involves making measurements of surface topography with methods such as stylus profilometry, optical profilometry, atomic force microscopy, cross-section electron microscopy, or other techniques. Each individual measurement contains height information about one location, over a finite range of size scales (from the pixel size to the scan size), with whatever artifacts are imparted by that instrument or technique. In other words, each measurement provides a partial and imperfect picture of the surface topography. A complete picture of surface topography requires a large number of measurements, at various sizes, locations, and instruments, combined into a single descriptor. In a prior publication from the Jacobs group,[74] the power spectral density (PSD) was presented as one way to do this combining. Here we compare and contrast three such methods: the PSD, the autocorrelation function (ACF), and the variable bandwidth method (VBM).

3.3 Relating Multi-scale Roughness to Contact Properties

The properties of an interface are primarily governed by two factors: the material properties of the surfaces in contact, including surface chemistry and mechanical properties; and the surface topography. For a given surface chemistry, tremendous effort has gone into understanding the relationship between surface roughness and contact properties. While early attempts used simple, scalar roughness descriptors, recent efforts account for all scales of roughness, and therefore require more comprehensive descriptors. Bo Persson has developed a contact theory describing contact area, adhesion, sealing, and friction of soft materials, utilizing the power spectral density to describe key parameters such as the stored mechanical energy across all length scales [76], [78], [81], [82]. Wang and Müser provide an analysis of the ACF, drawing connections between the height-difference ACF and interfacial properties such as stresses and contact area [83]. The ACF has also been used in various forms to model and predict contact geometry [84], adhesion [85], coating grain size [86].

The purpose of this chapter is to assess the strengths and weaknesses of three scaling analysis methods—PSD, ACF, and VBM—in combining multiple topography measurements and assessing measurement artifacts. There have been several useful works comparing different multi-scale analysis methods [87]–[90], which have demonstrated how different methods perform in extracting fractal quantities from both synthetic and measured surfaces and profiles. The purpose of the present investigation is to specifically assess the strengths and weaknesses of three different techniques in accurate detection of key topographic features, including: the large-scale roll-off region, the small-scale cutoff of roughness, the fractal dimension and Hurst exponent, reentrant features, and noise.

3.4 Analysis Methods

3.4.1 VBM

3.4.1.1 Intro and Schematic

The variable bandwidth method, also called the roughness-length method, is a simple way to analyze surface roughness at different scales. The VBM quantifies how the computed RMS height of a profile varies with the size of the sampling window. Using this method, the RMS height, or the standard deviation of heights, of a profile is calculated across a certain sampling window, or bandwidth. A small bandwidth can capture only the smaller scales of lateral size, which tend to have smaller height variation, thus resulting in a small average RMS height. A larger sampling window captures larger scales of roughness, which tend to have larger height variation, and will be more representative of the true RMS height computed by considering the whole profile with infinite resolution. Variable bandwidth analysis can be carried out on a single measurement, or across different measurements collected at various scales. In the case of an areal measurement, such as that from a typical AFM scan, the VBM can be calculated for each raster line. In Gujrati et al. [64] many individual surface profiles were measured and then analyzed this way using the VBM.

For a given profile, the bandwidths will range from the length of two pixels up to some fraction of the full length of the profile, typically half of the profile length [89]. The schematic in figure 11 and equations 3-1 and 3-2 detail the calculation of the VBM.

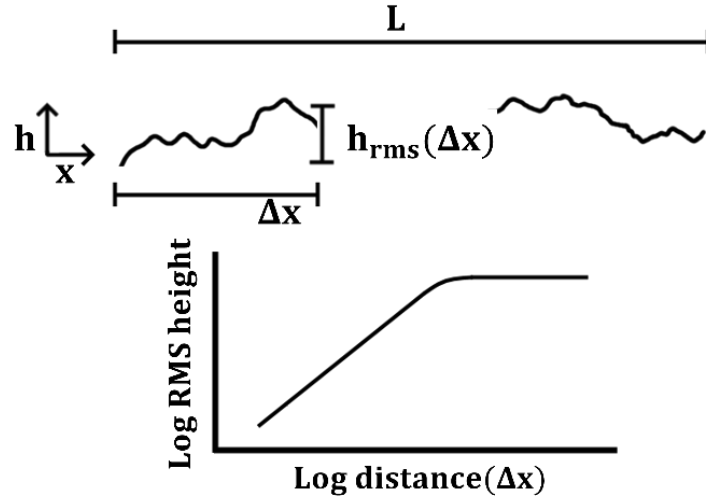


Figure 11 Schematic representation of the variable bandwidth method applied to a surface profile

While the most straightforward application of the VBM is on 1-dimensional profiles, it can be applied 2-dimensionally as a function of Δx and Δy , but this approach is not detailed here.

3.4.1.2 Calculations

The VBM is calculated using a sliding window. Essentially, a window of size Δx starting at position x_0 is scanned across the profile and a value of RMS height is calculated at every value of x_0 . The standard deviation of heights (the RMS height) for each window is averaged, indicated by the angled brackets in equation 3-1. Equation 3-2 gives the calculation of the RMS height.

$$VBM(\Delta x) = \langle h_{rms}(\Delta x) \rangle_{x_0} \quad (3-1)$$

$$h_{rms}(\Delta x) = \left[\frac{1}{\Delta x} \int_{x_0}^{\Delta x} h(x)^2 dx \right]^{\frac{1}{2}} \quad (3-2)$$

3.4.2 ACF

3.4.2.1 Intro and Schematic

The height-difference autocorrelation function (ACF), also called the variogram method [91] or the structure function [92], describes how a dataset correlates to itself when the profile is shifted laterally by a varying distance. When the data is shifted by a small amount Δx , the height difference between datasets is necessarily small. As the shift gets larger, the variance becomes larger until some saturation point is reached. This saturation point is related to the roll-off regime, see section 3.6.2. The schematic in figure 12 and equation 3-3 details the calculation of the ACF

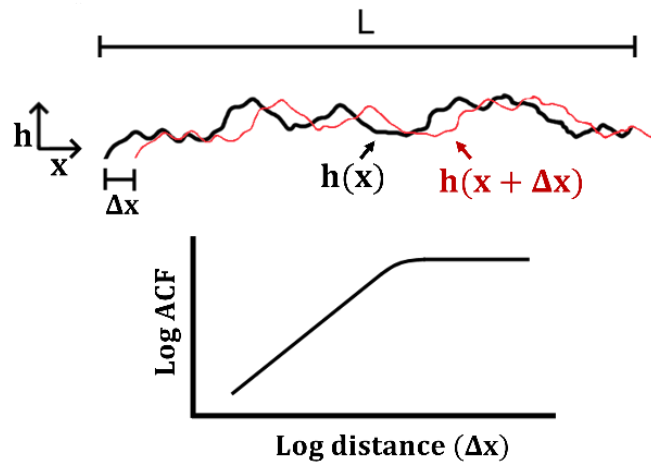


Figure 12 Schematic representation of the autocorrelation function applied to a surface profile

3.4.2.2 Calculations

The ACF is applied to a single profile using equation 3-3. The calculation takes a profile $h(x)$ and a shifted profile $h(x + \Delta x)$ as inputs. The square of the difference between each overlapping datapoint in the original and shifted profiles is calculated and averaged. This gives an average, absolute height difference between the two profiles.

$$ACF(\Delta x) = \frac{1}{2} \langle \{h(x) - h(x + \Delta x)\}^2 \rangle_x \quad (3-3)$$

Where x outside of the brackets denotes an average taken over all values of x . The ACF is generally applied to profiles. A 2D calculation can also be performed, shifting an areal scan in x and y .

3.4.3 PSD

3.4.3.1 Intro and Schematic

The power spectral density represents a surface in frequency space, rather than real space, as in the ACF or VBM. A comprehensive description of the PSD is given in [53], and therefore only a brief summary is included here. A surface is broken down into a summation of sinusoidal components via the Fourier transform. Each component has a certain wavelength, phase, and amplitude. Because the PSD is the square of the Fourier transform, the phase information is lost. A theoretical surface composed of one or a few distinct sinusoidal components would produce a PSD with sharp spikes at the frequencies of those sine waves; however, real surface can be described by sine waves over a continuum of frequencies, as depicted in figure 13 below. Each sinusoidal component can be described by a frequency, or wavelength, and an amplitude. The PSD can give an idea of the relative frequencies and amplitudes of the roughness scales present in a profile. Figure 13 presents the PSD as a function of wavelength. The PSD is typically presented (and calculated) as a function of wavevector. It is shown here in terms of wavelength for ease of comparison with the VBM and ACF.

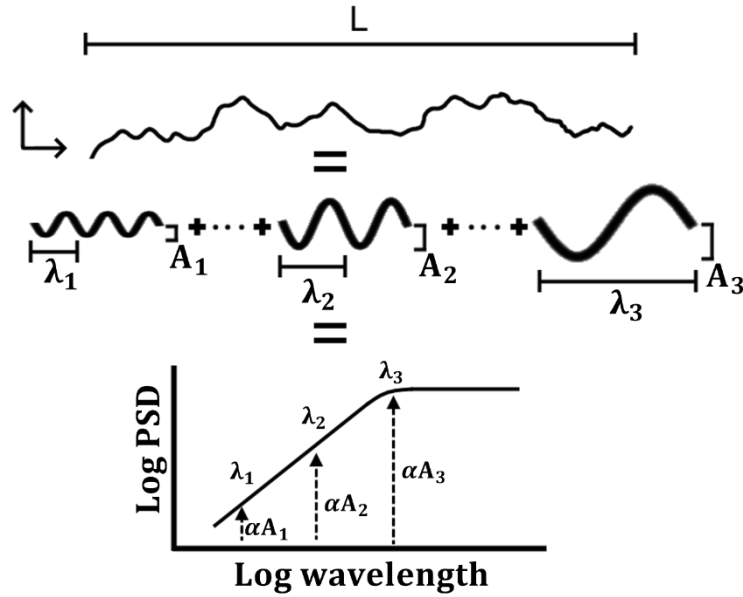


Figure 13 Schematic representation of the power spectral density applied to a surface profile

3.4.3.2 Calculations

The PSD is calculated from the Fourier transform of the height profile in equation 3-4 below

$$\hat{h}(x) = \int_0^L h(x) \exp(-iqx) dx \quad (3-4)$$

Where $h(x)$ is the height profile along x and q is the wavevector with units of inverse distance, since we are not working in the time domain, but rather the distance domain. The wavevector is related to its real-space counterpart, the wavelength by $q = 2\pi/\lambda$. The PSD is calculated as the square of the Fourier transform and is commonly normalized by the length of the profile, L_x in equation 3-5.

$$PSD = \frac{1}{L_x} |\hat{h}(x)|^2 \quad (3-5)$$

Where L_x is the length of the measured profile. Unlike other methods, the calculation of the PSD requires a periodic profile because of its use of the Fourier transform. To compute the PSD of typical, non-periodic topographies, the surface is windowed, most commonly by multiplying through by part of a cosine function that is zero-valued at the end points. A drawback of this method is that any data near the edges of the line scan is weighted less than data in the center of the scan, though this should not have a significant impact on randomly rough surfaces where all locations are statistically identical.

3.5 The Use of These Methods to Extract Roughness Parameters

3.5.1 Hurst Exponent

Each of these multi-scale analysis methods can identify distinct regions of size scale, which may have self-affine behavior or may deviate, for example in the “roll-off” region (see section 3.6.2). The profiles analyzed in this investigation all have a self-affine region, which is typically present for most real surfaces, at least over some range of size scales. In this region, the magnitude of the curve has power-law scaling, which appears linear on a log-log plot. For 1D analyses, the scaling in this region is related to the Hurst exponent by equations 3-6, A through C.

$$PSD \propto q^{-1-2H} \quad ACF \propto \Delta x^{2H} \quad VBM \propto \Delta x^H \quad (3-6A, B,C)$$

3.5.2 Extracting RMS Roughness Parameters

A critically important feature of these methods is the extraction of common roughness parameters from them. While scalar roughness parameters do not fully describe a surface, they are important partial descriptors and the ability of these methods to extract these quantities is important. The VBM offers the most straightforward way to extract one scalar roughness parameter, the RMS height. Since the standard deviation of heights at a given size scale is the definition of the VBM. Equation 3-7 gives the RMS height for a surface by the value of the VBM at the maximum bandwidth sampled.

$$h_{rms} = VBM(\Delta x) \text{ for } \Delta x \rightarrow \infty \quad (3-7)$$

The ACF is not quite so straightforward but does allow the extraction of both the RMS slope and RMS height. Just like the VBM, when the ACF is calculated across a large distance, e.g., the entire length of a scan, the value is equal to the square of the RMS height. When the distance over which the ACF is calculated is set to the pixel size the RMS slope can be calculated.

$$h_{rms} = \sqrt{ACF} \text{ for } \lambda \rightarrow \infty \quad (3-8)$$

$$h'_{rms} = \frac{\sqrt{2 ACF}}{\lambda} \text{ for } \lambda \rightarrow 0 \quad (3-9)$$

Where λ is the wavelength, or the amount of shift between the profiles.

The PSD offers perhaps the most complete picture of roughness parameters. The RMS height, slope and curvature can all be extracted using Parseval's law from the zeroth, second, and fourth spectral moments of the PSD. By integrating over the entire spectrum of frequencies (zero to infinity below), the RMS height (h_{rms}), slope (h'_{rms}), and curvature (h''_{rms}) are calculated.

$$(h_{rms})^2 = \frac{1}{\pi} \int_0^{\infty} PSD(q) dq \quad (3-10)$$

$$(h'_{rms})^2 = \frac{1}{\pi} \int_0^{\infty} q^2 PSD(q) dq \quad (3-11)$$

$$(h''_{rms})^2 = \frac{1}{\pi} \int_0^{\infty} q^4 PSD(q) dq \quad (3-12)$$

where q is the wavevector. These RMS parameters can be calculated at any scale of interest by varying the bounds of integration. In addition to calculating RMS roughness parameters, the PSD can also offer insight into the specific wavelengths and amplitudes of roughness present on a surface. The PSD can be thought of as revealing the amplitude of roughness at a given wavelength or frequency. Equations 3-13 through 3-18 details these calculations. This scale-dependent amplitude can be computed by rearranging the equations from Ref. [74] section A.1.

For a 2D surface, the discrete inverse Fourier transform can be written as

$$h(x, y) = \frac{1}{L_x L_y} \sum_{q_x, q_y} \tilde{h}_{q_x, q_y} e^{i(q_x x + q_y y)} \quad (3-13)$$

The pre-factor to the exponential term gives us the amplitude for a given frequency. The amplitude can be related to the magnitude of the PSD by

$$PSD_{q_x, q_y}^{2D} = A^{-1} \left| \tilde{h}_{q_x, q_y} \right|^2 \quad (3-14)$$

Where A is the area of the 2D data. The equations can be combined to relate amplitude to the PSD

$$amplitude = \frac{\tilde{h}_{q_x, q_y}}{A} = \sqrt{\frac{PSD_{q_x, q_y}^{2D}}{A}} \quad (3-15)$$

For a 1D profile, the inverse Fourier transform can be written as

$$h(x) = \frac{1}{L_x} \sum_{q_x} \tilde{h}_{q_x} e^{i q_x x} \quad (3-16)$$

The pre-factor to the exponential term gives us the amplitude. The amplitude can be related to the magnitude of the PSD by

$$PSD_{q_x}^{1D} = L_x^{-1} |\tilde{h}_{q_x}|^2 \quad (3-17)$$

The equations can be combined to relate amplitude to the PSD

$$amplitude = \frac{\tilde{h}_{q_x}}{L_x} = \sqrt{\frac{PSD_{q_x}^{1D}}{L_x}} \quad (3-18)$$

PSD analysis can be applied to a 1D profile, or a 2D topography. Here, we focus on the 1D PSD and analysis of a 1D profile. A 2D surface can be analyzed by the 1D PSD by treating the surface as a group of 1D profiles, or it can be analyzed as a surface using the 2D PSD.

3.6 Results and Discussion: Applying Scaling Analysis to Synthetic and Real Surfaces and Profiles

In the following analysis, these three different approaches will be applied to synthetic self-affine profiles, as well as measured experimental surfaces, in order to assess their strengths and weaknesses in detecting various artifacts and topographic features.

3.6.1 Characterizing Self-Affine Topography: Extracting Hurst Exponents, and Detecting the Short- and Long-Wavelength Limits

In order to evaluate the characterization of self-affine profiles, we created and analyzed a set of computer-generated, synthetic surfaces. Synthetic roughness profiles allow us to control certain specific parameters and test how different multi-scale characterization methods quantify

each profile. For this purpose, synthetic line scans were generated here with 32,768 datapoints (2^{15}), representing a physical length 512 nm. The Hurst exponent is fixed at four different values, 0.25, 0.5, 0.75, and 1. The RMS slope and height are allowed to vary. The short wavelength cutoff is 4 nm (256 px) and the long wavelength cutoff is 256 nm (16,384 px). The short wavelength cutoff refers to the wavelength below which there are no scales of roughness present. The long wavelength cutoff refers to the wavelength above which there are no roughness scales present. Most real surfaces exhibit a long wavelength cutoff very clearly. The short wavelength cutoff is often obscured by noise.

The Hurst exponent is an important parameter describing self-affine fractal surfaces, which can be related to the fractal dimension [74], and describes the correlation between points in a series. In general, for any signal, a high Hurst exponent (max of 1 for a line profile) indicates a stronger correlation between one value in a series and the next; for instance, if the height difference between two adjacent points is positive, then the height difference to the next point is more likely to also be positive. A Hurst exponent of 0.5 represents no correlation between subsequent height differences, which is described as a ‘random walk’. A Hurst exponent between 0 and 0.5 indicates a negative correlation between adjacent height differences, with a positive value more likely to be followed by a negative one. As the Hurst exponent goes from 0.25 to 1 in figure 14, the profile maintains its overall shape, but the correlation between nearby datapoints becomes stronger and the profile appears smoother.

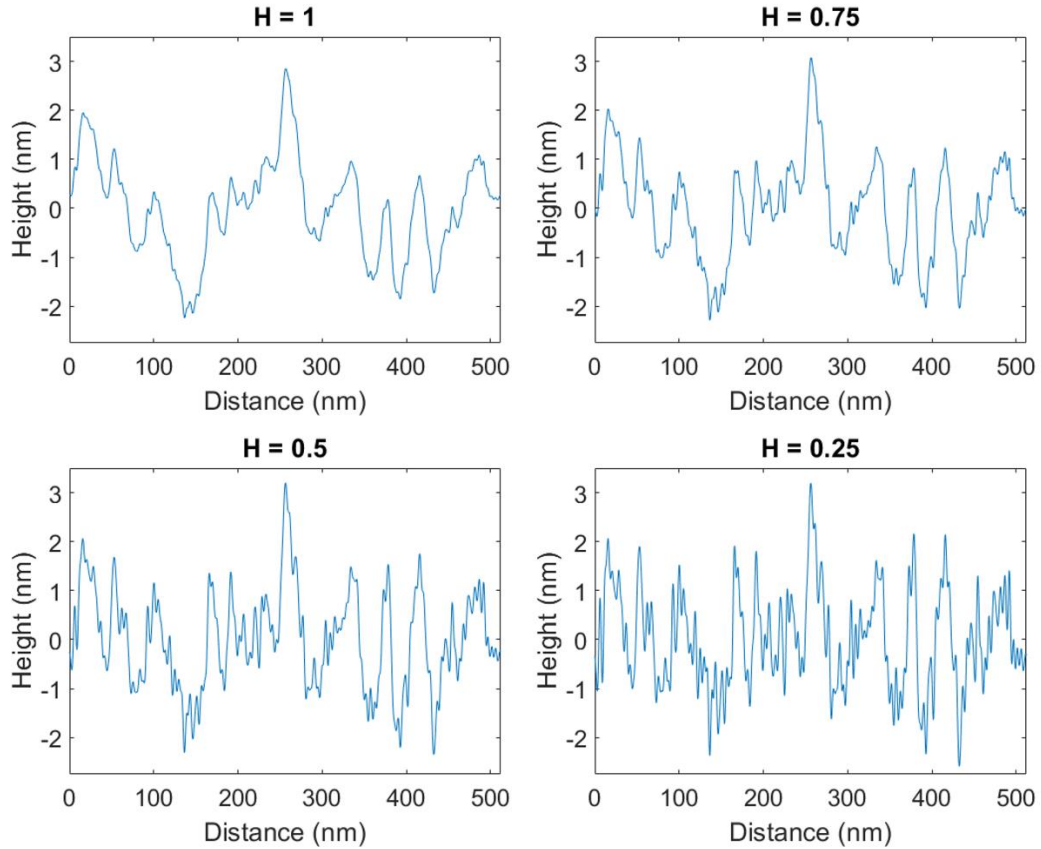


Figure 14 Synthetic, self-affine profiles with varying Hurst exponents

Each of these surfaces was analyzed in the context of the VBM, ACF, and PSD. Figure 15 shows the result of each of these methods applied to the four synthetic surfaces. Each method has a distinct slope in the self-affine region and is marked at the points where different regions of scaling occur.

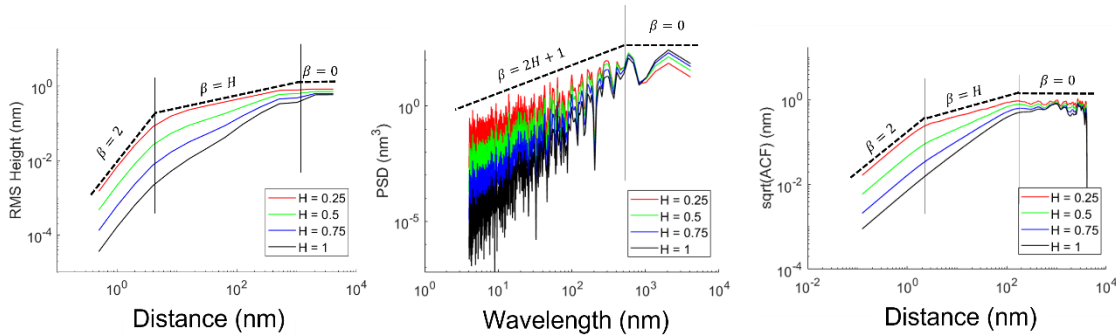


Figure 15 The VBM (left), PSD (middle), and ACF (right) applied to each of the four synthetic profile shown in figure 15

These results will be discussed in the following sections and will offer insight into how each of the methods performs when applied to these synthetic profiles as well as some special cases of roughness shapes.

3.6.2 Detecting the Start and End of Self-Affinity: The Long-Wavelength “Roll-Off” and the Short-Wavelength “Cut-Off” Region

All three methods accurately show the self-affine region between the small- and large-wavelength cut-off. However, the behavior at these two limits is very different between the three methods.

Regarding the long-wavelength “roll-off” region, the VBM shows a clear leveling off at larger wavelengths, reflecting the true input data. However, the ACF is less well behaved at wavelengths approaching the length of the profile. The shifted term in equation 3-3 cannot exceed the scan length., and when the shift amount approaches the scan length, fewer and fewer datapoints are used in the calculation. When, for example, the shift becomes one pixel less than the length of the scan, then we only have a single datapoint in the calculation. This leads to the unstable behavior of the ACF at wavelengths near the scan size. The ACF can also be computed on a periodic

topography to avoid this issue. A profile can be forced into periodicity by tiling it end-to-end with mirror symmetry; thus, the unstable behavior at large distances avoided. However, care needs to be taken that the profiles have little or no features on the length of the full scan, otherwise, new periodicity will be added, and roughness will be introduced at the largest scales.

The VBM does not rely on shifting the profile and simply includes more and more data right up to the full length of the profile. Although it has been recommended to only include bandwidths less than half the width of the profile measured for the sake of sufficient independent sampling [89]. The roll-off region in the VBM, then, approaches the RMS height of the profile and does not deviate as the ACF does. The PSD has a well-defined roll-off region, but the curve generally appears much noisier than the other two methods.

The VBM calculates roll-off at a wavelength of 500 - 2048 nm, the ACF at 150-300 nm, and the PSD at 400-1500 nm. The roll-off region should correspond to the long-wavelength cutoff, 256 nm in the case of these synthetic profiles. The ACF seems to give the closest estimate of the true long-wavelength cutoff of 256 nm.

Regarding the short-wavelength cut-off region, the VBM and ACF plots both show a kink between the λ^H region and the λ^2 region, which occurs at this cutoff. This λ^2 region corresponds to the “ballistic region” of the ACF, as described in Ref. [83]. The VBM offers better distinction between the λ^H region and the λ^2 region due to the shallower slope in the fractal region for any given value of Hurst exponent. For a Hurst exponent equal to one, the self-affine region in the ACF is indistinguishable from the ballistic region. For a more common Hurst exponent that is typical of real-world surfaces (e.g. $H = 0.8$), the slope of the VBM self-affine region will be shallower than that of the ACF self-affine region, thus offering better contrast between the two regions. There is thus a trade-off: the steeper slope of the ACF makes it easier to

resolve the transition from roll-off to self-affine, but harder to resolve the transition from self-affine to the ballistic regime. On the other hand, the shallower slope of the VBM makes it easier to resolve the short-wavelength transition and harder to resolve the long-wavelength transition.

The PSD lacks the ballistic region data, correctly calculating that there are no features with wavelength below the short-wavelength cutoff. The magnitude of the PSD abruptly drops off at the short-wavelength cutoff.

3.6.3 Evaluation of the Hurst Exponent

The hurst exponents are extracted from each method and each profile created. The extraction of the Hurst exponent can be carried out by a simple linear fitting to the self-affine portion of each method’s data. The self-affine region for all three methods has an approximately linear shape with a constant slope that levels off at larger wavelengths as it approaches the roll-off region. At the roll-off region, the profile is no longer self-affine. The roll-off region was found as the region where the data deviated from a linear trendline by a factor of 2 and was confirmed visually on each plot. The Hurst exponents shown in table 2 were extracted from the self-affine region of each method. A least-squares linear fit was carried out on the logarithm of the PSD/ACF/VBM and the logarithm of the distance/wavelength. A thorough discussion fractal self-affine measurements is given in ref [89].

Table 2 Hurst exponents used to generate the synthetic profile above and the Hurst exponent extracted for each profile by each method

Input H	H (PSD)	H (ACF)	H (VBM)
0.25	0.249	0.315	0.344
0.5	0.499	0.524	0.557
0.75	0.749	0.712	0.783
1	1.000	0.835	1.006

3.7 Characterizing Other Common Topographic Factors: Crystallographic Facets, Surface Steps, and Reentrant Surfaces

The above discussion (and many other authors [81]–[86], [88]) have described the application of these methods to self-affine surfaces; however, as discussed in the introduction, many surfaces do not have self-affine behavior across all size scales. Real-world crystalline surfaces often display faceted surface structure that creates well-defined morphology over certain size scales. Because certain crystallographic planes are lower energy than others, the grains tend to be faceted, and there will commonly be a characteristic grain size that is determined by synthesis or processing conditions. Additionally, grains may be randomly oriented or may have preferred orientations, or “texture”. The topography of this grain structure can be described mathematically using Euclidean geometry (well-defined polyhedra) that persists over a certain range of length scales. A real-world example of this is given by the polycrystalline diamond surface that were explored in Ref. [63]. In this work, we show that a surface can have self-affine characteristics at scales larger than the grain size, then have Euclidean geometry in the size scale equal to the mean grain diameter, then go back to self-affinity at small scales due to roughness that is superimposed on individual facets.

To simulate a Euclidean surface, a profile was generated containing linear segments that meet at sharp points. Between each sharp point the profile is smooth and linear. In theory, the fractal dimension of Euclidean geometries is 1. However, the apparent exponent extracted from the PSD and VBM can differ from the value corresponding to $H = 1$ because such surfaces are not truly fractals. The Hurst exponent extracted from the VBM, ACF, and PSD is shown in figure 16, and discussed in more detail in the following sub-sections.

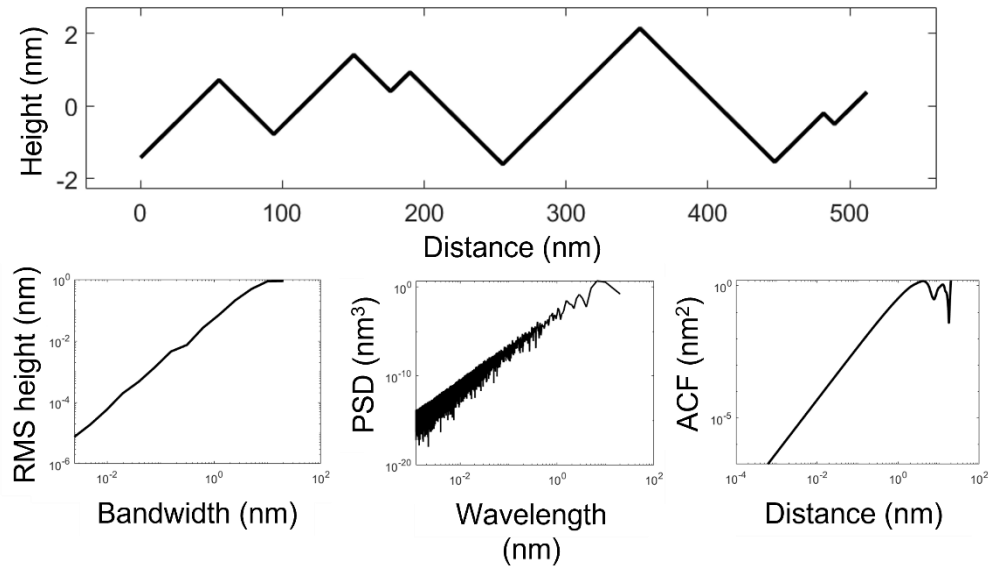


Figure 16 The euclidian profile analyzed and the corresponding VBM (left), PSD (middle), and ACF (right)

The hurst exponents extracted from each method is given in table 3 below. The ideal Hurst exponent is equal to 1. The three methods each provide a different interpretation of the profile.

Table 3 Hurst exponents extracted from the euclidian profile using each of the VBM, ACF, and PSD. *the extracted value for the VBM depends on detrending (discussed in section 3.7.1). The theoretical or ideal

Hurst exponent is also given.

Method	Hurst exponent
Ideal	1
VBM	1.435*
ACF	0.995
PSD	1.464

3.7.1 The VBM

Equations 3-19 through 3-21 below give a simple derivation of the Hurst exponent for Euclidian profiles. If the slope of the VBM on a log-log plot is the Hurst exponent H, then

$$H = \frac{\log(VBM(\Delta x_{max})) - \log(VBM(\Delta x_{min}))}{\log(\Delta x_{max}) - \log(\Delta x_{min})} \quad (3-19)$$

Where Δx_{\max} and Δx_{\min} are the maximum and minimum bandwidths analyzed. The RMS height of a linear region is equal to the RMS slope multiplied by the length of the segment, so

$$VBM(\Delta x) = h_{rms}(\Delta x) = \Delta x h'_{rms} \quad (3-20)$$

Since Δx cannot be zero in the logarithm, define Δx_{\min} as δ and let $\Delta x_{\max} = \Delta x$

$$H = \frac{\log(\Delta x h'_{rms}) - \log(\delta h'_{rms})}{\log(\Delta x) - \log(\delta)} = \frac{\log\left(\frac{\Delta x h'_{rms}}{\delta h'_{rms}}\right)}{\log\left(\frac{\Delta x}{\delta}\right)} = 1 \quad (3-21)$$

The Hurst exponent for any linear section of a surface is equal to one. Once a ‘kink’ is encountered, the standard deviation of height, the RMS height, must decrease, the VBM rapidly flattens out into a roll-off like region. Further kinks in the profile serve to stabilize the RMS height and lead to an ever-flattening roll-off region over larger and larger bandwidths. Only when analyzing bandwidths below the ‘kink spacing’ will the VBM return a slope of 1. Above the kink spacing will be a roll-off region in the VBM toward a zero slope at large scales.

It is common practice to detrend data before calculating the standard deviation of heights. In this case, the standard deviation of heights is zero for linear segments and only becomes non-zero when a ‘kink’ is included in the window. If detrending is carried out after windowing, the Hurst exponent becomes 1.5. If the data is not detrended, the extracted Hurst exponent will be equal to 1.

3.7.2 The ACF

We can look at the power-law scaling of the ACF with distance and calculate the ideal Hurst exponent for a Euclidian profile, much like in the previous section on the VBM. For a straight line starting at the origin, $h(x) = mx$

$$ACF(\Delta x) = \frac{1}{2} \langle \{h(x) - h(x + \Delta x)\}^2 \rangle \quad (3-22)$$

Becomes

$$ACF(\Delta x) = \frac{1}{2} (m\Delta x)^2 \quad (3-23)$$

Where m is the slope of a linear profile section. Using the same argument as in the VBM (equations 3-24 through 3-26), the slope between Δx and δ is equal to twice the Hurst exponent

$$2H = \frac{\log\left(\frac{1}{2}(m\Delta x)^2\right) - \log\left(\frac{1}{2}(m\delta)^2\right)}{\log(\Delta x) - \log(\delta)} = \frac{2\log\left(\frac{\Delta x}{\delta}\right)}{\log\left(\frac{\Delta x}{\delta}\right)} = 2 \quad (3-24)$$

Thus, the Hurst exponent for Euclidian profiles is equal to 1. We can also use another definition of the Hurst exponent, that describes how amplitudes scales with wavelengths in self-affine profiles according to equation 3-25 below.

$$\Delta x \rightarrow \lambda\Delta x, \Delta h \rightarrow \lambda^H\Delta h \quad (3-25)$$

Below the facet size,

$$\Delta x \rightarrow \lambda\Delta x, \Delta h \rightarrow \lambda\Delta h \quad (3-26)$$

According to the transformation shown in eq 33, the Hurst exponent must be equal to 1.

3.7.3 The PSD

The Euclidian profile can be described by a triangular function. The Fourier transform for a triangle function scales with q^{-2} . It follows that the PSD, the square of the Fourier transform, then scales with q^{-4} , which corresponds to a Hurst exponent of 1.5 (given that $q^{-1-2(1.5)} = q^{-4}$)

The usefulness of these analyses applied to Euclidean geometries comes about when dealing with polycrystalline surfaces. Such surfaces will very often have faceted shapes [63]. If we see that The PSD gives a Hurst exponent equal to 1.5 and the other methods return a Hurst exponent of 1, then determine that such structures are present and even get an idea of their size based on where the slope of each method flattens out.

3.8 Step Functions

A stepped surface is also a unique case and one that is relevant in application. A stepped surface profile can result from intentional patterning or can be the result of overhanging features on reentrant surfaces. A reentrant surface contains areas where there is some material overhanging another area of surface. Typical topography measurement instruments lack the ability to resolve overhanging features completely. Using an AFM, for example, the overhanging feature would appear as an abrupt step, (limited by the radius of the tip) removing the portion of the profile inaccessible to the vertical probe. Thus, most measurements of overhanging features will show sharp steps.

3.8.1 The PSD:

The Fourier transform for a single step function scales with q^{-1} [93]. It follows that the PSD, the square of the Fourier transform, then scales with q^{-2} . Based on established relationships between the slope of the PSD and the Hurst exponent [89] in the self-affine region (slope = $-2H - 1$). This q^{-2} scaling corresponds to a Hurst exponent of 0.5.

3.8.2 The ACF:

We assume that the profile has n_s steps (discontinuities) but is differentiable between these points. A measurement samples the heights on n points spaced by Δx . Differentiability means that $\Delta h(x_i, x_i + \eta\Delta x) \sim \eta\Delta x$ for $\eta \rightarrow 0$. In contrast $\Delta h(x_i, x_i + \eta\Delta x)$ is nearly independent of η when the interval contains a step. For each step, there are η intervals containing one step (we assume the spacing between the steps is larger than $\eta\Delta x$). We split the ACF into the contribution from the continuous points and from the steps and take the limit of $\eta \rightarrow 0$:

$$\begin{aligned}
 ACF(\eta\Delta x) &= \frac{1}{n} \sum_{i=0}^{n-1} \Delta h(x_i, x_i + \Delta x)^2 & (3-27) \\
 &\simeq \frac{n_s}{n} \eta c_1^2 + \left(1 - \frac{n_s}{n} \eta\right) c_2^2 \eta^2 \sim \eta
 \end{aligned}$$

The first term is the contribution from the steps and c_1 corresponds to a typical step height. The second term is the contribution from the differentiable region to the ACF and c_2 corresponds to a typical slope. Hence the apparent Hurst exponent is also 0.5 in the ACF.

3.8.3 The VBM:

The VBM computes the average rms-height of sub scans of length l . n_s of the L/l subscans contain a step. Because the profile is differentiable between the steps, the $h_{rms} \sim l$ for small l . If slope detrending is applied $h_{rms} \simeq 0$ for small l .

$$VBM(l) \simeq \frac{l}{L} \left[\left(\frac{L}{l} - n_s \right) 0^2 + n_s c_2^2 \right] \propto l \quad (3-28)$$

Again c_2 is a typical step size. This also means that the exponent obtained from VBM is also 0.5. To test these calculations steps were introduced into the synthetic surface with $H = 1$ shown in section 3.6.1. The steps have height equal to 0.15 times the peak-to-valley height, six steps were introduced. At scales above the short wavelength cutoff, the non-stepped topography dominates the magnitude of each method. After the short wavelength cutoff, the slopes of the stepped and un-stepped profiles diverge. Here, the ACF, VBM, and PSD of the stepped topography have a slope corresponding to a Hurst exponent of 0.5. The result of each method applied to the stepped functions.

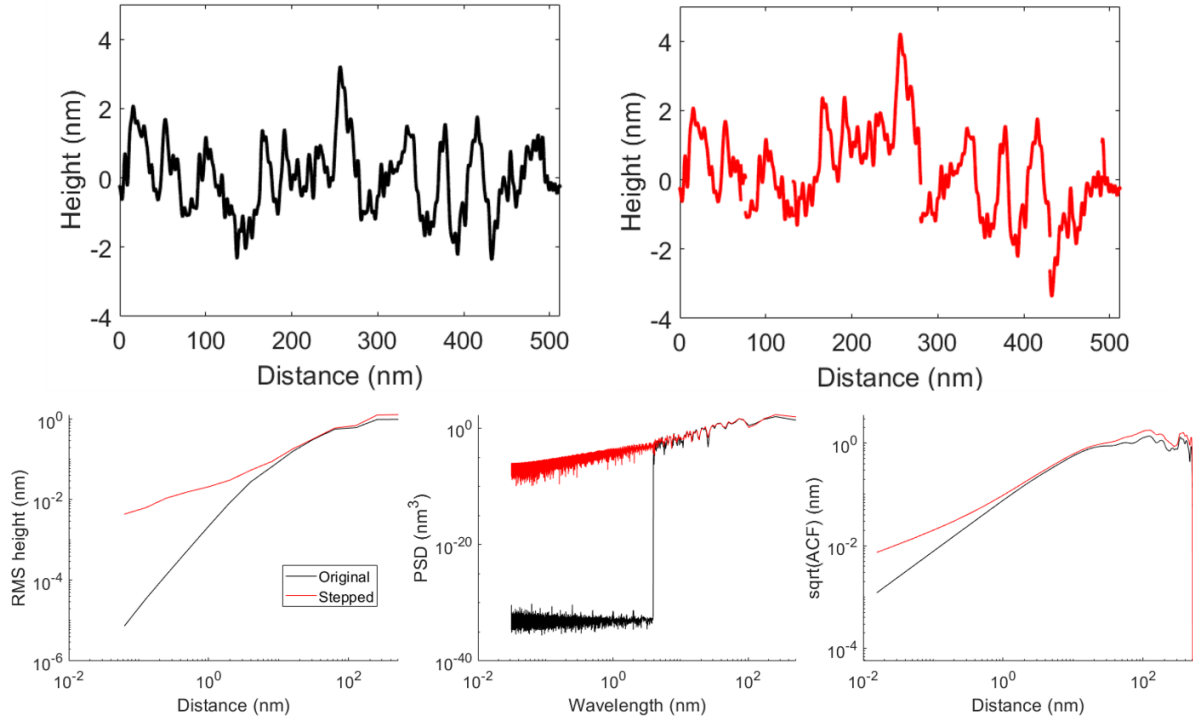


Figure 17 The height profile for the synthetic surface with $H = 0.5$, original (black) and with steps introduced (red) and the VBM, ACF, and PSD for a stepped profile (RED) and the unstepped profile (black)

All three methods are affected by the introduction of this noise. The VBM deviates from the non-stepped curve just above the short-wavelength cutoff, tending toward a slope corresponding to $H = 0.5$. The ACF behaves in a similar way, however the deviation appears at a slightly smaller scale, just below the short-wavelength cutoff. The PSD shows the most obvious change between the stepped profile and the non-stepped profile. This stark difference is only visible because we know the exact short-wavelength cutoff of the synthetic profile. In a real measurement, the noise-affected region would be more difficult to detect. In all three cases, the noise is distinguishable by a slope change, however subtle, between the self-affine region and the step-affected region. For a surface with Hurst exponent equal to 0.5, the self-affine region will be perfectly matched by the effects of steps. The farther the exponent is from 0.5, the stronger the distinction will be between the self-affine region and the step contributions.

3.9 Accurately Describing Reentrant Surfaces

Many real-world surfaces do contain reentrant regions, for example, nanoparticle coated surfaces have a down-facing region toward the bottom of the particle, additive manufacturing surfaces may have unmelted powder grains on the surface that also contain down-facing portions, also certain ceramics and other porous materials will contain surface pores that may have reentrant, cave-like features. These reentrant surfaces cannot be resolved with any top-down method (e.g., stylus profilometry, atomic force microscopy, optical interferometry), but can be accurately resolved using cross-section methods, such as cross-section scanning electron microscopy [94] or cross-section transmission electron microscopy [49].

Reentrant measurements cannot be analyzed with the PSD or ACF, since these techniques require a well-defined function, with one height value for each lateral position. Therefore, the VBM is the only approach that can be used for reentrant surfaces. The VBM requires only that we can average all height values within a window.

3.10 Characterizing Common Topographic Artifacts: Measurement Noise and Tip-Radius

Artifacts

3.10.1 Synthetic Surfaces with Intentionally Designed Measurement Noise and Radius

Artifacts

Experimental topography measurements will always have some contribution from environmental or instrumental noise. This noise most commonly appears as either a peak at a well-

defined frequency (for instance due to mechanical vibration or alternating-current electronic signals) or as a broadband background (for instance due to random thermal or electrical interference). The smaller the scale of the measurement, the more significant the noise contribution.

Here, the effect of broad-spectrum noise is investigated by superimposing a random signal on the synthetic scans from the previous section in the form of white noise with a signal-to-noise ratio of 50:1. Noise is introduced randomly at each pixel, essentially adding noise at the smallest scales measured (or synthesized). Analysis was performed on an ideal synthetic surface with $H = 0.75$ and the effects of the noise are shown in figure 18. The slope of the VBM, ACF, and VBM tends toward zero for white noise.

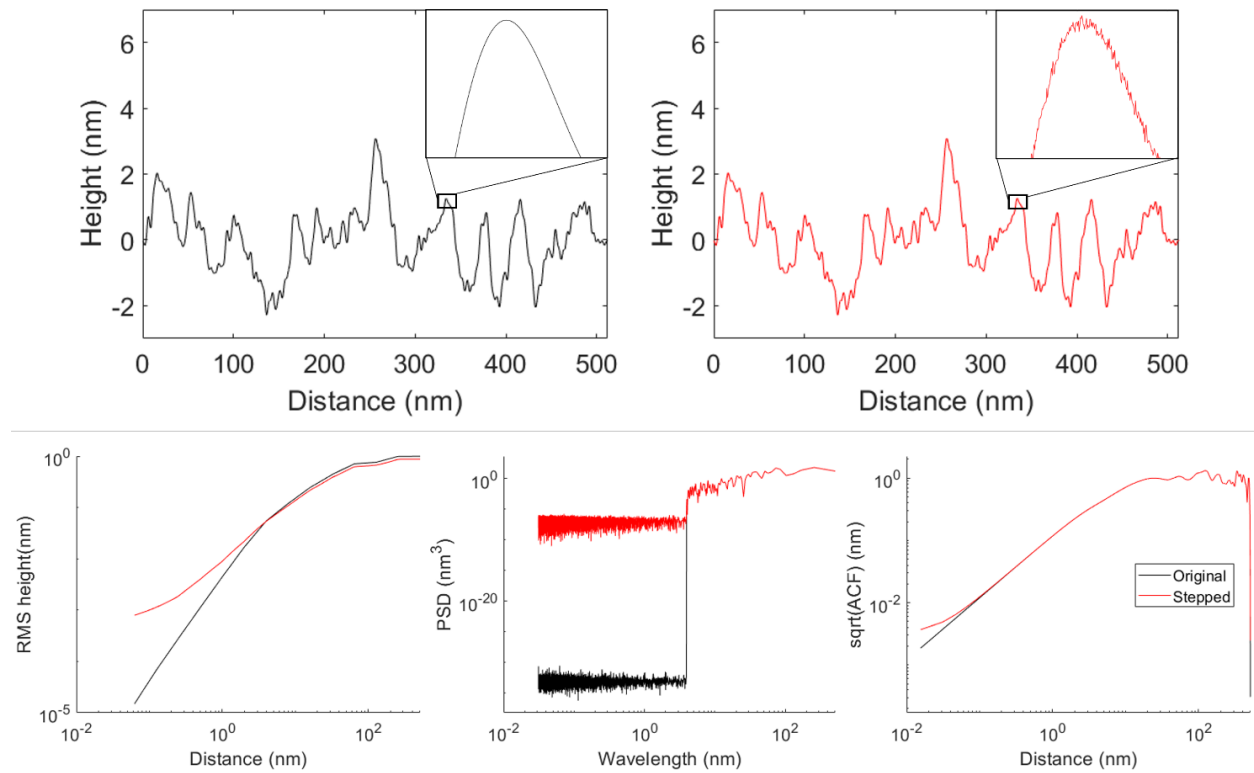


Figure 18 The height profile for the synthetic surface with $H = 0.75$ (black) and the same profile with white noise added (red) and the VBM, ACF, and PSD for surfaces with white noise introduced

The data is unaffected at the largest scales and only begins to deviate from the noiseless profile data near the smallest scales. For the PSD, the ideal profile magnitude goes to near zero and has a flat slope. The noisy signal PSD deviates at the small wavelength cutoff. It still has a zero slope, but has a larger magnitude, reflecting the newly introduced amplitude of the noise signal. The noisy profile VBM has similar behavior and starts deviating from the ideal profile VBM around 1 nm, below the small-wavelength cutoff of 4 nm. The noisy profile ACF begins to deviate around 0.1 nm, well below the small-wavelength cutoff of 4 nm. It seems that the ACF is less sensitive to noise than the VBM. In both the VBM and ACF, the ballistic region is drowned out by the noise contribution.

When noise is introduced at the scale of single pixels of a measurement, it manifests itself as a flattening of the curve (for all three methods) toward the smallest scales. Although where the noise begins to influence the curve seems to depend on the method. The flattening slope at the smallest scales could be mistakenly interpreted as increased roughness amplitude. While this increased amplitude might have truly been measured, the distinction between topography and noise contributions needs to be considered. Best practice is to characterize *both* the topography and the noise of the instrument. This helps to decouple the two contributions.

3.10.2 Real Experimental Surfaces with Measurement Noise and Radius Artifacts

Experimental data is analyzed using the VBM, ACF, and PSD. Each of these methods was used to analyze a large set of surface measurements from a real surface in [64]. The surface of a polycrystalline diamond coating, ultrananocrystalline diamond (Advanced Diamond Technologies, Romeoville, IL), was characterized using stylus profilometry and AFM. This

characterization is described in ref [63]. 1D profiles were extracted from each measurement. Together, these measurements had scan sizes from 10 cm down to 25 nm. A representative AFM image of the surface is shown in figure 19.

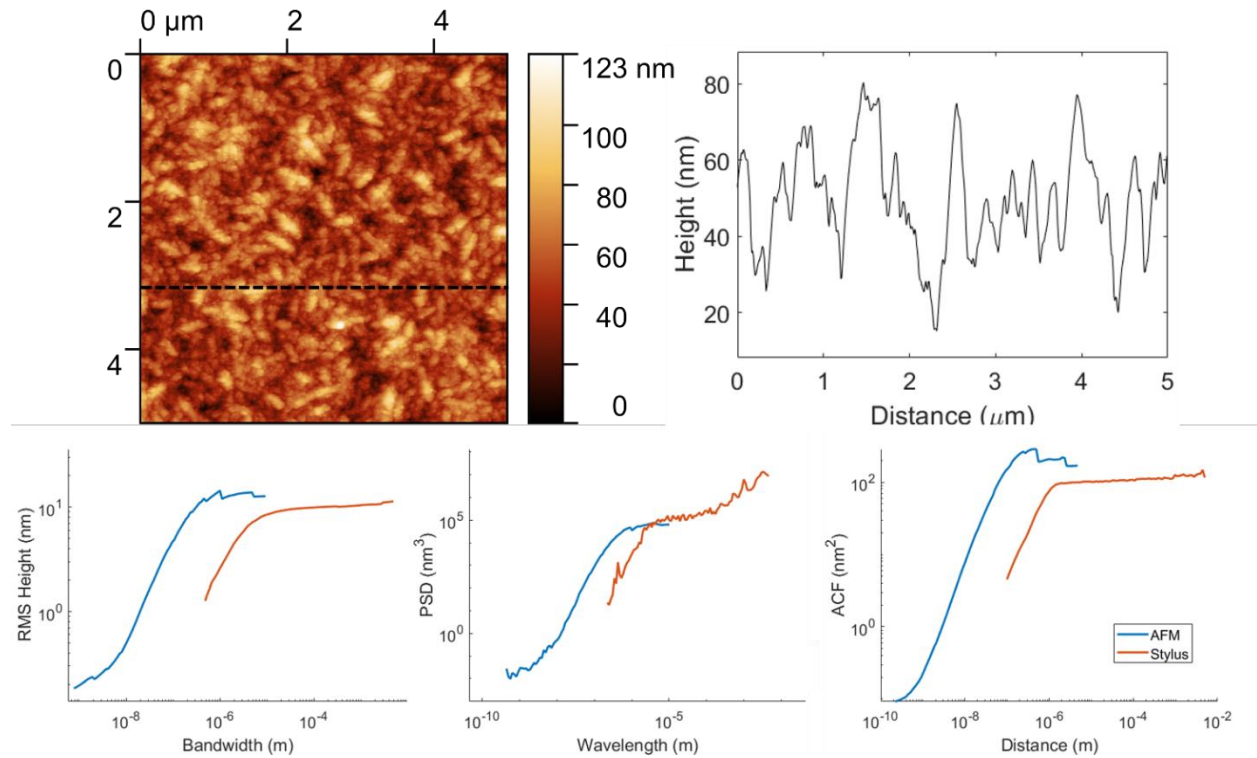


Figure 19 A representative AFM image of ultrananocrystalline diamond (top left) with a linescan extracted along the dashed black line, the extracted height profile (top right), and the VBM (lower left), the PSD (lower middle), and ACF (lower right).

Like the generated surfaces, the real surface has a self-affine region and a roll-off region. Shown in figure 19 are the three methods applied to a UNCD surface. The self-affine region is clearly visible in all three methods plot above. The plot also clearly shows the roll-off region where the curves flatten out at large distances. Note that these plots represent the average of dozens of measurements overlapping across all scales, thus they appear smoother than many of the analyses

shown above. The Hurst exponent can be extracted from all three methods as a function of the power-law scaling of the self-affine region. These extracted values are given in table 4. A simple linear regression was performed on the logarithm of distance and VBM/ACF/PSD magnitude. The self-affine region was isolated from the roll-off region before fitting.

Table 4 Hurst exponents extracted from real surfaces

Method	Slope of self-affine region	Hurst Exponent
ACF	1.47 ± 0.02	0.74 ± 0.01
PSD	2.67 ± 0.05	$.84 \pm 0.03$
VBM	0.82 ± 0.02	0.82 ± 0.02

The effects of tip radius are apparent in all three plots. The stylus, which has a far larger tip radius than AFM, becomes insensitive to smaller scales of roughness very quickly. This manifests itself as a drop-off in the magnitude of the VBM, ACF, and PSD. As the roughness features fall below the tip radius, the stylus sees the surfaces as more and more perfectly smooth. Note, however, that this downtrend in the curves indicates that the stylus is not nearing its noise floor, it is merely limited by the tip radius.

The AFM data, on the other hand, shows clear signs of noise in the smallest scales of roughness measured. At the smallest scales, on the left-most portions of all three plots, the AFM data begins to level off. This leveling effect is indicative of noise in the measurements, whether vibrations or electrical noise. In the case of real measurements, taking data on the vibration of the system or electromagnetic interference will help to determine the precise origins of the noise at small length scales (high frequencies).

3.11 Conclusions

The three methods of multi-scale analysis discussed here all have distinct advantages. In terms of ease of interpretation, the VBM gives the most intuitive interpretation of a surface. When we look at the VBM plot, we have simple axes of RMS height and distance. This method reports the scalar roughness parameter as a function of scan size.

The ACF gives a description of how different points on a surface or profile relate to one another. Instead of reading a simple scalar roughness parameter from the ACF plot, we must interpret the strength of the correlation between shifted datasets. The function will have a minimum value when the profile is not shifted relative to itself. As the shift becomes larger, the value will increase. It will continue to increase as the height difference between shifted points grows. Once the curve levels off, further shifting no longer introduces larger magnitudes of height variation. This begins the roll-off region where the ACF becomes equal to the square of the RMS height.

The PSD is a bit more complex of an interpretation of the surface. We can extract scalar roughness parameters from this method, but looking at the plot, it is difficult to make any quantitative conclusions without further analysis. We can easily see a roll-off region just as in the other methods. All scales of roughness with wavelengths in this region have magnitudes that no longer scale with wavelength, unlike in the self-affine region. A critical advantage of the PSD is its ability to analyze 2D data. While the ACF and VBM must be calculated over line scans, the PSD can analyze an entire surface. The 2D PSD can therefore give information on orientation-dependent or anisotropic topography, which other methods could not.

Different types of topographies can produce different behaviors in each of the methods used. For a complete understanding of the nature of topography, all three methods can be combined to examine aspects of agreement and disagreement. This is especially true in cases where there are

special roughness features that do not conform to fractal geometry (such as Euclidian geometries or steps). When multi-scale analysis methods are performed on these surfaces, the various methods differ in terms of the apparent fractal behavior of the profile. These differences can shed light in the nature of roughness present on a surface.

Different types of topographies can produce different behaviors in each of the methods used. In order to be completely confident in the analysis of a surface, it is best to simply compute all three methods and ensure that they are in general agreement. This is especially true in cases where there are special roughness features that do not conform to fractal geometry (such as Euclidian geometries or steps). When multi-scale analysis methods are performed on these surfaces, they differ in terms of the apparent fractal behavior of the profile. These differences can shed light in the types of roughness present on a surface.

4.0 Hard-Material Adhesion: Which Scales of Roughness Matter?

The majority of chapter 4 is reproduced from *Thimons, L.A., Gujrati, A., Sanner, A. et al. Hard-material Adhesion: Which Scales of Roughness Matter?. Exp Mech (2021). <https://doi.org/10.1007/s11340-021-00733-6>*

4.1 Chapter Overview

Background: Surface topography strongly modifies adhesion of hard-materials contacts, yet roughness of real surfaces typically exists over many length scales, and it is not clear which of these scales has the strongest effect.

Objective: This investigation aims to determine which scales of topography have the strongest effect on macroscopic adhesion.

Methods: Adhesion measurements were performed on technology-relevant diamond coatings of varying roughness using spherical ruby probes that are large enough (0.5-mm-diameter) to sample all length scales of topography. For each material, more than 2000 measurements of pull-off force were performed in order to investigate the magnitude and statistical distribution of adhesion. Using sphere-contact models, the roughness-dependent *effective* values of work of adhesion were measured, ranging from 0.08 to 7.15 mJ/m² across the four surfaces. The data was more accurately fit using numerical analysis, where an interaction potential was integrated over the AFM-measured topography of all contacting surfaces.

Results: These calculations revealed that consideration of nanometer-scale plasticity in the materials was crucial for a good quantitative fit of the measurements, and the presence of such plasticity was confirmed with AFM measurements of the tip after testing. This analysis enabled the extraction of geometry-independent material parameters; the *intrinsic* work of adhesion between ruby and diamond was determined to be 46.3 mJ/m^2 . The range of adhesion was 5.6 nm, which is longer than is typically assumed for atomic interactions but is in agreement with other recent investigations. Finally, the numerical analysis was repeated for the same surfaces but this time with different length-scales of roughness included or filtered out.

Conclusions: The results demonstrate a critical band of length-scales—between 43 nm and $1.8 \mu\text{m}$ in lateral size—that has the strongest effect on the total adhesive force for these hard, rough contacts.

4.2 Introduction

All real surfaces exhibit roughness, which has profound effects on surface properties. This includes the mechanics of interfaces - adhesion[26][95], contact stiffness [96]–[98], wetting[99], and friction [76]. Various analytical models have been developed to describe the dependence of functional properties on the geometry of the rough surface. The classic Greenwood & Williamson [100] multiasperity model for contact between rough surfaces was extended by Fuller and Tabor [26] and Maugis [27] to include adhesion. Further progress was made in connecting contact properties and roughness by Bush, Gibson, and Thomas (BGT) [28] and Rumpf [101], [102]. These models approximate real-world roughness using simpler mathematical functions and typically associate properties with a single geometric parameter, such as the root-mean square

(RMS) height. More recent models have attempted to explicitly account for the hierarchical, multi-scale nature of roughness. Mandelbrot began characterizing surfaces as fractal-like and self-affine using spectral analysis [30]. Later, Persson [75] created a theory for rubber friction which draws quantitative connections between fractal roughness and contact properties, including adhesion [36]. These multi-scale models are expansions that start from the limit of conforming contacts. They balance the adhesive energy gained when making contact with the stored elastic deformation energy, and are expected to work well for soft, conformal contacts.

A simpler approach is sufficient for hard contacts, in which the elastic energy required for creating a conforming contact is much larger than the interfacial adhesive energy gain: An interaction potential is integrated over the undeformed contacting geometry. This approach can be applied to simple analytical geometries, such as spheres [103][104], and can also be applied to more complex geometries, including rough surfaces, sharp tips, etc.[18], [55], [105]. Pioneering work by Delrio et al. [18] showed that long-range Casimir forces contribute strongly to surface adhesion of ultra-flat (RMS height of 2-10 nm) micromachined surfaces at distances up to tens of nanometers.

Three critical questions remain for describing the roughness-dependent adhesion of surfaces with multi-scale topography. First, can the classic analytical models such as those proposed by Fuller and Tabor, Rumpf, and Maugis, be applied to describe their behavior? Second, is the importance of long-range adhesive interactions limited to ultra-flat surfaces (as found in [18]) or is it generalizable to real-world coatings that are rough over many length scales? Third, and most generally, which size-scales contribute most strongly to adhesion?

The purpose of the present work is to investigate these questions using adhesion tests of some of the hardest materials: a ruby sphere on polycrystalline diamond substrates. Diamond

coatings are technologically relevant in a number of applications [106], including medical devices [107], [108], tool coating [109], face seals [110], and microelectromechanical systems (MEMS)[111]. The roughness of these films can be controlled by varying the growth condition or by polishing. Thus, we can test substrates with varying roughness but nominally identical surface chemistry. This allows us to isolate the effects of topography on adhesion. The surface topography [64] of these materials and their adhesion to soft PDMS [79] has been extensively characterized in prior publications. The present investigation examines their adhesion to a hard material: ruby.

Many adhesion studies have used atomic force microscopy (AFM) or colloidal AFM to characterize surface topography and then perform tip-based adhesion tests on the measured surface [5], [8], [112], [113]. Such investigations provide valuable information on the atomic-scale parameters governing nanoscale adhesion. However, the small size of the contact limits their applicability in understanding the contribution of multi-scale roughness to macroscale adhesion. The present investigation overcomes this limitation by using AFM to characterize the topography, but uses a 0.5-mm-diameter sphere to measure adhesion.

4.3 Diamond Substrates

Diamond is a highly relevant material, having uses primarily in low-friction and wear-resistant coatings. Any findings from this work should be easily translated into real applications, although this work seeks conclusions that can be generalized to more materials. Another benefit is ability to tune roughness while keeping surface chemistry constant. The diamond is grown on a silicon wafer using chemical vapor deposition. Growth techniques for CVD diamond are well-studied and can be controlled. By varying the growth parameters, the topography of the films can

be varied. Allows creation of surfaces with same chemistry and different levels and types of roughness. The availability and reproducibility of this coating material allows for very good potential reproducibility of the results gathered. An example of a CVD diamond film growth process is shown below in figure 20.

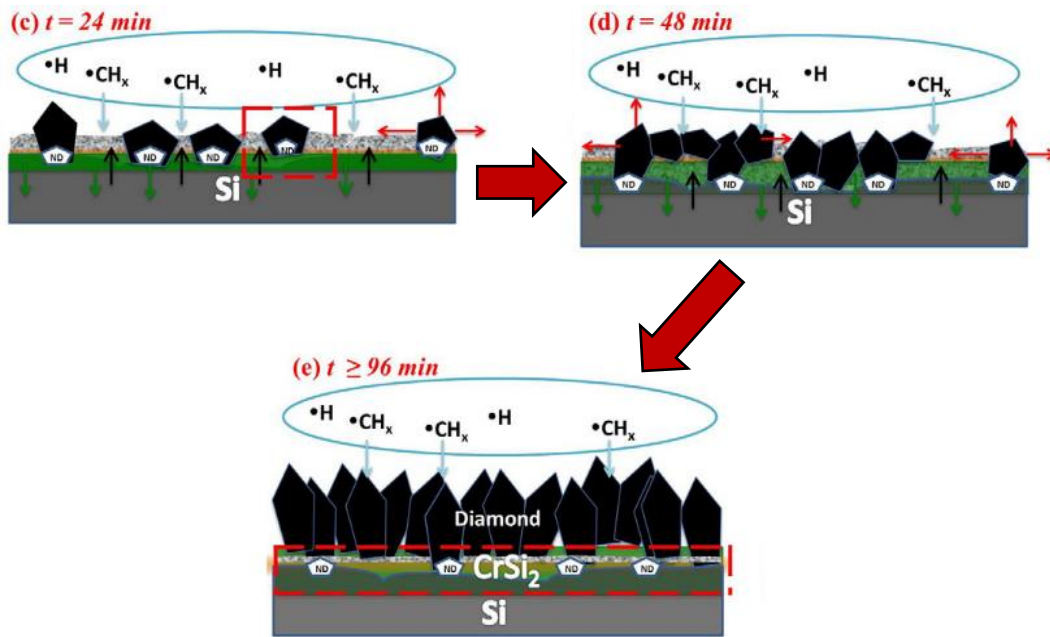


Figure 20 Schematic diagram of the growth of diamond films using CVD. Reproduced from [97]

The roughness of these films can be tuned without changing the bulk chemistry. Based on the nucleation density during the CVD process, this polycrystalline coating can be given a range of grain sizes. In the current study, four type of polycrystalline diamond (PCD) substrates are investigated. Microcrystalline, Nanocrystalline and Ultra-nanocrystalline diamond (UNCD). The UNCD substrate has two varieties, as grown surface and a mechanically polished surface, termed unpolished UNCD (uUNCD) and polished UNCD (pUNCD). By tuning the grain sizes, different topographies can be created. The topographies will have different types and magnitudes of

roughness. For the sake of the current work, the surface chemistry of all surfaces is assumed to be identical. There are some compositional differences between the different films, however.

The diamond films consist of sp^3 hybridized carbon in the diamond-cubic crystal structure. The grain boundaries contain sp^2 hybridized carbon. This carbon is more similar to graphite, forming sheets and having a free electron. An interesting feature arises from this. The surface chemistry, although assumed to be identical, may vary due to grain boundary density. The UNCD surfaces will have far more grain boundaries than the MCD and NCD. This means that there is a higher concentration of higher energy sp^2 carbon in the UNCD surfaces. This is not considered to be an issue in the current work. The grain boundaries in these films are at the lowest points on the surface, with the grains appearing to rise up from the grain edges. The contacts made are generally supported by the peaks of roughness and should not interact with grain boundaries. The area of interest is the surface of the diamond film, made up of crystallites of identical chemistry. The surfaces of the PCD substrates are assumed to be passivated by some species. In general, this species will be Oxygen or Hydrogen. Hydrogen is the typical dominant termination atom after the CVD process.

4.4 Methods

4.4.1 Experimental Adhesion and Topography Measurements

Adhesion tests were carried out between ruby microspheres and polycrystalline diamond coatings using a MEMS-based force sensing probe (FT-MA02, FemtoTools, Buchs, Switzerland). The 0.5-mm-diameter spheres (B0.50R, SwissJewel, Philadelphia, PA) were pre-polished to an

ultra-smooth (RMS height < 1 nm) finish using a slurry of ruby particles (0.05 μm). The spheres were glued to the tips of the force-probes to create a sphere-on-flat geometry for the test. The substrates comprised four different polycrystalline diamond coatings, which were grown by hot-filament chemical vapor deposition (HF-CVD) and are boron-doped for electrical conductivity. The substrates have varying grain size, and are denoted microcrystalline diamond (MCD), nanocrystalline diamond (NCD), ultrananocrystalline diamond (UNCD), and a polished form of UNCD. The deposition and surface topography of the diamond coatings are characterized in Ref. [63].

For this work, the topography of the spheres and substrates were measured using atomic force microscopy (AFM)(Dimension V, Bruker, Billerica, MA). Measurements were made using diamond-like carbon (DLC)-coated probes (Tap DLC300, Mikromasch, Watsonville, CA) in tapping mode. Scans with lateral size of 2.5 μm (512 x 512 pixels) were performed on each of the four substrates and on the ruby spheres.

Representative images for the surface topography of the substrates, and of the polished spheres are shown in Fig. 21. Using the AFM measurements of 2.5-micron lateral size, the root-mean-square height, slope, and curvature of the surfaces are given in Table 5. The surface topography of the polycrystalline diamond films has been extensively measured in Ref. [64]. In the numerical analysis included here, however integration over specific topography measurements on both the sphere and the flat were performed using AFM.

The MCD and NCD have the largest roughness magnitude of the four substrates, as is shown by the vertical scale bar of the AFM images in Fig. 21. These two surfaces also show clear faceting due to the grain structure. The unpolished UNCD is significantly smoother than the MCD and NCD, and the faceting is not apparent at these size scales. The features that are visible have

been shown to correspond to clusters of much smaller grains [64]. The polished UNCD is the smoothest of the four surfaces and shows no obvious grain structure. Similarly, the ruby tip images show a very smooth surface; while scratches are visible from the polishing process, the peak-to-valley roughness of this ruby sphere is smaller than all other surfaces. Common roughness parameters of the diamond surfaces are presented later in the Experimental Results section. These AFM images, along with 4 more from different sample areas of the various materials, form the basis of the numerical analysis that was performed.

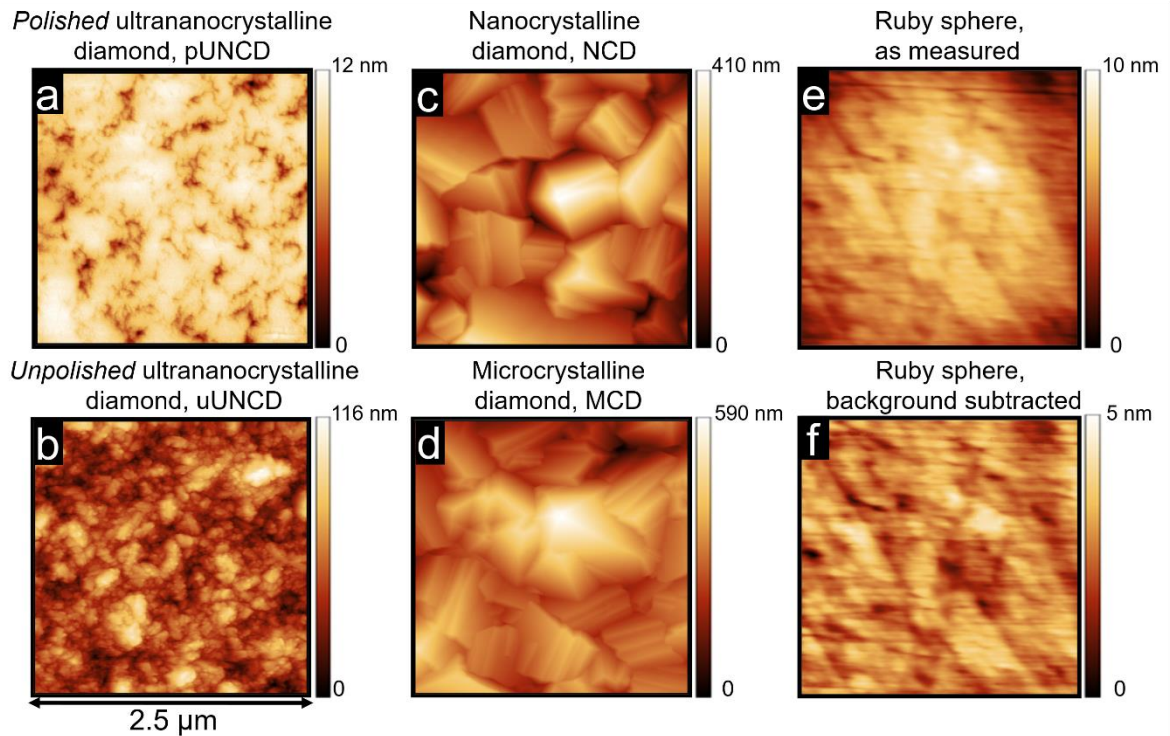


Figure 21 AFM measurements of the four polycrystalline diamond substrates (a-d) and one instance of a ruby sphere (e). The ruby sphere is also shown with its spherical geometry subtracted (f) to allow for direct comparison of roughness against the other surfaces

The adhesion testing was performed in a custom micromechanical tester in a controlled-environment vacuum chamber on a vibration-isolation table. Dry air was flowed into the chamber prior to testing until the relative humidity was less than 1% (below the minimum reading of the humidity sensor). Dry air was flowed in for the duration of the test at low flow rates to ensure consistently low humidity levels.

A three-axis slip-stick piezoelectric stage provides closed-loop motion control and real-time x-y-z position data. For each individual adhesion measurement, the sphere was brought into contact with the substrate, loaded to a 10- μ N preload (corresponding to a nominal Hertz stress of 135 MPa), and then withdrawn at a rate of 30 nm/s. The 10- μ N preload occurs before the test and represents the minimum force required for the probe to find the point of contact. After finding contact the tip is lowered slowly onto the substrate up to a preload of 5 μ N. This is the data used to quantify adhesion. The force required to pull the sphere off of the surface is recorded as $F_{\text{pull-off}}$, with a force resolution of +/- 30 nN. A single “test” comprised an array of individual adhesion measurements (typically 1-by-1 mm), for a total of 400 individual measurements per test. Tests were performed in immediate sequence on all four samples in randomized order, without opening the chamber or modifying test conditions. Six such sequences were performed with different spheres and different substrate samples, to ensure repeatability and reproducibility of results. A schematic of a typical test setup is shown in Fig. 8 in section 2.1.1.

4.4.2 Numerical Analysis of Results

The experimental data was fitted using a cohesive zone model, using an exponential interaction potential with energy U given by

$$U(r) = -W_{\text{adh,int}} \exp\left(\frac{-r}{\rho}\right) \quad (4-1)$$

with a hard-wall repulsion at $r = 0$. Here, $W_{\text{adh,int}}$ is the intrinsic work of adhesion, r is the distance between interacting bodies, and ρ is the “range of adhesion” [114], which describes its characteristic length scale. Note that U and W are energies per unit surface area. Since we do not know the exact nature of the microscopic interaction between the two surfaces, this approach of using an empirical exponential interaction potential is a pragmatic approach to simplify the mathematical calculations. Similar results would be obtained using more complicated functional forms, e.g. based on instantaneous or retarded dispersion interactions, electrostatic interaction, or others. Distinguishing between competing functional forms from our macroscopic experiments would be difficult. The functional form given in Eq. (36) allows separate fitting of the intrinsic work of adhesion (U at distance $r=0$) and the range of adhesion ρ , which yields the strength and length-scale of the interaction. This interaction potential has been widely used, including in the recent Contact Mechanics Challenge [40].

This interaction potential can be converted into a cohesive law (stress-distance relationship) for two interacting bodies,

$$p(r) = -\frac{dU}{dr} = -\frac{W_{\text{adh,int}}}{\rho} \exp\left(\frac{-r}{\rho}\right) \quad (4-2)$$

where p is the (compressive) pressure acting between the surfaces. For the present analysis, this potential was applied to each pixel pairing between the substrate and the tip, resulting in the following calculated force F_{calc} between the two contacting surfaces at separation d :

$$F_{\text{calc}}(d) = - \sum_{x,y} \frac{W_{\text{adh,int}}}{\rho} \exp\left(\frac{-(g_{x,y} + d)}{\rho}\right) A_{\text{pix}} \quad (4-3)$$

Here, A_{pix} is the area for a single surface pixel and the sum runs over all pixels in x and y . Note that $g_{x,y}$ in Eq. (38) is the *difference* of the topography maps of the ruby sphere and the diamond coating, while $g_{x,y}+d$ is hence the gap between the two interacting surfaces. The calculation can only be carried out for distances d where the gap $g_{x,y}+d$ is non-negative everywhere and the surfaces hence do not interpenetrate. The calculated adhesion values were thus found by summing the interaction potential pixel-by-pixel over every pixel pair of the two scans. The pull-off force is the minimum value of the force-separation curve $F_{\text{calc}}(d)$ that is found at the point of closest approach $d=-\min g_{x,y}$.

Due to random topography variation, there were sometimes significant contributions to adhesion from near the edges of the AFM scans. Therefore, for all substrate-tip combinations, the scans were stitched together so that there were no longer edge contributions to the adhesive interaction between the rough surface and a sphere 0.5 mm in diameter (<0.5% change from additional stitching). The stitching was done by mirroring the surface scans horizontally and vertically to ensure that all edges matched up. This was needed because real topography measurements are not periodic. Similar to the experiments, the tip was brought into contact with the substrate in many locations over a square array.

The above *rigid* analysis was supplemented by an elastic and a plastic analysis. For the elastic analysis, we computed surface deformation using a Fast-Fourier-transform-accelerated

boundary element technique [95], [115]. The hard-wall constraint was realized using an L-BFGS-B optimizer [116]. Note that we do not report the results of the elastic analysis explicitly here, but it was carried out to rule out the influence of elastic surface deformation. From this elastic analysis, we generally found that the surface pressure was exceeding common hardness values in most of the contact area such that a purely plastic analysis is appropriate.

For the plastic analysis, we use a simple bearing-area approach. This assumes that the harder surface permanently deforms the softer surface on all points that penetrate, and that the pressure in the contact area is equal to the hardness H . The penetration of the tip is then such that the number of contacting (and hence deformed) surface pixels is sufficient to support the preload, $N_{\text{contact}} = F / H A_{\text{pix}}$. A preload of 10 μN , chosen to match the experimental preload, was used to determine the amount of plastic deformation of the softer surface. No deformation then occurs during pull-off; the pull-off force is simply a result of the deformed geometry. Note that we did not employ a combination of elastic and plastic contact, but similar plasticity models were used in elasto-plastic contexts in Refs. [117]–[119].

4.5 Experimental Results

The topography can be used to compute roughness metrics such as root-mean-square (RMS) height, slope, and curvature, which are commonly used as inputs for rough-contact models. Table 5 shows the results of these calculations when performed only using the AFM measurements from this investigation (top) as compared to the same parameters that are computed when all of the many scales of roughness are included (bottom, using the full multi-scale spectral analysis from Ref. [63]). Table 5 shows the values that might serve as inputs to classical models, such as

those of Maugis [27] or Rumpf [101]. Table 5 also serves to underscore just how widely varying these parameters can be when measured at different length scales. For example, the root-mean-square slope, a parameter that has recently been identified as important for multi-scale roughness models, varies for polished UNCD from 0.04 to 0.39 depending on how it is measured.

Table 5 RMS roughness values calculated from AFM data only (top) and also from the full-spectrum roughness data, including topography data from stylus, AFM, and TEM measurements of the same surfaces.

AFM Data Only		<u>Polished UNCD</u>	<u>Unpolished UNCD</u>	<u>NCD</u>	<u>MCD</u>
	RMS height (nm)	3.2 ± 1.6	17.4 ± 2.1	97.1 ± 11.2	107.1 ± 12.0
	RMS slope	0.04 ± 0.01	0.39 ± 0.05	0.51 ± 0.07	0.49 ± 0.07
	RMS curvature (nm ⁻¹)	2.0*10 ⁻³ ± 1.3*10 ⁻³	4.8*10 ⁻² ± 3.8*10 ⁻³	3.9*10 ⁻² ± 1.1*10 ⁻²	2.8*10 ⁻² ± 6.6*10 ⁻³
Stylus, AFM & TEM Data [63]		<u>Polished UNCD</u>	<u>Unpolished UNCD</u>	<u>NCD</u>	<u>MCD</u>
	RMS height (nm)	4.6 ± 0.8	23.4 ± 1.3	121.7 ± 13.4	126.6 ± 8.2
	RMS slope	0.39 ± 0.04	1.46 ± 0.36	1.15 ± 0.13	1.07 ± 0.13
	RMS curvature (nm ⁻¹)	1.13 ± 0.23	3.37 ± 0.69	3.19 ± 1.15	2.83 ± 0.81

Figure 22 shows the distributions of values for adhesion force that have been measured on these four substrates. More than 2000 adhesion tests have been performed on every surface, with at least 6 different spheres. Each color on the histogram represents a new ruby sphere on a new sample of the diamond substrate. The mean adhesion of the polished UNCD was far higher than the unpolished version of the same material. Both UNCD surfaces showed higher adhesion than either the MCD or the NCD. The mean (median) pull-off forces of all four surfaces are 0.11 μN

(0.06 μN) , 0.16 μN (0.12 μN) , 0.4 μN (0.31 μN) , and 8.8 μN (1.75 μN) , for MCD, NCD, unpolished UNCD, and polished UNCD respectively. Due to the large skew in the data, the mean value is shifted away from the peak of the distribution toward higher adhesion values.

All four of the distributions can be fit using a log-normal distribution. This is more difficult to see in the linear plots, given the skew of a large number of events with small pull-off force. Plotted on a log-log scale (Fig. 22b), the log-normal distribution is shown to accurately fit the data over at least two decades of adhesive force. In all cases, the low end of the distribution is cut off at 30 nN, as this represents the sensitivity of the force probe. Similar shapes for adhesion distributions have been reported previously for measurements in various contexts, including: centrifugal adhesion studies of particle adhesion in powders [59][62]; biological samples and cell adhesion [120][121]; and many other studies using AFM adhesion measurements [43], [53], [122]. The origin of this distribution shape is not yet clear. While the fit is good for a log-normal distribution, there are other distributions—such as half of a gaussian distribution an inverse-gaussian distribution— that also give good qualitative fits. Further investigation is required to ascertain the origin of the shape of these distributions.

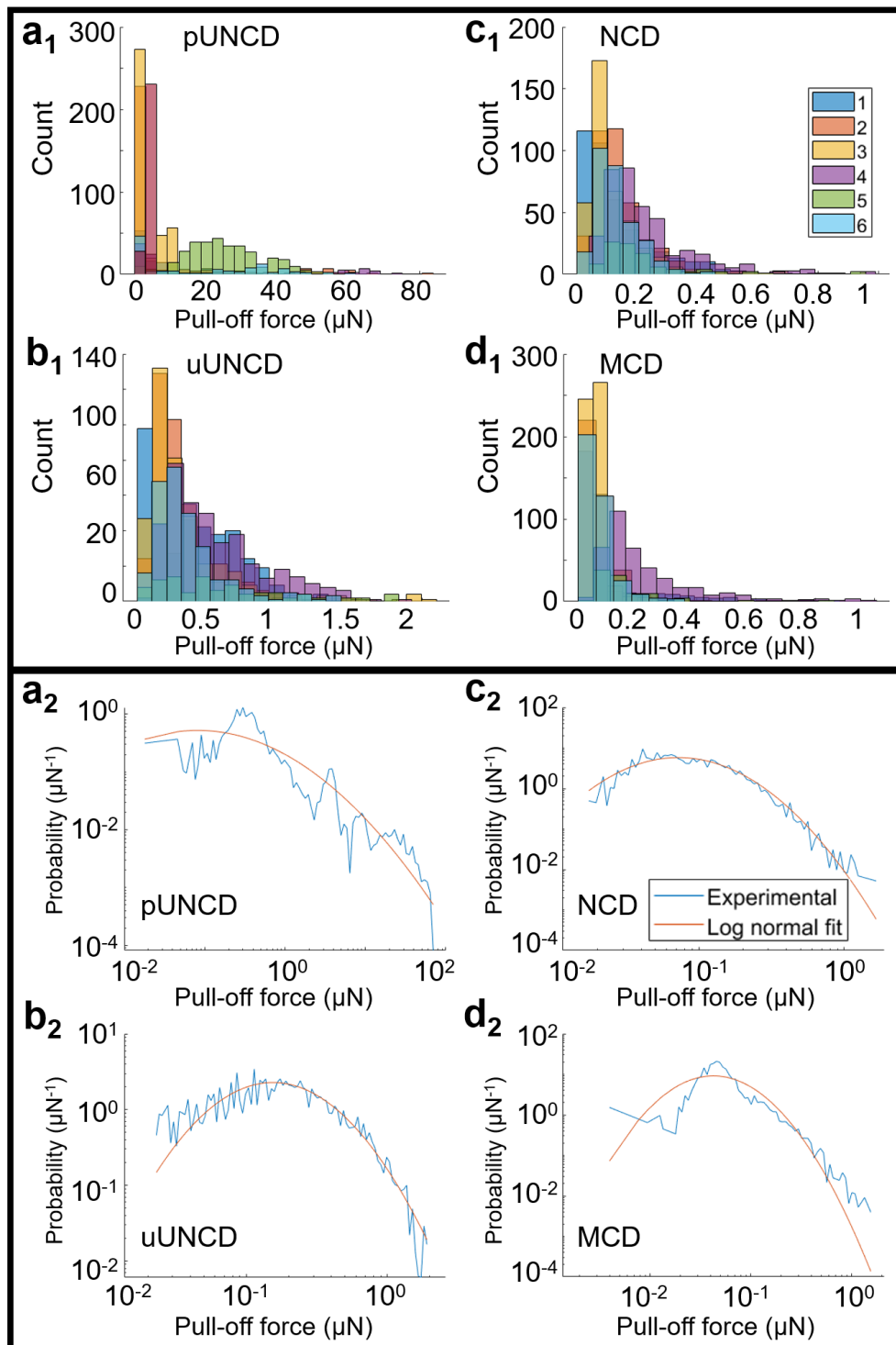


Figure 22 Experimental pull-off data is shown for the four substrates across different testing sessions (different colors) on a linear scale (a1-d1). The same data from panel a is combined into a single dataset and shown on a log-log plot (a2-d2), with log-normal distribution fitted to the data.

4.6 Discussion

4.6.1 Effective Work of Adhesion and the Application of Classical Rough-Adhesion Models

A standard method of analyzing adhesion in rough spheres is to use classical sphere-contact models (such as JKR or DMT [123]) to extract an *effective* work of adhesion $W_{\text{adh,eff}}$, and then to use standard roughness models (such as those described in the first paragraph of the introduction) to relate $W_{\text{adh,eff}}$ to standard roughness parameters. Following the procedure of Grierson, *et al.* [24], with material parameters of ruby (elastic modulus $E = 365$ GPa and Poisson ratio $\nu = 0.29$) and diamond ($E = 1010$ GPa, $\nu = 0.22$) and a nominal sphere diameter of 0.5 mm, the Tabor parameter is determined to be 0.81. This falls in the transition region between the DMT and JKR models. Using Maugis' analysis for the transition region between JKR and DMT, the analysis yields values of $W_{\text{adh,eff}} = 0.08, 0.13, 0.32,$ and 7.15 mJ/m² for MCD, NCD, unpolished UNCD, and polished UNCD, respectively. The surface chemistry is assumed to be similar for all of these HF-CVD diamond coatings, and therefore this difference is attributed primarily to surface topography.

It is clear from these measured values of effective work of adhesion, along with the values of RMS parameters shown in Table 5, that there are no simple relationships between RMS parameters and effective work of adhesion. Attempts to fit this data using simple analytical models [26], [28], [101] were unsuccessful, regardless of which roughness parameters were used (AFM-based or multi-scale). One potential explanation for why these models fail here is that the pull-off force for these hard materials is most dependent on the behavior of the uppermost contact points. These contacts represent the extreme-value statistics of the distribution of surface heights. They

do not follow the central limit theorem and are likely not described by the many models based on Gaussian statistics. Rather than relying on classical models to extract an effective work of adhesion, more deterministic modelling can be carried out to gather insight into the work of adhesion between our two surfaces.

4.6.2 Intrinsic Work of Adhesion and Range of Adhesion

Instead of a single-asperity model extracting the effective work of adhesion for each substrate, a numerical analysis can be performed using the combined roughness of the sphere and substrate (see Methods). Like the experiments, the calculations were repeated for an array of 20 x 20 contacts on each substrate. Each numerical calculation yields a computed pull-off force F_{calc} for a specific choice of input values for $W_{adh,int}$ and ρ and a specific contact location on the rough surface. Then a fitting routine can be applied to all data to extract the best-fit values of those material parameters.

For numerical tractability, the analysis was only performed over a square of size of 12.5 μm rather than the 1-mm size scale of the experiments. Initially, the calculations were performed assuming rigid and/or elastic deformation only. Elastic calculations were virtually indistinguishable from the rigid calculations and we concluded that elasticity does not play a significant role in these contacts. Additionally, the micronewton-scale adhesive forces measured experimentally could not be explained with adhesion models based on rigid or elastically deforming surfaces, thus indicating that permanent deformation may be occurring in these contacts.

We incorporated permanent deformation of the ruby tip with hardness of $H = 25$ GPa [124], [125] into our model using a penetration hardness model (see Methods). We first determine the deformation in the softer sphere at a preload of $10 \mu\text{N}$, identical to the average load used to find contact in the experiments. Pull-off calculations using the deformed topography of the sphere were able to accurately reproduce the micronewton scale of pull-off forces from the experimental data. The possibility of plastic flow in similar hard materials has been reported in nanopillars [126] and nanoparticles [127]. A more in-depth analysis of the role of permanent deformation in these contacts is included in the following section.

The numerical analysis can be fit to the mean values of the experimental data from all four substrates in order to extract best-fit values for intrinsic work of adhesion and the range of adhesion. We note that while $W_{\text{adh,int}}$ simply rescales the computed pull-off force, the dependence of F_{calc} on ρ is nonlinear and depends on the specific topography. The range of adhesion ρ is extracted by analyzing the *ratios* of pull-off forces between materials, since this cancels the (unknown) intrinsic work of adhesion $W_{\text{adh,int}}$ in our model equations. Figure 23b shows the ratio of the pull-off force of polished UNCD, NCD and MCD with respect to unpolished UNCD. The solid horizontal lines are the experimental results and the data points represent calculations carried out at various values of ρ (x-axis). The error bars represent the variation over the contact points. Only for a range of adhesion of approximately $\rho=5$ nm do all three lines cross the experimental results *simultaneously*. This means that while different values of ρ (with modified values of $W_{\text{adh,int}}$) can describe individual experiments, a simultaneous fit yields a range of adhesion around 5 nm. Note that the increase in pull-off force for small values for range of adhesion is due to the finite pixel size. Once the range of adhesion was fit, the data was scaled by a factor $W_{\text{adh,int}}$ to match the magnitude of the experiments. A second relative error minimization was performed to find the

best-fit value for $W_{\text{adh,int}}$ at the best-fit range of adhesion. Figure 23c shows the computed pull-off results calculated on varying points on the rough topography as a function of range of adhesion ρ . The work of adhesion used in this plot is the value that yields the best possible final fit.

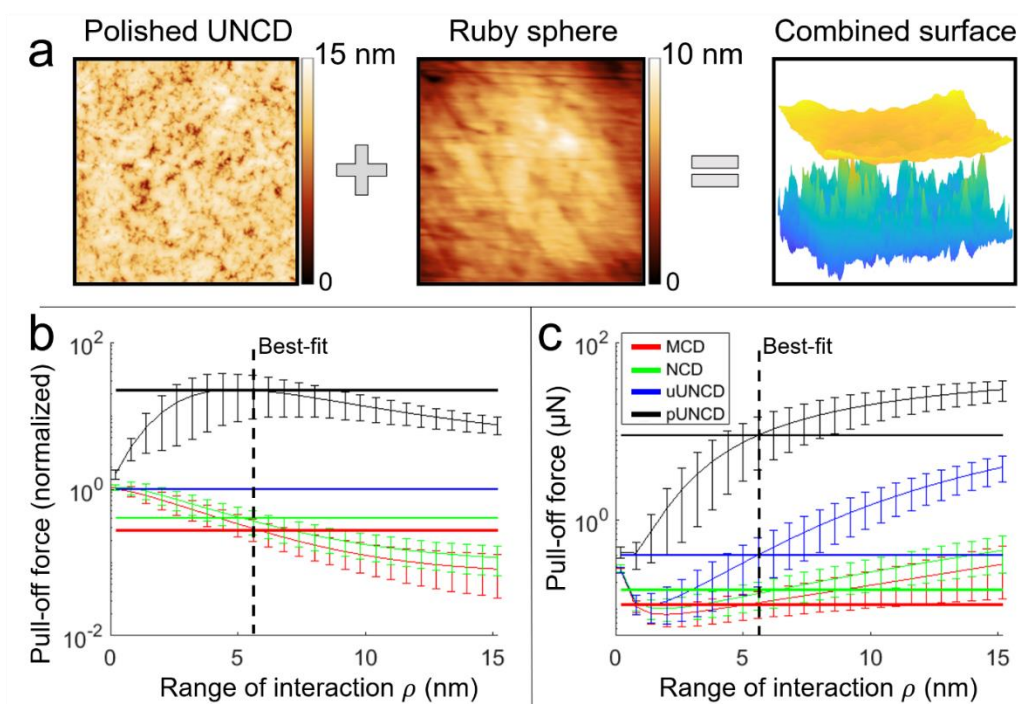


Figure 23 Computed pull-off forces were calculated by integrating an interaction potential over the combined roughness of the sphere and substrate (a). The best-fit value of range of adhesion was found by fitting to ratios of pull-off force (b), to eliminate the

It is clear from Fig. 23 that the range of adhesion strongly affects the values of adhesion force. Rougher surfaces, like MCD and NCD, are less strongly affected and can be fit over a wider band of values for ρ . Smoother surfaces, such as the polished UNCD, are more influenced by changes in ρ because the increasing range of adhesion enables more of the substrate to contribute to adhesion. This can be seen in Fig. 23c as a steeper slope for the smoothest polished UNCD

surface and for the unpolished UNCD. The majority of the adhesion contribution to the rougher surfaces (MCD, NCD) comes from just one or two asperities, and therefore larger values for range of adhesion do not lead to such significant contributions to the area of interaction.

There is only one combination of parameters that enables the best fit for all samples. The fit was evaluated by computing and minimizing the mean relative error (MRE) between the fitted and measured adhesion. The uncertainty in the fit was computed for all values around the best-fit value with $MRE < 0.1$. This match between calculated and experimental data was used to extract values for work of adhesion of $46.3 \pm 3.5 \text{ mJ/m}^2$ and range of adhesion of $5.6 \pm 0.5 \text{ nm}$. Previous adhesion measurements on rough contacts between diamond and other hard materials report similar values for the intrinsic work of adhesion by accounting for surface roughness [105], [128], [129].

The measured range of adhesion is much longer than is expected for typical atomic interactions such as covalent bonds or van der Waals forces, which are typically considered to have a range of adhesion around 0.3 to 0.6 nm [130]. However, there is prior nanoscale literature that supports a larger-than-expected value for range of adhesion. Using DLC-coated AFM tips, Grierson et al. have measured a range of adhesion between DLC and UNCD of 4-5 nm [131]. While for spherical (parabolic) tips the pull-off force does not depend on range of adhesion [23], their measurements exploited the non-parabolic shapes of worn tips, where pull-off force does depend on range of adhesion. In separate experiments also involving AFM pull-off measurements, Jiang et al. have measured a range of adhesion between UNCD and PMMA of 1.5-2.5 nm [105]. Similarly, in nanoindentation experiments adhesive forces were found to act over distances of 1.5-4.5 nm [132]. As mentioned in the introduction, the presence of long-range forces has also been

observed by DelRio et al. [18] in adhesion experiments involving silicon micro-cantilevers. The experiments showed contributions to adhesion from distances up to tens of nanometers.

The origin of these large values for range of adhesion is still in dispute. Previously proposed explanations involve electrostatic interactions due to contact charging [133]–[135], capillary adhesion [136]–[138], and Casimir forces [18]. First, electrostatic interactions have been proposed as a possible explanation because of the well-known phenomena of contact charging [14]–[17], [134]. While the detailed physical mechanism is still in discussion [139], the results are a net charge between the two materials that can result in measurable electrostatic interactions. In the present testing, these long-range electrostatic forces would be expected to be seen as measurable forces observed before and after contact. This can manifest as a tilting of the “out-of-contact” region of the force-displacement curve or as an earlier-than-expected snap-into-contact event as the charged sphere attracts the uncharged substrate in a new location. While such long-range interactions *have* been observed in other, unrelated testing where ruby tips were brought into contact with non-conductive substrates, the present substrates were boron-doped for conductivity, and the tester and substrates were electrically grounded to the vacuum chamber. The measured force curves in the present testing were similar to that shown in Fig. 8d, with no interaction forces observed until contact was initiated. Therefore, contact charging is not expected to have played a significant role in the present results.

A second common explanation for longer-than expected values for range of adhesion is capillarity. Water bridges across a contact can increase the area of interaction of a rough contact and are known to significantly increase the adhesive force. The relative humidity determines the presence and size of these capillary bridges, which in turn affect the adhesive force. The present testing was carried out in a dry atmosphere ($< 1\%$ RH). This is insufficient to eliminate all water

from the contact, but will limit its contribution. He et al. [140] showed that, even for hydrophilic surfaces, capillary necks could not form below a relative humidity of 20-40%. Numerical analyses [141] also suggests that capillary formation should not play a role in adhesion at low humidity. Therefore, capillarity is not expected to be the dominant factor in explaining the effect of topography on adhesion. Although the effects of capillary formation are grounds for future work.

A third common explanation for large values for range of adhesion is retarded dispersion, or Casimir, interactions. These forces arise due to the finite speed of electromagnetic interactions and typically act over ranges larger than a few nanometers, even up to tens of nm [18]. The present investigation is consistent with these findings, since the large micronewton adhesive forces cannot be explained without considering longer-range interactions. Furthermore, the smoother surfaces show a stronger contribution from these longer-range interactions, while these interactions play a less important role for the rougher surfaces, with fewer, sharper asperities in contact. However, the interaction potential used here does not explicitly account for any specific attraction mechanism. It is an empirical potential that elucidates the strength and length-scale of the interaction. In this case, those parameters are consistent with Casimir forces, but further investigation would be required to conclusively demonstrate the physical origin.

4.6.3 The Role of Permanent Shape Change in Adhesion of These Contacts

To specifically verify that permanent deformation can occur in these contacts, an additional investigation was performed with AFM imaging performed in the exact location of contact before and after an array test was performed. The standard adhesion test setup does not permit this precise knowledge of test location; therefore, an alternate custom micromechanical test setup was used, with a cantilever-based force sensor, but otherwise similar setup. A ruby sphere was polished, pre-

imaged in the AFM (Fig. 24b), and then used in an array test of adhesion against an NCD substrate. This testing repeated the 400 measurements in an array of locations from a typical adhesion experiment but used a pre-load of 20 μN (the minimum load of the alternate test apparatus). The apex of the sphere was imaged again after the test (Fig. 24c) and the location was matched to the pre-test image. The AFM imaging presented clear evidence of indentations at the tip of the sphere. The indentations were approximately 150 – 300 nm in lateral size, and approximately 2 – 10 nm in depth. These indentations were scattered across the tip of the sphere, with single indents concentrated around a region of multiple overlapping indents.

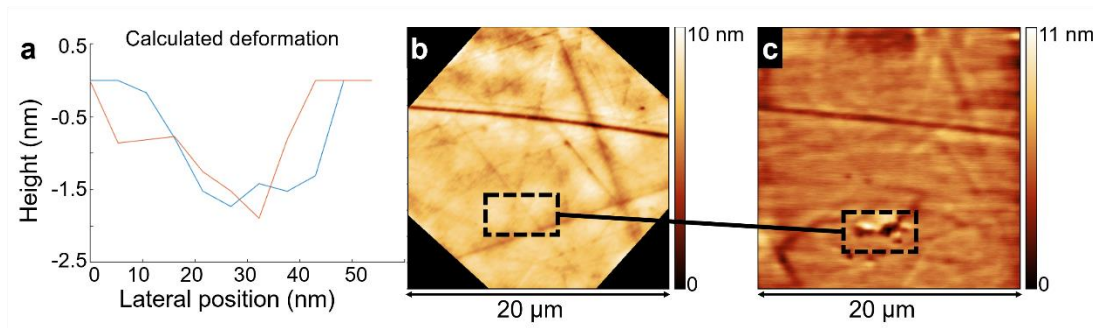


Figure 24 The computed deformation for a single adhesion test is shown in panel (a) with the red and blue lines representing x and y direction line scans respectively. The actual deformation of the ruby sphere after an array of adhesion tests is measured using AFM images taken at the sphere apex before (b) and after (c) testing. The images have been precisely located at the apex of the tip where contact took place, and fiducial markers have been used to orient the image. The after-test image confirm the presence of permanent deformation, as is assumed in the numerical modeling, seems to be in order-of-magnitude agreement with what would be expected after 400 tests in different locations, each with the deformation shown in (a).

The numerical modelling (recalculated at a preload of 20 μN) predicted deformations with a depth of approximately 2 nm and edge lengths of approximately 50 nm (Fig. 24a). The measurements are in reasonable agreement with predictions. The region of overlapping indentations makes it difficult to determine the size of a single indentation. However, there do appear to be single indentations scattered around that region. The measured deformation for what appear to be single indents had depths ranging from single nanometers to nearly 10 nm and lateral sizes for measured deformation of approximately 100 – 500 nm. The computed deformations are for a single adhesion test, while the experimental deformations correspond to the cumulative effect of 400 adhesion tests against different contact points. Therefore, the overall scales of deformations compare favorably, and likely indicate that the tallest asperities on the substrates are serving to permanently indent the polished spheres.

4.6.4 Determining the Most Relevant Length-Scales of Roughness

The numerical analysis in this investigation has demonstrated that adhesive interactions act over a length scale of greater than 5 nm, and that permanent deformation serves to increase contact area above the predictions of rigid or elastic calculations. These two factors may limit the impact of certain length-scales of topography on the total macroscopic adhesion.

To check the influence of different roughness scales, we repeated the pull-off force calculations on a variety of virtual surfaces, with different scales of roughness filtered out or included. This was accomplished by taking advantage of the all-scale measurements performed on the same substrates in Ref. [63] and combining them with the AFM measurements performed here. Since we do not have multi-scale measurements taken in the exact same location, we used the statistics of the random roughness to add smaller- and larger-scale roughness to the measurements.

Specifically, we started with an AFM image of the surface of the type shown in Fig. 21, then we superimposed artificially generated roughness that was created using a Fourier-filtering algorithm [74], [84] based on the measured PSD for that particular substrate. Therefore, these virtual surfaces are representative of the true multi-scale topography of each substrate. Then, from these multi-scale “master” surfaces, we filtered out different scales of roughness. Finally, we performed the numerical calculations on each of the filtered surfaces to compute the pull-off force and determine the sensitivity to different scales of roughness. The detailed approach of creating and filtering these surfaces is described in the next paragraph.

To add small-scale roughness, we first stitched the 512x512 pixel AFM scan using mirror images, leading to a 1024x1024 periodic topography. This stitched surface was first Fourier interpolated on an 8192x8192 grid (0.625 nm pixel size) and parts of the spectrum with wavelength smaller than $\lambda_T = 20$ nm were cut out. A randomly rough surface that follows the substrate PSD for wavelengths $\lambda < \lambda_T$ and has a constant roll-off above λ_T was added to this interpolated topography. Features below the varying cutoff wavelengths λ_S are then filtered out to check their effect on the calculated pull-off force. To add large-scale roughness, the AFM scan was again stitched to create a periodic topography, and this was stitched multiple times to yield an 8192x8192 (20 μ m linear size) grid. Fourier components at wavelengths bigger than $\lambda_T = 1\mu$ m were cut out. A randomly rough surface with spectrum following the substrate PSD for wavelengths $\lambda > \lambda_T$ and zero below λ_T was added to this topography. Features with wavelength above the varying cutoff wavelengths λ_L are then filtered out to check how they affected the calculated pull-off force.

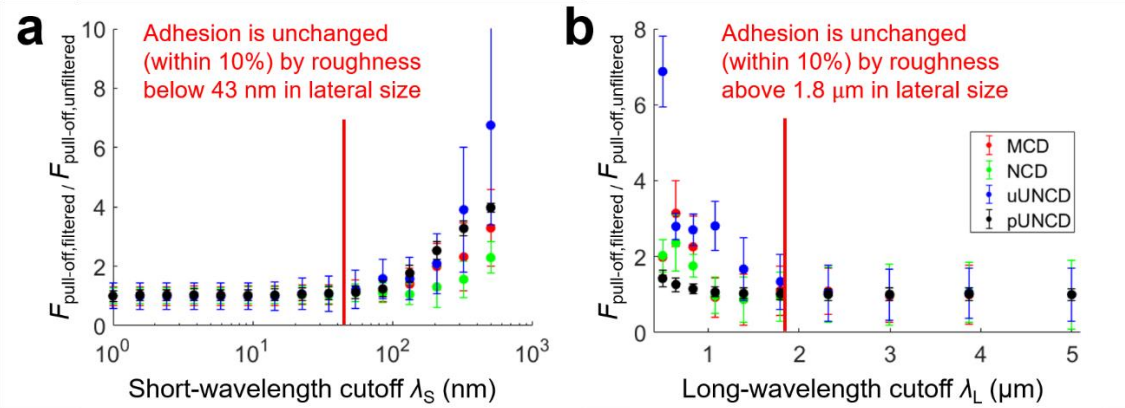


Figure 25 The contribution to pull-off force from various length scales can be directly demonstrated by recalculating pull-off force after filtering out small (a) and large (b) scales of roughness. Specifically, the pull-off force calculated from the filtered surfaces is normalized by the pull-off force calculated from the unfiltered surfaces. In panel (a), the x-axis indicates a short-wavelength cutoff, where all roughness below this size scale has been removed. A value near 1 indicates that there is almost no effect on pull-off force of filtering out roughness below that size scale. In panel (b), the x-axis indicates a long-wavelength cutoff, where all roughness above this size is removed. Here, a value of 1 indicates no contribution to pull-off force from roughness above that size scale

Figure 25 shows the change in pull-off that occurs when different length scales of roughness are filtered out. In Fig. 25a, which shows the effect of small-scale roughness, the leftmost datapoints represent the pull-off force computed on the unfiltered surface. As the short-wavelength cutoff (x axis) gets larger, more and more small-scale roughness is removed from the surface. Thus, the surface is perfectly smooth below this cutoff; the rightmost data points approach the pull-off force from a perfectly flat plane. The value of pull-off force remains constant (within 10%) until the cutoff wavelength reaches 43 nm. Removing roughness *above* this size scale has a strong effect on the adhesive force, but removing roughness *below* this size has almost no effect. Figure 25b shows a similar calculation, but now with long-wavelength roughness filtered out; thus, the rightmost datapoint represents a nearly unfiltered surface. As the long-wavelength cutoff

decreases, shorter and shorter wavelengths of roughness are removed from the surface, along with all wavelengths above the cutoff. The results show that, with removal of roughness with wavelength above approximately 1.8 microns, the adhesion remains constant (within 10%). Taken together, the two plots in Fig. 25 demonstrate that there is almost no effect on adhesion from roughness with lateral length scales smaller than 43 nm or larger than 1.8 microns. The critical finding of this analysis is that there is a certain band of length scales of roughness, 43 nm to 1.8 microns, that most-strongly affects adhesion in these materials; roughness outside of this band plays a secondary role in adhesion.

The explanation for this critical band of scales of topography may be different for the large and small scales. The unimportance of large-scale topography is likely linked to the area that is interacting with the sphere. Given a range of adhesion ρ , a sphere of radius R will interact with a flat surface within a disk of radius $r = \sqrt{D\rho}$. For $D = 500 \mu\text{m}$ and $\rho = 5.6 \text{ nm}$ we obtain a radius of $r = 1.7 \mu\text{m}$, almost exactly the wavelength above which large scale topography no longer matters. This shows that macroscopic pull-off forces are strongly affected by finite-size effects, and that the magnitude of pull-off forces will depend strongly on the sphere radius. This also means that the scales of roughness that matter are determined by the macroscopic contact geometry, as long as sphere radius R is much larger than typical scales of the roughness.

For the unimportance of small-scale topography, there are two effects that enhance each other: the large range of adhesion, and the effect of permanent deformation. The large range of adhesion (5.6 nm), which was determined from the numerical analysis, indicates that topography variations below this scale have a reduced contribution to adhesion. For example, for rigid surfaces with a sinusoidal gap of amplitude 2 nm, a range of adhesion of 0.5 nm would mean that only the contacting peaks contribute to adhesion and the rest of the surface is irrelevant; while a range of

adhesion of 5 nm would mean that all portions of the surface are adhering, with only small differences in relative contributions from different locations. An additional explanation is the effect of permanent shape change. The small-scale roughness has the highest local slope, and thus the highest surface stress. This means that the small-scale roughness will cause deformation, which smooths out these scales earlier than other scales, and reduces their contribution to macroscale adhesion.

4.6.5 Implications of the Present Findings

The results demonstrated that, for the macroscale adhesion of extremely stiff materials, the very smallest scales of roughness do not determine adhesion. This is in stark contrast to the adhesion of nanoscale contacts of hard materials [55] and to the adhesion of macroscale contacts of soft solids [79], both of which show a critical influence of smallest-scale roughness. While the present work draws on extensive roughness characterization at all scales using stylus profilometry, AFM, and TEM, in the end the AFM-scale roughness data (which covers the critical band of length scales discussed in the prior section) was sufficient to describe adhesion in these contacts. The introduction of smaller-scale roughness, as measured in the TEM, had little influence on the predicted adhesion. This means that parameters like RMS slope and curvature, that are most strongly influenced by the smallest-scale roughness, are less important for these hard-material contacts.

In these measurements, the larger scales of roughness were also less significant. This implies that measurements based on stylus profilometry, which is resolution-limited by the micron-scale radius of the tip, are not sufficient to predict and describe adhesion of these materials. It also implies that a simple scalar parameter such as RMS height is insufficient to determine macroscale

adhesion. We look forward to investigating this point further, with the goal to understand the generalizability of this result beyond the current experimental setup.

Another key result of the calculations for hard materials is that adhesion is dominated by the asperities at the very high end of the height distribution. This leads to highly variable extremes in adhesion that can far exceed common predictions based on the average asperity height. The adhesion distributions appear to be log-normal, with a long tail, which strongly impacts the mean adhesion value and leads to rare but significant ultra-high-adhesion events. This has strong implications for real-world applications, such as MEMS devices, which must overcome such surface forces and the threat of stiction. The shape of the measured distributions would suggest that any moving parts should be significantly overdesigned to ensure they can overcome the long-tail events.

Another important finding is that the experimental results were unable to be fit without the inclusion of permanent deformation. The assumption is that at some length scale, the contact pressure will overcome the hardness of one of the materials. Ruby, in our experiments, is the softer material. Whether this results in plastic flow or fracture, the contact area should evolve to support the preload applied and will be significantly larger than predictions from elastic models. In recent work in both SEM [142] and TEM [126], [127] experiments, plasticity in nanoscale ruby and diamond samples has been reported. These experiments found evidence of plastic flow, although the flow was likely facilitated by the large surface area. In the case of our ruby spheres, this type of flow seems unlikely. Simple experiments were performed to confirm the presence of small-scale damage on the ruby tip. These findings are supported by prior work demonstrating connections between nanoscale shape change and large-scale properties [143]. The nanometer-scale deformation is likely an important factor behind the presence of a small-wavelength cutoff

in the roughness that affects adhesion. The *effective* work of adhesion (that includes the effect of topography) of these surfaces varies by almost two orders of magnitude, from 0.08 to 7.15 mJ/m². These values for $W_{\text{adh,eff}}$ are calculated from the overall sphere geometry using spherical contact-mechanics models. Given the wide variability of the adhesion force between interfaces of identical large-scale geometry, it is not surprising that the effective work of adhesion varies so much. These variations, however, are not explained by simple analytical models, such as those based on a Gaussian distribution of asperity heights, nor those based on a balance between elastic and adhesive energy.

Common (elasto-)adhesion theories balance the elastic energy required for deformation with the interfacial energy (intrinsic work of adhesion) gained during contact [22], [75], [95], [144], [145]. In our case, the interfaces are so stiff that the deformation energy vastly exceeds any energy gain from making contact and we expect no pull-off force (or no stickiness [95]) in the “thermodynamic” limit of large surface areas and vanishing range of adhesion. In our case, the pull-off force is then determined by the interfacial stress carried by the intermolecular potential between the two surfaces and we can simply compute it by summing up these stress contributions (as we did in our numerical calculations); or in other words, the interface does not separate like a crack [22]. The explanation for the appreciable pull-off force is tightly linked to the long range (5.6 nm) of interaction extracted from this analysis.

4.7 Conclusions

By combining detailed measurements of topography, thousands of mm-scale adhesion measurements, and numerical integration of an interaction potential, we computed both the intrinsic material parameters governing adhesion as well as the contributions to adhesion from multi-scale topography. The intrinsic work of adhesion between ruby and polycrystalline diamond was found to be 46.3 mJ/m^2 while the range of adhesion was 5.6 nm . This large value for range of adhesion, along with the requirement for permanent deformation in the calculations, leads to a diminished role of small-scale topography on the macroscale adhesion of these hard contacts. While prior work on soft-material adhesion on the same substrates [79] demonstrated the important role of single-digit-nm topography on adhesion, the same is not true for the present measurements of hard-material adhesion. In fact, based on this analysis incorporating permanent deformation and the large range of adhesion, it has been demonstrated that there is a critical band of length scales of topography— 43 nm to $1.8 \text{ }\mu\text{m}$ —which plays the most significant role macroscale adhesion for these hard materials. The presence of this critical range of roughness scales is investigated further in chapter 5. In this chapter, the critical range of scales was determined through numerical analyses, the next step is to test this finding experimentally. In the next chapter, multi-scale roughness is intentionally patterned onto substrates, which are characterized in terms of adhesion and roughness. The effects of specific length scales of roughness on dry adhesion are explored.

5.0 Controlling Dry Adhesion Through Multi-Scale Surface Texturing Via Grayscale

Lithography

5.1 Chapter Overview

Despite extensive empirical measurement showing strong effects of surface texture on hard-material adhesion, advancements in this area have been mostly by trial and error and fundamental understanding has been elusive. This is partly due to the difficulty of systematically controlling and varying all scales of surface topography. The present work takes a unique approach in investigating this relationship between dry adhesion and multi-scale surface texturing. Rather than relying on natural surface variation to control roughness, as was done in the prior chapter, we intentionally impart rationally designed roughness into our substrates. The substrates are patterned using grayscale electron-beam lithography with multi-scale patterns onto silicon wafers, then the adhesion was measured using smooth silicon spheres as measurement probes. The data are analyzed with numerical calculations, using on a cohesive zone model, to characterize the fundamental adhesive interactions at the interface. As expected, patterns of roughness larger than the measuring probe did not have a significant impact on the adhesion. On the small scale, unlike for ruby-on-diamond, all roughness measured did seem to have a marked effect on adhesion. This investigation shows the impossibility of predicting adhesion using conventional, scalar topography metrics for rough surfaces due to the observed non-monotonic trends with all scalar parameters. For very smooth surfaces, expected trends arise in terms of adhesion and roughness. For surfaces with larger scales of roughness, more complex behavior emerges.

5.2 Introduction

Attempts to modify surfaces to tune adhesion have taken many different paths. Nanoparticle gradients used to study the effects of nanoscale roughness on adhesion and friction [5], [6], [146] found high adhesion at very large particle densities and very low densities, with minimum adhesion occurring at intermediate particle densities. In other experiments, roughness was controlled by altering growth parameters of CVD or ALD grown thin films [147]–[149]. These experiments have had good success varying surface roughness and compare contact properties with scalar roughness parameters. They report mixed results in terms of how adhesion changes with roughness and in terms of agreement with classical models. Lithographic patterning allows for complex shapes to be etched into a surface, usually in the form a repeating unit, such as nanopillars. Numerical study of textured surfaces [150] have reported increases in pull-off force that we're not monotonic and some scales of surface texture did not influence the value.

5.3 Limitations of Prior Work and Remaining Open Questions

Some of the literature has reported monotonically increasing adhesion with decreasing RMS height. Other studies have focused not on the height or magnitude of the roughness, but on its lateral dimensions and distribution. These investigations into the effects of roughness on adhesion have revealed a more complicated interplay between the height and lateral dimensions of roughness. Controlling surface topography of hard materials has generally been accomplished in two ways. The first is to create a pattern from a simple repeating unit. This can be accomplished by depositing nominally identical nanoparticles onto a surface or patterning with micro-pillars or

other shapes imparted by standard lithographic techniques. These methods impart roughness with well-controlled shapes, and results can often be fitted analytically to classical models, where the topography is also assumed to be composed of easy-to-describe shapes. This makes connecting adhesion to classical models as well as simulations very straightforward. The primary drawback of using these methods is that the roughness being imparted is typically of a single scale. We know, however, that roughness typically exists across *many* different scales can. Therefore, it is desirable to have models that account for this, and even take advantage of it.

Another common method involves a somewhat uncontrolled variation of surface roughness. Methods like sand blasting can be used to impart roughness that has a certain character [151]–[153], which is specific to the technique, but cannot be controlled as tightly as the methods mentioned above. Similar loosely controlled roughness variation has been accomplished via CVD [154][63] and ALD [149]. These methods are often successful in imparting multi-scale roughness but tend to produce topography that is far more difficult to describe than those produced by typical lithography or nanoparticle deposition.

In order to bridge the gap between these two types of roughness control, we have employed gray-scale lithography to pattern surfaces with highly controlled roughness across a wide range of length scales. Hierarchical patterns were etched into silicon surfaces to investigate their various contributions to macroscale adhesion. Specifically, a set of four computer-generated patterns of sinusoids were lithographically patterned into substrates. One “unfiltered” surface contained three 2D sinusoids of varying size scale: referred to as large (wavelength $\lambda = 19.5 \mu\text{m}$, amplitude $A = 10 \text{ nm}$), medium ($\lambda = 3.12 \mu\text{m}$, $A = 4 \text{ nm}$), and small ($\lambda = 0.5 \mu\text{m}$, $A = 1.5 \text{ nm}$). The other three surfaces contained the same pattern, but with one scale of sinusoid filtered out, referred to as

“large-filtered”, “medium-filtered”, and “small-filtered”. The adhesive force measured at each pattern was then correlated to the scales of roughness present on each pattern.

5.4 Methods

Grayscale electron-beam lithography (EBL) was carried out on a silicon wafer to create patterns with controlled roughness. This method has been described in [155], [156]. The exposure to the electron beam was varied between 255 (maximum intensity) and 1 (minimum intensity). The variable electron dose degrades the polymer resist to different degrees at different locations, such that when the resist is developed the pattern has been imparted into the resist itself. Then, when the resist-covered wafer is dipped into the etchant, the grayscale patterns are etched into the wafer.

Each pattern was created as a grayscale image with pixel intensity ranging from 1 to 255 to match the precision of the beam intensity. The images corresponded to a physical size of 100 microns and contained 3000 x 3000 pixels. The pixel size of 33 nm was designed to match the spot size of the e-beam.

The roughness of each pattern was characterized by optical profilometry (Bruker Countour-GT), stylus profilometry (KLA Tencor Alpha-Step IQ), and atomic force microscopy (AFM). Images with sizes between 200 nm and 20 microns were taken with AFM (Bruker Icon-V). For AFM, tapping mode images were taken with DLC coated probes. Stylus profilometry data was taken with scans lengths between 50 μm and 600 μm . Optical profilometry was used to take 2D images of each pattern between 50 μm and 600 μm edge length. TEM imaging of these samples is planned for future work (see section 7.3). Four patterns were etched to have specific, hierarchical

roughness. This roughness took the form of 2D sine waves. Three sinusoidal surfaces were designed into the patterns, they are outlined in table 8. Different combinations of these sinusoids were superimposed onto one another to create the four patterns on the wafer.

The grayscale lithography, as with any lithographic patterning technique, will inevitably impart roughness on the smallest scales that cannot be reliably controlled. In addition to tightly controlled sinusoidal roughness, there is also roughness on the small scale, inherent to the etching process. While the lithographic technique used gives us control over an incredibly wide range of length scales, we could not control roughness below the spot size of the beam, approximately 50 nm. Below this size, the etching process introduces its own topography variations. Variations at this size scale can be measured, but not easily controlled.

Adhesion measurements were taken using a MEMS-based force sensing probe (FT-MA02, FemtoTools, Buchs, Switzerland). Silicon hemispheres (goodfellow SI006805) with nominal radii of 250 μm were glued to the force probe to form the spherical tip for our adhesion measurements. Prior to mounting, the silicon hemispheres were polished from their as-received state down to a sub-nanometer roughness (RMS height < 1 nm) using a 0.05 μm alumina polishing suspension. Adhesion was measured between the silicon hemisphere and each pattern on the silicon wafer. The adhesion testing was carried out in a manner identical to that described in section 2.1.1.

5.5 Results

5.5.1 Topography Results

Figure 26 shows measurements of the 4 sinusoidal patterns. Line scans extracted from AFM, along with areal AFM data are shown as well as the PSD corresponding to each of the patterns. The PSDs were compiled from AFM, stylus profilometry, and optical profilometry.

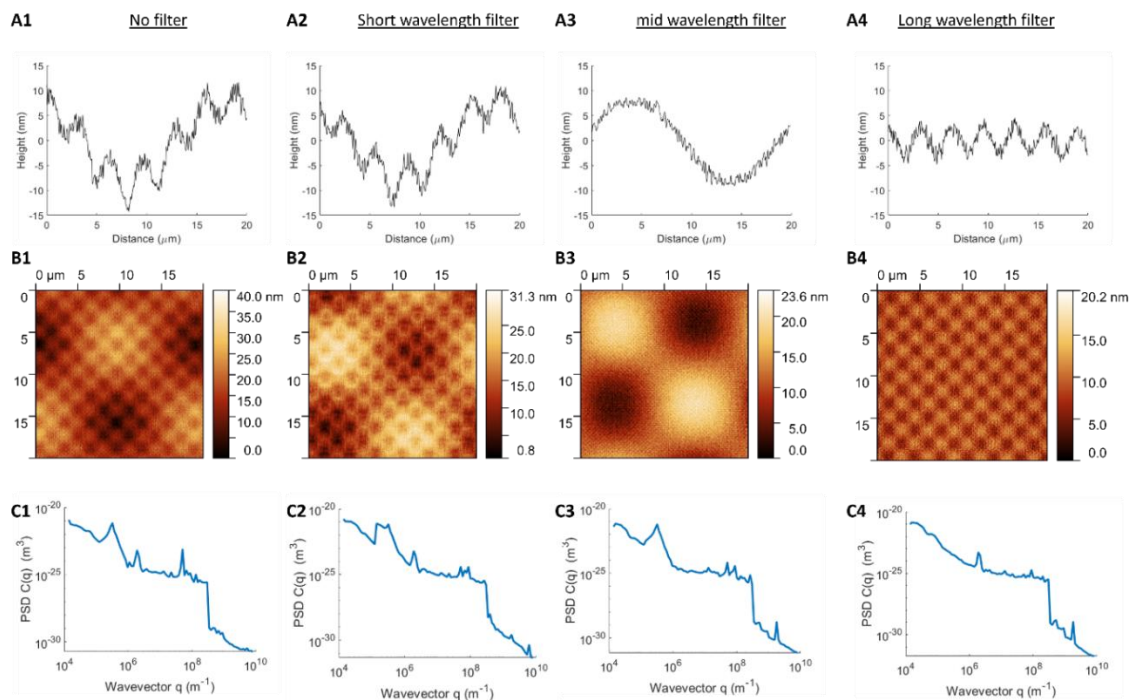


Figure 26 Lines scans from AFM of each patterned surface (A1-4), AFM scans of each patterned surface (B1-4), and the corresponding PSD for each (C1-4)

The unfiltered surface clearly shows the largest and medium scale sinusoids. The smallest scale is difficult to discern by eye, but the peak present in the PSD in panel C1 reveals its presence. Filtering the medium-scale sinusoid is very successful, as shown in Panels A3-C3, where the medium-scale roughness peak is absent in the PSD in panel C3. Similarly, the large wavelength

was successfully removed, seen in the PSD in panel C4, which is missing the peak at the largest scale. The short-wavelength peak is reduced, though not totally eliminated, in the short-wavelength filtered surface; this is likely due to raster-scan artifacts of the electron-beam tool, which also manifest at a similar size scale.

5.5.2 Adhesion Results, Measured and Numerical Calculations

The measured adhesion forces for each of the sinusoidal patterns is shown in figure 27. We refer to the pattern with all three sinusoids present as the “unfiltered surface”. The surface with the smallest scale sinusoid removed is called the “short-wavelength filtered surface”. The surfaces with the medium- and large-scale sinusoids removed are referred to as the “medium-wavelength filtered” and “large-wavelength filtered” surface respectively.

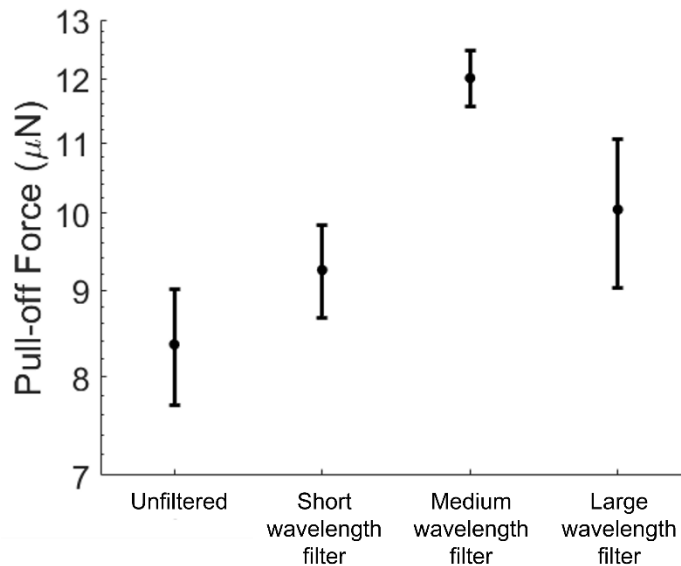


Figure 27 Adhesion measurements for the four sinusoidal patterns

The unfiltered sinusoidal surface has the lowest adhesion. The measured adhesion changed when different scales of roughness were removed. See table 6 for precise values from this figure. Removing the smallest-scale sinusoid increased the adhesion slightly. Removing the medium-scale roughness had the largest effect of any of the sinusoids, increasing adhesion by approximately 43% from the unfiltered value. Removing the largest scales of sinusoidal roughness had a lesser effect than removing the medium scales, but greater than removing the small scales.

Table 6 Adhesion values for the sinusoidal patterns with corresponding standard error

Pattern	Pull-off force (μN)
Unfiltered	8.36 ± 0.66
Short filter	9.25 ± 0.58
Medium filter	12.01 ± 0.45
Long filter	10.04 ± 0.89

To determine the statistical significance of these differences in adhesion, ANOVA testing was performed. The data was log-transformed to produce adhesion distributions that more closely aligned to the assumed normally distributed data. Log normal data has been reported in prior literature, although the physical origin remains unclear (see section 4.5). The results of this analysis are shown in table 7 below.

surfaces compared	p-value
unfiltered - short filter	0.019
unfiltered - medium filter	0.000
unfiltered - long filter	0.365
short filter - medium filter	0.045
short filter - long filter	0.840
medium filter - long filter	0.013

The null hypothesis of the ANOVA test is that the means of all datasets are equal. To interrogate specifically which means are equal and which are not, we apply a post hoc test, in this case we used the Tukey honestly significant difference (HSD) test, a standard post hoc test. We test the null hypothesis for each pairing of surfaces that the means are equal. With a significance level of 0.05, we reject the null hypothesis for all pairings except for the unfiltered - long filter, and the short filter - long filter. All other datasets have significantly different means. The medium filtered surface had a mean significantly larger than all others. While some means were not significantly different, gathering more statistics on adhesion would likely refine these tests and reveal significant differences.

5.5.3 Roughness Parameters Extracted from Measured Surfaces

Table 8 given common roughness parameters calculated from the PSD of each of the 4 sinusoidal patterns. These scalar metrics are commonly used in contact models to describe surfaces. The simplest attempt at relating roughness to adhesion would be to find some trends between the RMS roughness descriptors and the measured adhesion. Figure 28 shows how these quantities compare.

Table 7 RMS parameters extracted from the PSD of each of the sinusoidal patterns

Pattern	RMS Height (nm)	RMS slope (m/m)	RMS curvature (1/nm)
Unfiltered	7.26	0.42	7.05E-01
Short filter	7.69	0.34	5.30E-01
Medium filter	5.75	0.39	4.64E-01
Long filter	4.07	0.35	2.53E-01

5.6 Discussion

5.6.1 Correlating Adhesion Force to Conventional Roughness Metrics

When we look at the RMS metrics vs adhesion for the patterned surfaces, we do not see any strong trends in adhesion with RMS height, slope, or curvature. In fact, all trends with RMS metrics are non-monotonic and run counter to prior observations. For instance, while prior models and references predict that the pull-off force should decrease with RMS height, the present data shows the highest adhesion for an intermediate value and far lower adhesion for the “rougher” surfaces by any of the three metric shown in figure 28. Likewise, classical sphere-contact models may suggest decreasing adhesion force with increasing curvature, while recent work has suggested a decrease in adhesion with increasing RMS slope. Neither of these trends are consistently borne out in this data.

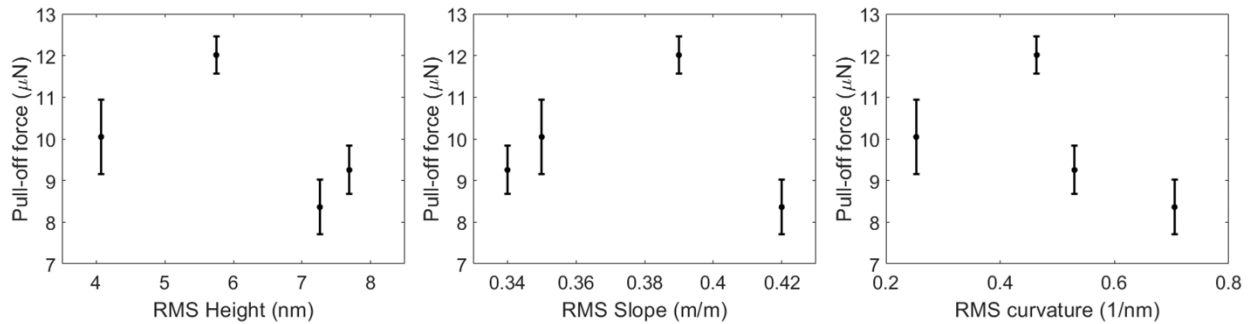


Figure 28 RMS roughness parameters vs. pull-off force for the 4 sinusoidal patterns

The lack of consistent trends demonstrates the difficulty of establishing clear correlations between macroscale adhesion and scalar parameters. In this case, the RMS values were calculated from the full spectrum of the PSDs shown in figure 26, such that all scales of roughness influence

these measured values. The values themselves include no information about the size scales that contribute most significantly to roughness, and therefore to adhesion.

5.6.2 Fundamental Properties of the Interface

To probe the details of the fundamental physical interactions taking place, we have performed a numerical analysis on the measured surfaces. By calculating a pair-wise interaction potential across AFM scans of the tip and substrates, we can extract fundamental parameters of the attractive interactions at the interfaces. In order to capture all of the scales of roughness present, the scans used had an edge length of 20 microns. This allowed us to capture one full period of the largest sine wave patterned.

To account for roughness beneath the pixel size (around 40 nm), we superimposed random roughness that was generated using the measured PSD of each of the sinusoidal patterns. The short-wavelength cutoff was set at 8 nm and the long wavelength cutoff was set at 2 pixels from the 20-micron scan (80 nm). The tip used a 20-um scan and had a smaller 2- μ m scan attached to the apex instead of using the interpolation. The numerical adhesion calculations were carried out as described in section 4.4.2.

Figure 29 shows the results of this calculation. The thick, horizontal lines represent the mean adhesion for each of the sinusoidal patterns. The thin lines with error bars represent the value of adhesion calculated by superimposing AFM scan of the Si tip onto various scans of each pattern. The x-axis represents the range of the interaction (ρ). By tuning ρ , we tune the shape of the interaction and find a value that allows us to accurately predict the measured values.

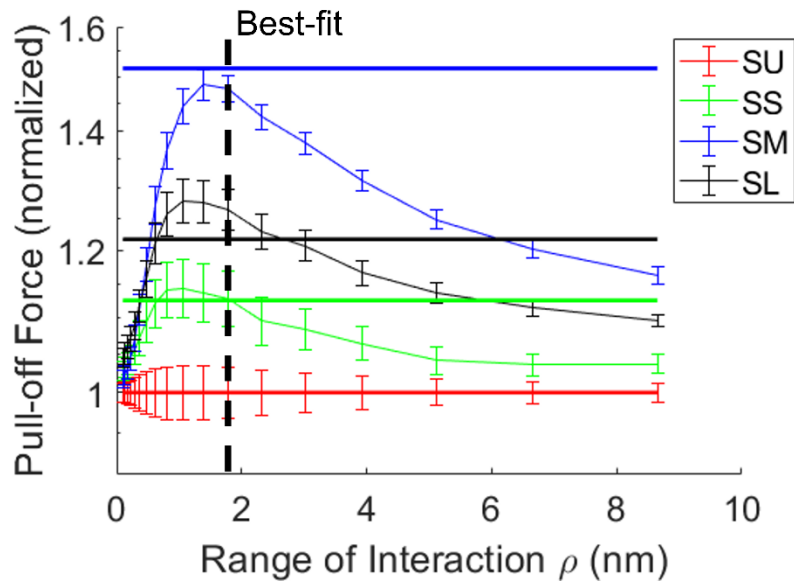


Figure 29 Computed pull-off forces were calculated by integrating an interaction potential over the combined roughness of the sphere and substrate. The best-fit value of interaction range was found by fitting to ratios of pull-off force, to eliminate the absolute value of work of adhesion.

The results shown in figure 29 show all adhesion values normalized by the value measured and calculated for the flat field reference. The fitting procedure fits the range of interaction using these normalized values as the work of adhesion falls out in normalization. Once the ratios of adhesion are fitted with a certain ρ , then the values are scaled using the work of adhesion to fit the absolute values of measured adhesion. The work of adhesion was fitted to $119 \pm 25 \text{ mJ/m}^2$ and range of interaction is $1.79 \pm 0.4 \text{ nm}$. This range is longer than expected for Van der Waals attraction, which is typically assumed to have a range of around 0.2 nm [130], but not nearly as long as the ruby-diamond value measured in the previous chapter (5.6 nm). As discussed, similarly long ranges of adhesion have been reported in the literature [80], [105], [131] and might be attributed to longer range Casimir forces [18]. The fitted work of adhesion is in good agreement with literature, although reports of intrinsic work of adhesion are sparse. Extracting a roughness-

dependent *apparent* work of adhesion is simpler and much more common, with typical values around 20 mJ/m^2 [157][158]. Some experiments using micromechanical cantilevers report the work of adhesion for silicon on silicon around 140 mJ/m^2 [159]. Also, the intrinsic work of adhesion has been calculated from the Hamaker constant to be 100 mJ/m^2 [160].

5.6.3 Understanding the Length Scales Governing Macroscopic Adhesion

Once roughness is imparted onto the surface, we see competing contributions to adhesion from all of the scales of roughness present. And as such, we would not expect any single or few-scale rough contact model to accurately represent our contacts. Here, we focus on determining which of the many scales present are most strongly influencing adhesion. If the most critical scales can be found, this would eliminate the need for accounting for every scale of roughness (there are almost always a continuum of scales present).

The pattern with all three sinusoids present produced the lowest adhesion. Removing remaining sinusoids only increased adhesion. We found that the largest increase in adhesion came from removing the medium-scale sinusoid. In the absence of the medium-scale sinusoid, adhesion was able to increase significantly. This reveals that the medium-scale sinusoid was the most effective scale of roughness in reducing adhesion.

The importance of large-scale roughness is closely tied to the geometry of the contact. The geometry used in this experiment is sphere-on-flat. The spherical countersurface to the substrate has a certain radius of curvature. We calculate the radius of curvature of each of the sinusoids present as well to determine how they might interact with the tip. The curvature data is shown in table 9 below. The radius of curvature of each sinusoid is calculated as the minimum radius of curvature, which corresponds to the peaks and valleys of the sine wave. The peak/valley radius of

curvature is calculated as $\text{radius} = \lambda^2 / (4\pi A)$, where λ is the wavelength and A the amplitude of the sine wave.

Table 8 Designed amplitudes and wavelengths for each of the sinusoidal patterns

Sinusoid	amplitude (nm)	wavelength (nm)	peak/valley radius (um)
small	1.5	500	4.2
medium	4	3120	61.6
large	10	19500	963.2

The radius of the tip is 250 μm . If the radius of a sinusoid is significantly larger than the tip radius, then the tip will be largely insensitive to that scale of roughness. The largest scale sinusoid has a radius of curvature nearly four times that of the tip. While this is larger than the tip radius, the results do demonstrate a difference in adhesion when this scale is removed. The critical factor is the radius of curvature of the roughness. If the substrate has roughness which can be probed completely by a tip of some radius, then that roughness should not influence adhesion as strongly as smaller scales. However, the local changes in curvature (from positive to negative) do seem to be influencing adhesion measurably.

For roughness similar to or smaller than the radius of the spherical probe, the probe will be restricted to contacting the peaks of the sinusoid and cannot access the valleys of roughness. In that case, the amplitude of the roughness serves to separate the tip from the bulk and thus reduce adhesion. We would expect the amplitude of the roughness to play an important role in adhesion in this size scale. Indeed, removal of the medium-scale sinusoid caused a 43% increase in adhesion, to the largest value measured on any surface. Removal of the smallest-scale sinusoid was associated with a 10% increase in adhesion.

5.6.4 Probing the Effects of Small-scale Roughness

We have a clear picture of how the large scales of roughness affect adhesion, but need to interrogate the effects of the smallest scales of roughness. The smallest scales of roughness patterned were the small-scale sinusoid with wavelength of 500 nm. Adhesion did increase when this scale was removed, so we can conclude that these scales are still within the range of scales that affect adhesion. However, with the current statistics on adhesion values, we were unable to prove that removing this scale had a significant difference in adhesion. Further testing will be needed to improve sample size and determine definitively whether this difference is real or not.

A 2D sinusoidal surface was created and consisted of a single sine wave with defined wavelength and amplitude. The scaling of the amplitude and wavelength was chosen to match that of the patterned surface (a Hurst exponent of 0.5). A smooth sphere of radius 250 μm was brought down into contact with the substrate at random locations 100 times. The interaction potential was summed over each pixel pairing between the substrate and the tip. Deformation was allowed in the form of a simple penetration hardness assumption. The surfaces were allowed to interpenetrate until the preload was able to be supported by the hardness of the material ($Y = 13 \text{ MPa}$ for Si [161]). The preload was 10 μN , chosen to match the experimental values for the sinusoidal adhesion measurements.

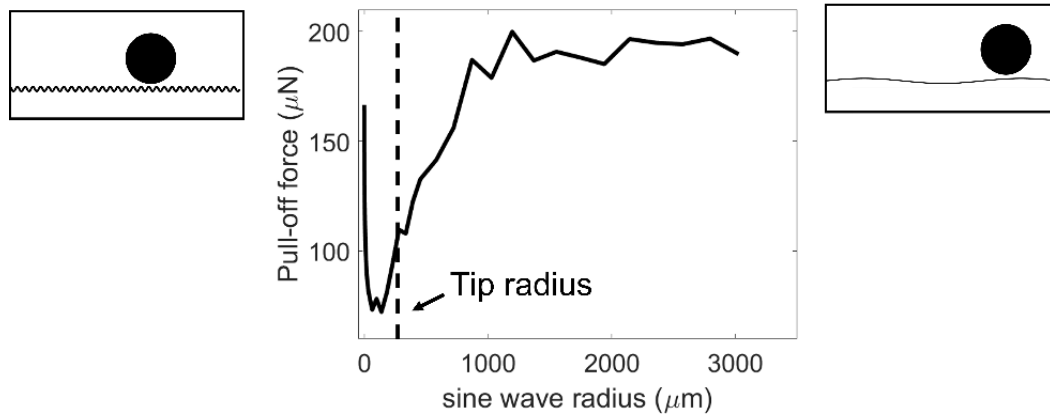


Figure 30 Pull-off force between a smooth sphere of 250- μm radius (dashed black line) and a sinusoidal surface with peaks of different radius (solid black line). The far right of the plot represents contact between a sphere and a nearly flat sinusoid. The far left represents contact between a sphere and a very rough, but low amplitude sinusoid, essentially returning to a flat substrate.

As expected, sinusoids with very large wavelengths produced adhesion very near to the smooth contact limit. As we shrink the wavelength and amplitude of the sinusoid, the adhesion begins to drop. A precipitous drop occurs as the curvature of the peaks/valleys of the sinusoid approaches the tip radius. The minimum in adhesion occurs just below the tip radius. After this point, the adhesion no longer decreases. The primary driving factor for adhesion reduction is the sinusoid's ability to separate the tip from the bulk. Once we get below the tip radius, the magnitude of the separation is what matters. As the amplitude continues to shrink, the tip approaches the bulk more closely and the surface begins once more to resemble a flat. This effect is suggested by Rabinovich for a single scale of roughness [101], [102]. The present work studies the generalization of this idea and to many scales superimposed onto one another. The calculations performed above represent the single-scale roughness analyzed by Rabinovich, while the patterned surfaces are multi-scale. In order to develop a better understanding of how multi-scale roughness affects adhesion, these calculations need to be extended to include multi-scale features.

5.7 Conclusions

The measured adhesion values and their variation with roughness reveal important factors governing adhesion in hard contacts. This investigation illustrates the difficulty in relying on scalar roughness parameters in predicting adhesion. Furthermore, we have demonstrated how roughness amplitude and wavelength (as reflected in a PSD), together with the strength and length-scale of the interaction potential, play a critical role in determining which scales of roughness will influence adhesion the most. In general, largest- and smallest- wavelength roughness contribute to macroscale adhesion, but the intermediate size scales seem to play the largest role.

6.0 Conclusions from Published Works

Taken together, the three original scientific contributions described above are targeted at addressing the three research questions addressed in Sect. 1.7. These were as follows:

- *First, what are the best characterization approaches and metrics to provide accurate input data for the investigation and prediction of roughness-dependent adhesion.*
- *Second, which length scales have the most significant impact on roughness?*
- *Third, what are the micro- or nano-scale physical processes that are governing macro-scale contact behavior and thus determining which length scales of roughness are most significant?*

More specifically, these works were aimed to test various aspects of the hypothesis that many scales of roughness contribute to adhesion, while a critical range of length scales plays the most significant role. This was accomplished by means of comprehensive adhesion and roughness characterization of many different surfaces and types of roughness. The following conclusions have been reached throughout the preceding chapters.

6.1 The Importance of Multi-scale Roughness Analysis

It has been demonstrated that the trends between scalar roughness parameters and adhesion are inconsistent, at best. In some cases, trends exist only across specific length scales and break down outside of these scales. This speaks to the fact that there are certain length scales that are

controlling adhesion in predictable ways, and some that current models do not account for and that affect adhesion alongside other scales. When roughness is considered to be multi-scale, there exist numerous methods to analyze the nature of such geometries. The present work has performed an original assessment and comparison of three such techniques, the variable bandwidth method (VBM), the autocorrelation function (ACF), and the power spectral density (PSD). The analysis determines that each one gives a partial picture of the roughness with its own advantages and disadvantages. Furthermore, each method can offer different insights into the complex nature of real surface roughness.

6.2 In Some Cases, a Specific Range of Scales Controls Adhesion

For the ruby-on-diamond surface, it was found that a certain critical range of scales controlled adhesion, while roughness outside of these scales had little or no effect. It is obvious that large scales of roughness, above the size of the features in contact, do not contribute to adhesion. However, it was also found that there was a small size scale, below which roughness had a diminished contribution. This was demonstrated by filtering out specific scales of roughness, with negligible effect.

However, by contrast, for the self-mated silicon contact, all size scales of roughness played a significant role in adhesion. Large, medium, and small-scales of roughness could be filtered out or added in, and each contributed significantly to the total macroscopic adhesion in the contact.

6.3 Fundamental Material Properties of Interfacial Interactions and Contact Properties

Determine Length Scales Relevant to Adhesion

The impact of smallest scales of roughness on adhesion, which was high in one case and low in another, is attributed to two key factors. The first is the length scale of the interaction between the two bodies. A key finding in this work is that, for ruby on diamond, the interaction range was 5.6 nm, far longer than the typically expected <1 nm of van der Waals attraction. This longer-than-expected interaction range means that height deviations that are smaller than this scale of roughness will have a diminished effect on adhesion. By contrast, in the self-mated silicon contact, the range of adhesion was shorter, only 1.8 nm. Here, a similar range of height deviations would have a far larger effect on the integrated interaction force.

The second key factor is the mechanical deformation and plasticity of the surfaces in contact. The yield strength, often characterized using hardness, determines how the surface handles loading and whether permanent deformation will occur. When the curvature of the roughness was high, as in the case of the nanodiamond surfaces, the smallest scales of roughness were permanently deformed, and therefore removed. Because the local contact stress depends on RMS slope, which itself is scale-dependent, then there should be a critical size scale at which the yield strength is reached. This will also provide a physical explanation for the small-wavelength cut-off in ruby-on-diamond.

7.0 In Process and Future Work

7.1 Study of Permanent Shape Change in Patterned Surfaces

To further aid in distinguishing adhesive-interaction effects from plasticity effects (as described in the previous sub-section), additional experimental investigation could be performed into the plastic deformation of the silicon-silicon contact. While permanent shape change was observed in ruby-diamond contacts, it is unclear if similar behavior would be observed in the patterned silicon-silicon contacts. More generally, permanent deformation was observed when the tips of asperities in contact with the tip were very sharp. This led to well-defined and highly localized deformation. When asperities are much broader, one might not expect to see such behavior.

The deformation observed in the ruby-diamond contacts was likely playing a significant role in the determination of the relevant small-scale roughness. A measurement identical to that performed in section 4.4 could be performed on the silicon tip used in adhesion testing. The presence or absence of permanent deformation would provide insight into how the geometry of the small-scale roughness influences permanent deformation. It is likely that the presence or absence of permanent deformation depends not only on the mechanical properties of the materials in contact, but also on the shape of the roughness present at small scales.

7.2 Friction: Sphere on Flat

The problem of rough adhesion has proven complex to measure and understand. Friction adds another layer of complexity to the problem, yet is critically important for real-world applications. While we take care in adhesion measurements to use only normal loading and unloading, friction testing introduces lateral displacements. With that, many complex considerations need to be considered. Some preliminary data on friction testing was carried out during this project, and the results were consistent, but not easily explained by classical models. Shown below in figure 31 are the results for friction testing between a ruby sphere and four different diamond substrates. The tip and substrates are the same ones used in the adhesion testing in chapter 4. The trends in adhesion differed from the predictions of several classical models or of simplifying assumptions. This likely points out the importance of multi-scale roughness descriptors; however an in-depth analysis has not yet been performed. While the adhesion methodology utilized a numerical contact calculation method to account for the multi-scale nature of the surfaces, the friction data would require a new approach to calculations which account for normal loading and sliding. Additionally, the observed indentations in section 4.4.5 suggest that there is likely some plowing friction at work in these contacts, which would complicate the application of a simple numerical integration of an interaction potential over a fixed contact geometry. Similar to the Sect. 7.1, the collection and examination of a tested sphere under an AFM after testing might reveal the presence of scratches on the surface. This would be useful in determining the mechanisms underlying friction in these and other hard contacts.

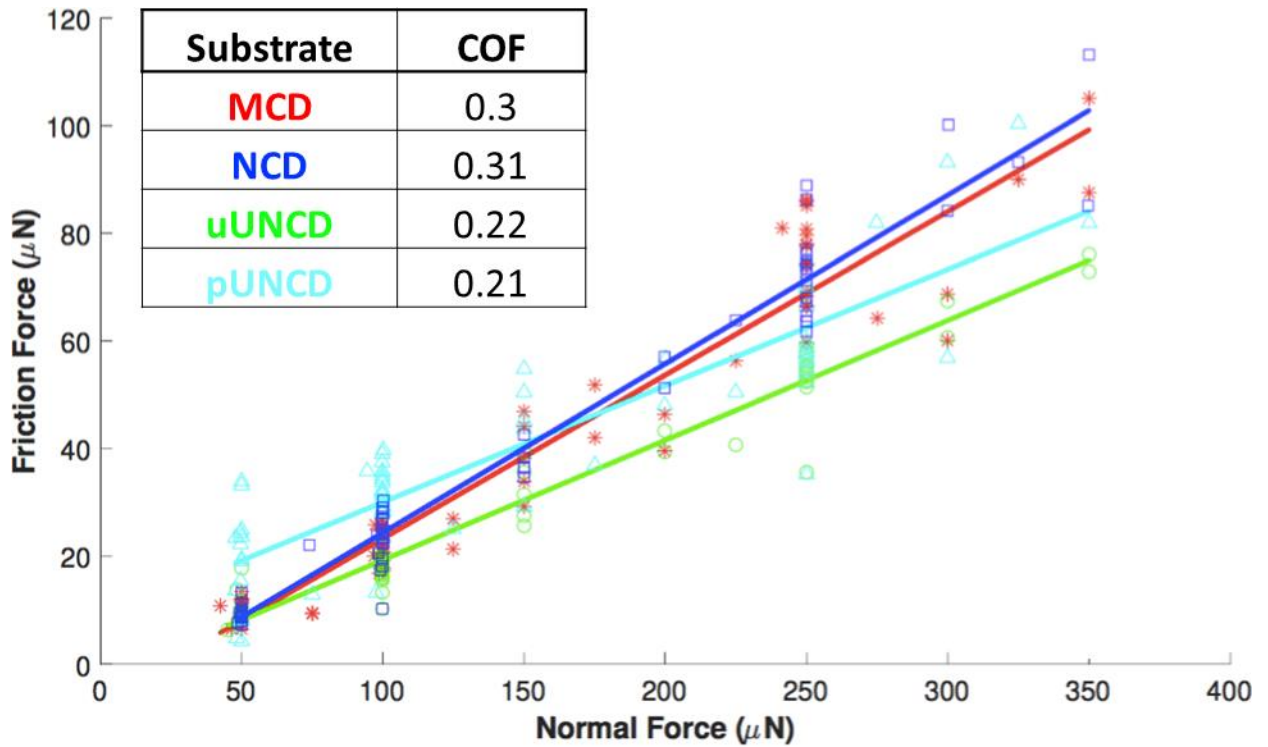


Figure 31 Normal force vs. friction force. The data is fitted with a linear trendline and the slope (the COF) is summarized in the legend.

7.3 TEM Analysis of Patterned Surfaces

The patterned surface created and analyzed in chapter 5 were characterized using stylus, optical profilometry, and AFM. TEM could not be performed on these samples. Although there are established methods for section and imaging films (or patterns) on a silicon wafer [49], this method could not be reliably applied to the patterned surfaces. The sectioning process does not offer control over the precise location of the cross-section. Ideally, we would look at a cross section that captures the peaks and valleys of each sinusoid. Using the current techniques, we would have no control over which portion of the sinusoid we were imaging. To overcome this, we plan to create a new set of patterns.

These new patterns will be identical to the current ones, with one critical difference. These new patterns will be etched onto TEM wedges [49]. These wedges are millimeters long, but are thin enough to be electron transparent. The patterns will be etched along this wedge, which will allow us complete control over which portion of the sinusoids we see in the TEM. It is important that we can characterize the peaks of the sinusoids, as these are what the tip will contact in most cases. With atomic-scale roughness data, we can strengthen our analysis and draw far more concrete conclusions concerning the relationship between roughness and adhesion in our patterned surfaces.

7.4 Future Directions

The topic of contact between rough surfaces is a very broad one. Throughout this project, my collaborators and myself have developed analysis and experimental methods to interrogate the effects of roughness on contacts between hard materials, and the potential for future work is great. This test setup developed here could be used to test the effects of ambient conditions, such as humidity, on adhesion, recall that in this project the focus was on dry adhesion. While dry understanding adhesion is important to learning about the fundamental mechanisms behind adhesion, humidity affects almost all large-scale contacts (although well-packaged microdevices can avoid humidity). Another path would be to vary the substrates themselves. This project focused on changing substrate topography to alter the adhesion. With no changes to the experimental setup, the substrate chemistry could be tuned. Surface chemistry is another important factor in adhesion and could easily be explored using the methods detailed here.

Finally, a direct extension of this work is the investigation into nanometer level shape change in contacts under adhesive loads. This topic was addressed in chapter 4, but should be given a more thorough treatment in future work. This would further our understanding of how adhesion can lead to deformation and destruction of small scales of roughness.

As a whole, this work and the future directions discussed in this section contribute toward a more complete understanding of the effects of surface roughness on contact properties. Pursuing these future directions will lead toward the development of well-designed and efficient interfaces that can be tuned to excel in any application.

Appendix A Single Sheets of Graphene for Fabricating Fibers with Enhanced Mechanical Properties

The majority of Appendix A is reproduced from Salim, M, Thimons L.A., Kim, M. et al, *Single Sheets of Graphene for Fabricating Fibers with Enhanced Mechanical Properties*, Phys. Chem. Chem. Phys. (2021) 10.1039/d1cp03238k

Appendix A.1 Chapter Overview

This chapter reports the fabrication and mechanical properties of macroscale graphene fibers (diameters of 10 to 100 μm with lengths upwards of 2 cm) prepared from a single sheet of single-layer graphene grown by chemical vapor deposition (CVD). The breaking strength of these graphene fibers increased with consecutive tensile test measurement on a single fiber, where fiber fragments produced from a prior test exhibited larger breaking strengths. Additionally, we observed a reduction of surface folds and wrinkles and their alignment to parallel the tensile tension direction. We propose that a foundation of this property are the plastic deformations within the fiber that accumulate through sequential tensile tension. Through this cyclic method, our best fiber produced a strength of 2.67 GPa with a 1 mm gauge length.

Appendix A.2 Introduction

Ever since the isolation of graphene was first reported,[1] researchers have investigated its remarkable mechanical properties—the intrinsic strength of graphene has been predicted to exceed that of any other material.[2] Coupled with its large specific surface area (2630 m²/g), graphene has proven to be a promising reinforcement material in composites.[3, 4] Similarly, the existence of graphitic-like atomic structures in related carbon-based materials have portrayed the benefits that their bonding environments have towards optimizing useful mechanical properties.[5, 6]

Early studies on the mechanical properties of graphene were performed at the nanoscale level.[4, 7-11] Nanoindentation measurements on graphene revealed an extremely high Young's modulus ($E = 1.02$ TPa) and intrinsic strength ($\sigma_{\text{int}} = 130$ GPa).[9, 10] Macroscale measurements have also been performed on graphene-based fibers, mostly of which are made using graphene oxide. In stark contrast to the nanoscale measurements, the macroscale graphene or graphene-oxide fibers show vastly different properties. [12-14] For example, the current highest reported mechanical ideal tensile strength for a graphene-based fiber is 3.4 GPa, a factor of 40 times smaller than the nanoscale value.[15]

This difference in mechanical behavior between the nano- and macroscale measurements is in part explained by the existence of critical defects in the material or structure.[7, 16] For 2D graphene, these include point defects, grain boundaries[17], and structural defects such as wrinkles and kinks, all of which have been shown to affect the local structure and intrinsic strength of graphene.[18-21] According to classic fracture theory,[22] the breaking strength of a brittle material is governed by these defects, which concentrate the stress to locally exceed the intrinsic strength of its atomic bonds. An example of this difference

between nano- and macro- scale measurements are included below for carbon nanotubes (CNTs). Nanoscale tensile tests of free-standing single-walled CNTs (SWCNTs) and multi-walled CNTs (MWCNTs) have revealed an ideal intrinsic strength of ca. 30 GPa and an elastic modulus of ca. 500 – 1000 GPa. [7, 23] Similar tests on MWCNTs were shown to produce intrinsic strength values equivalent to a single SWCNT with diameter equal to the largest MWCNT diameter—a result of poor load transfer between CNT layers in MWCNTs.[7, 24]

Macroscale measurements on MWCNT bundles have shown vastly different properties to their nanoscale counterparts, with an ideal tensile strength of 1.72 GPa and an elastic modulus of 0.45 TPa for lengths of ca. 2 mm.[16] Others have reported an ideal tensile strength of 1.2 GPa and elastic modulus of 16 GPa for double-walled CNT bundles for lengths of ca. 10 mm.[25] Macroscale measurements on SWCNTs also show the same reduced mechanical behavior to their nanoscale counterpart, with an ideal tensile strength of 1.0 GPa and an elastic modulus of 49 – 77 GPa for lengths of ca. 200 mm.[26]

The trend in these data shows that the mechanical properties of CNTs performed on the macroscale are universally orders of magnitude lower than when measured at the nanoscale; in that, the larger amount of material being measured, the more likely to have a critical defect that could lead to a failure is present somewhere along the materials length. [7, 16] Similar behavior has been observed for graphene oxide-based fibers. Some attempts have been made to reduce this discrepancy between nano- and macroscale properties.[27]

Graphene and/or graphene oxide (G/GO) flakes can be formed into layered structures and grouped into fiber-like assemblies. [12-14] The critical defects in these assemblies are related to both the local interlayer coupling and the G/GO flake alignment. The former

determines the nanoscale mechanical strength, and the latter determines the load balancing within the fiber assembly. Under load, the stress will be focused onto the G/GO flakes that are already aligned along the primary axis; at the nanoscale, the failure occurs where the interlayer coupling is the weakest. Based on this model, the mechanical properties of a G/GO flake assembly can be enhanced by increasing the interlayer coupling between each flake component. Experimentally, increasing the size of the G/GO flake improves the interlayer coupling, and increasing the alignment of the G/GO sheets can improve the load balancing within the assembly.[28, 29] Even so, these G/GO assemblies often require polymer binders and other stabilizers, e.g., during wet-spinning[12, 13] or blow-spinning,[30] in which binders coat the graphene/graphite flakes within the assembly in order to hold the resulting shape intact—further reducing the intra-layer interaction and therefore the potential fiber mechanical strength provided by the graphene flakes. Despite these related efforts in optimizing G/GO assembly structure and composition, the mechanical strength record for these macroscale fibers is ca. 3 orders of magnitude lower than the nanoscale value, with the current record at 3.4 GPa, through maximizing crystalline compactness of G/GO sheets, sheet ordering, and sheet size.[15]

Ideally, the best way to circumnavigate these issues would be to use a single continuous sheet of graphene along the entire length of the fiber. Such a system would eliminate in its entirety the issues of interlayer coupling and nanoscale load balancing, by using pristine nanoscale defect-free graphene. This can be done by using CVD-grown graphene—presenting a promising opportunity to further improve fiber structure and load balancing. The CVD method can produce meter-sized single-crystal graphene, far larger than any G/GO flakes.[31] CVD graphene can also be folded just like a macroscale object, and such

a process can produce highly aligned graphene sheets.[31] Therefore, forming fibers using large cohesive graphene sheets is a possible solution to resolve many of the mechanical limitations of graphene/GO flake assemblies. Although similar fibers which require polymer composites to maintain their structures have been reported, [32, 33] a polymer-free fiber made of a single sheet of CVD offers many advantages and has not been reported in the literature.

Herein, we report the fabrication of a polymer-free graphene fiber made from a single sheet of CVD graphene and report its mechanical behavior. The highest effective tensile strength we measured from these samples is 2.67 GPa.

Appendix A.3 Results and Discussion

The graphene fibers were fabricated by physically folding a single sheet of single-layer CVD graphene into a 1D-fiber shape in an accordion-like pattern, Figure 32. Additional details on CVD graphene synthesis and characterization is provided in the supplementary information (Figures S1 and S2). During folding, CVD graphene was supported by a thin layer of polymethyl methacrylate (PMMA). This polymer coating was decomposed and removed by annealing the fiber at 420 °C after folding, above the thermal decomposition temperature of PMMA (390 °C), Figure S3. The accordion-like folding pattern (Figure 32) was selected for maximizing the surface area of exposed PMMA in order to prevent the decomposition products from being trapped within the fiber structure upon heat treatment. As an example of a poor folding pattern, thermally annealed rolled/scrolled fiber structures,

are shown in Figure S5—where the decomposed PMMA becomes trapped between the rolled graphene layers, resulting in bubbled structures on the surface and a hollow fiber. Since only one single CVD graphene sheet was used for each fiber, the dimensions of the flat graphene sheet were used to calculate the ideal cross-sectional area of the graphene in the fiber (A_{graphene}) by using the width (prior to folding) of the graphene sheet and the thickness of graphene (0.335 nm). For a 1-cm-wide CVD graphene sheet, the ideal cross-sectional area is $3.35 \mu\text{m}^2$.

Scanning electron microscope (SEM) images of annealed graphene fibers, Figure 33, folded in an accordion-like pattern, reveal that this folding pattern produces a cohesive straight fiber that does not exhibit any bubbled or hollow structures like that in the annealed rolled fibers, Figure S5. This is due to accordion pattern allowing for decomposition/removal of PMMA without being trapped between graphene layers. After annealing, the typical nominal diameter of the fibers was between 10 – 100 μm . The presence of both lateral and axial folds is observed in the final annealed fiber. The initial length of the graphene fibers (L_{fiber}), after fabrication, was measured with a digital microscope and were typically within 0.1 – 2.0 cm.

These graphene fibers were mounted onto a custom uniaxial testing setup (Figure S4), where both the force, F , and displacement, ΔL , along the fiber were measured. The fibers were put under tensile tension until breaking, and the resulting broken fiber segments were re-mounted and testing was repeated. Ideal stress was calculated as F/A_{graphene} , where A_{graphene} is the cross-sectional area of the graphene fiber calculated using the initial pre-folded CVD graphene sheet width and atomic thickness—similar to the method used for the previously reported measurements on CNTs. Strain was calculated by $\Delta L/L_0$, where L_0

was the initial fiber length, as described in the Supplementary Information. The modulus of the fibers, K_{fiber} , was determined from the slope of the linear portion of the stress-strain curve, and the tensile breaking strength was calculated from the stress at the time of breaking.

We observed two distinct types of fracture mechanisms in the graphene fibers upon tensile loading. The first type, herein referred to as brittle, is associated with rapid breaking of the fiber after fracture initiation. In this case, the corresponding force-distance curve shows an instantaneous vertical drop in the force from breaking strength to baseline. The second type, herein referred to as ductile, involves a gradual propagation of the fracture across the width of the fiber, the initiation of which correlates to a plateauing of the measured force in the force-distance curve.

Our measurements revealed that brittle fractures correlated with a lower breaking strength and were associated with longer fibers. An example of such a fracture behavior is shown in Figure 34 and Video S1, for a fiber that is ca. 3 mm in length and an ideal breaking strength of 0.475 GPa.

Ductile fracturing was only observed on smaller fragments produced after multiple cycles of tensile measurements. This ductile fracture mechanism resulted in a higher tensile strength in comparison to the brittle-fracture samples (Figure 35, Video S2). Top of Figure 35 (Frames 1-3) depicts three video frames during the tensile testing of a ductile fiber. Frame 1 was taken after the macroscopic bends along the axis were removed by the axial movement of the tensile testing setup, forming a more linear fiber. Changes in the diameter and length from this point are a combination of further unbending and elastic or plastic deformation inside the fiber, which was measured optically. Frame 2 was captured right

before the graphene fiber fractured, whereby the ideal breaking strength was calculated to be 2.67 GPa. Frame 3 shows the fiber after breaking, where the sum of the lengths of the broken pieces is larger than the L_{fiber} value of Frame 1, representing some plastic deformation which occurred during testing. These results show a total strain to failure for this wire of 11.4%, where both plastic and elastic deformation plays a role. The stress-strain curve for this test is shown in Figure 35, with a measured modulus K_{fiber} value of $61.85 \text{ GPa} \pm 2.26 \text{ GPa}$.

The tensile response of the fiber fragments is affected by the plastic deformations of previous tensile tests. Figure 36 shows the plot of the tensile strength measured on two fibers and their resulting fragments. In both cases, we observed a gradual increase of breaking strength for all sequential tensile measurements, where the longest fiber had the lowest breaking strength, and the shortest fragment had the largest breaking strength. We conjecture that this behavior is partially explained by the fibers fracturing and breaking at the location of their most critical flaw(s) during uniaxial testing; this results in fiber fragments which must therefore only have flaw(s) of equal or lesser nature. The final measurement of the fiber in Figure 36A, indicated by a green arrow, is a fragment which exhibited ductile fracturing behavior. We conjecture that straightening and alignment of folds during repetitive uniaxial tests may also be a cause for the mechanical improvements we observe. Comparing the surface morphology of pre- (Figure 33 A/B) and post- (Figure 33 C/D, Figure S6) tensile testing reveals that during the uniaxial tensile tension there is a reduction in folds/wrinkles orthogonal to the pulling axis, as well as alignment of folds/wrinkles parallel to the pulling axis. Analogous observations have been reported

G/GO fibers during stress relaxation upon uniaxial tension. [15, 34] Similar enhancements have been observed for GO films during cyclic tensile tests.[33]

Figure 37 shows tensile strength measurements of fibers as a function of the fiber length. There is a large variation in the average breaking strength for brittle fractures ($0.45 \text{ GPa} \pm 0.20 \text{ GPa}$). The fibers exhibiting ductile behavior were all smaller fragments of a parent fiber. However, this behavior cannot simply be described using the conventional weakest-link statistics because there was no generalized correlation between length of the fiber and fracture strength (as is predicted from a statistical distribution of flaw sizes). We note that the existence of two types of graphene fracture behavior has been previously reported (denoted in that work as bad and good).[35]

The separation of graphene fiber fragments into brittle and ductile regimes is presumed to be a function of several factors, which includes the number of limiting critical defects and the structure and quality of the graphene fiber in which the crack propagates. Crack propagation likely occurs through an unzipping mechanism, which has been previously reported for CVD graphene.[35] Hwangbo et al. also reported that this unzipping fracture mechanism can be heavily influenced by the surrounding environment.[35] We conjecture that fracture in the graphene is occurring locally along the most energetically favourable paths, such as grain boundaries and defects. Control of these grain boundaries and defects may lead to further enhancement of mechanical properties.[36] We believe that the force plateau is achieved through a global load-rebalancing mechanism. Although the graphene sheet is highly folded along the axial direction, other folds are in random orientations, so different regions of the sheet will experience different degrees of tension. These folds could be present at the fracturing location and oriented in a way that applied tension could not be

distributed; this partial loading would reduce the effective A graphene and calculated ideal tensile strength. As a higher-tension region fails, other portions of the fiber will take up the load. As an example, Figure 38 shows a schematic of adjacent regions of the sheet with high and low stiffness due to different degrees of folding. When the crack propagates into a localized region that is under lower stress, the crack will arrest, preventing catastrophic failure and transferring the load to other regions. The tensile strength and modulus of our graphene fiber system could be simulated theoretically on a size scale under computational efficiency limits, similarly to previously reported fracture mechanics modelled for graphene. [21, 37]

We note that for the fibers exhibiting ductile fracture behavior, the force remains relatively constant as the graphene fracture propagates. While the graphene unzips, the true cross-sectional area of the graphene in the fiber is continuously reduced. Therefore, the measured breaking strength values are still an underestimation of the ideal strength of the graphene fibers.

Appendix A.4 Conclusions

We developed a fabrication technique for single sheets of CVD graphene into macroscale graphene fibers and measured their mechanical properties. Our results highlight the potential of using CVD graphene to fabricate high performance macroscopic structures. The effective tensile strength of our graphene fibers increased with decreasing length of the fiber for repeated tests on a single fiber. Graphene fibers exhibited either

ductile or brittle fracture mechanics. We believe that the lasting plastic deformations built upon sequential tensile tension plays a key role in these properties. The results suggest that optimizing interlayer coupling is necessary to control mechanical efficiency—between increasing interlayer coupling to improve load transfer and balancing and limiting it to prevent large variations of tension within a sheet that led to premature fracture. The average ideal breaking strength for fibers exhibiting ductile behavior was $1.75 \text{ GPa} \pm 0.62 \text{ GPa}$, with the largest breaking strength of 2.67 GPa .

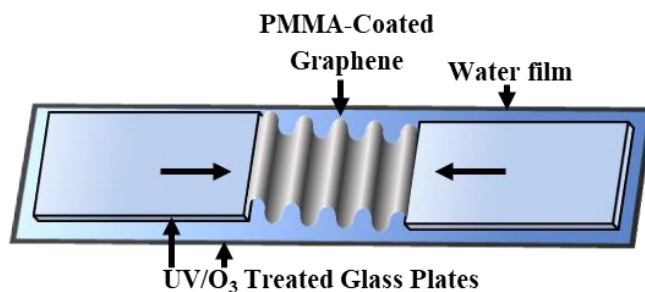


Figure 32 Schematic of folding process for PMMA-coated graphene in an accordion-like pattern. Glass plates were treated with UV/O₃ prior to use. Wrinkles formed in the graphene sheet during compression along the width of the graphene sheet and remained folded as the sheet was compressed further.

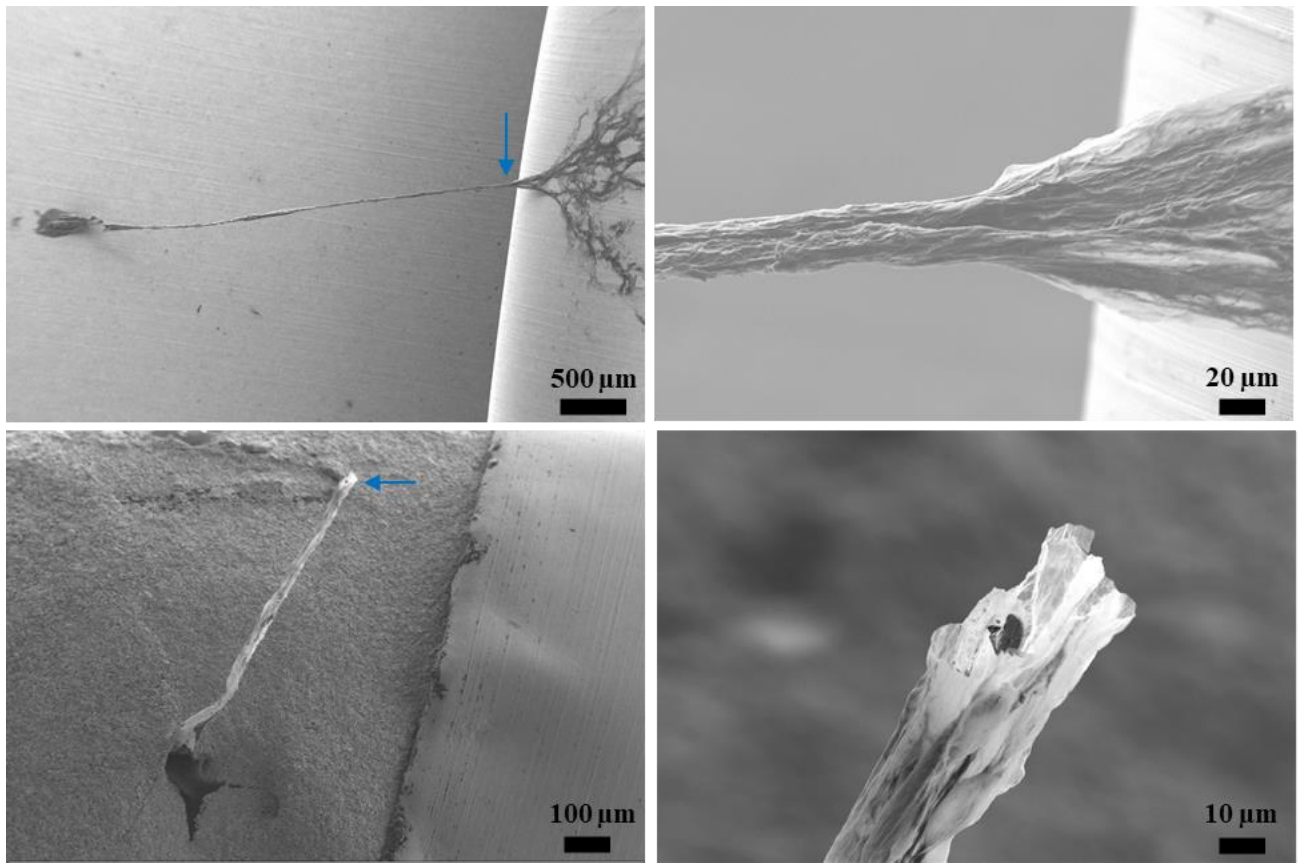


Figure 33 SEM images of two graphene fibers. A suspended graphene fiber is shown after annealing on a copper substrate to remove its polymer backing. B, zoom in of graphene fiber from panel A (location marked with an arrow) is shown at a higher magnification and has a diameter of approximately 25 μm . C, a broken graphene fiber after tensile testing. Conductive silver paste was used to coat the mounting adhesive for SEM imaging. D, zoom in of graphene fiber from panel C, (location marked with arrow) showing the fracture edge after tensile testing.

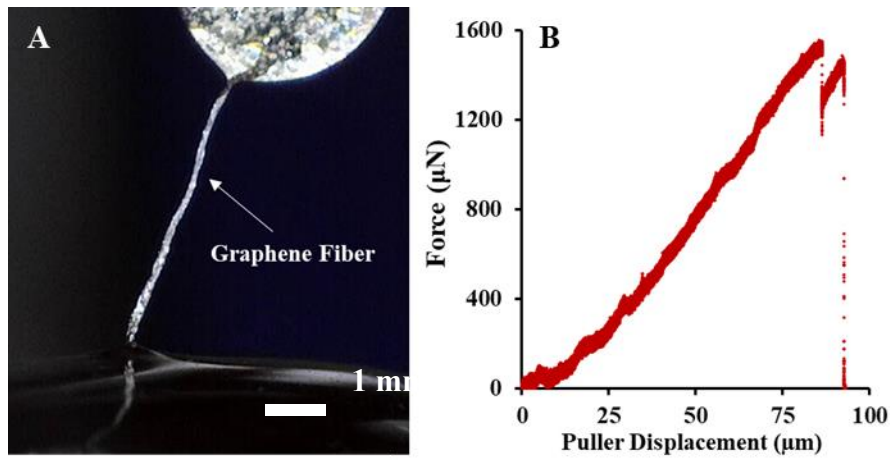


Figure 34 Macroscale graphene fiber tested in uniaxial tension. **A**, optical image of graphene fiber ($A_{\text{graphene}} = 3.18 \mu\text{m}^2$, $L_{\text{fiber}} = 2952 \mu\text{m}$). **B**, Force-displacement plot of uniaxial tensile test (puller displacement rate $r_p = 0.50 \mu\text{m/s}$). This fiber exhibited brittle fracture, with a tensile strength of 0.475 GPa.

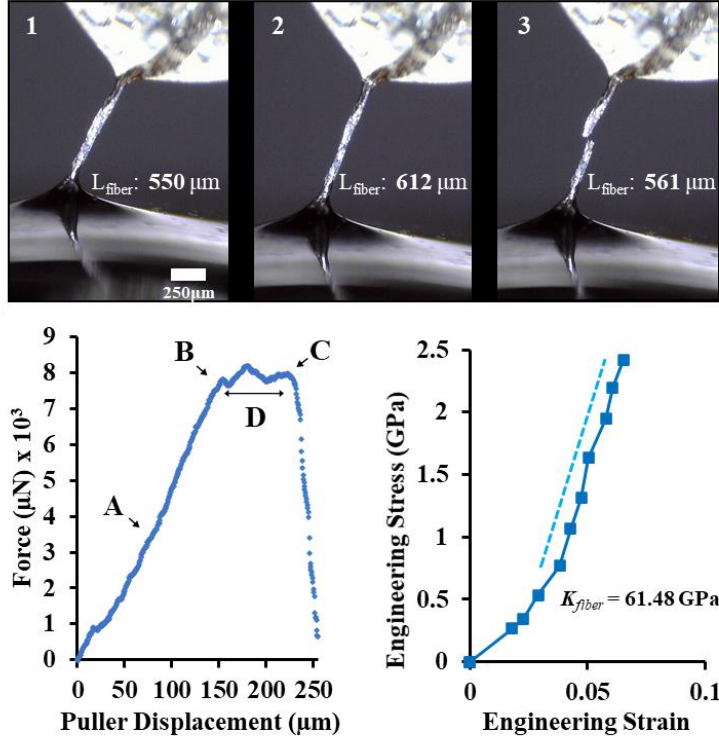


Figure 35 Uniaxial tensile testing of graphene fiber exhibiting ductile fracture. ($A_{\text{graphene}}=1.84 \mu\text{m}^2$, $r_p=0.50 \mu\text{m/s}$) Top: Three frames (1-3) of a graphene fiber uniaxial tensile test. (Frame 1) Graphene fiber ($L_{\text{fiber}}=550 \mu\text{m}$) after straightening the macroscopic bends in the fiber; (Frame 2) Fracture initiation ($L_{\text{fiber}}=612 \mu\text{m}$), (Position B); (Frame 3) Post-fracture ($L_{\text{fiber}} = 561 \mu\text{m}$). Bottom: Force-Distance plot (Left) of graphene fiber depicted in Top. A-B represents region of the stress-strain curve (right plot) used to calculate the fiber modulus $K_{\text{fiber}} = 61.48 \text{ GPa} \pm 2.26 \text{ GPa}$. Point B refers to the fracture initiation of the graphene fiber. The maximum force at point C can be used to calculate breaking strength. The graphene fiber fractured in an unzipping pattern (see Video S2), which is also evident by the gradual (rather than immediate) reduction to zero force. Point D refers to the plateau region of force during unzipping of fiber.

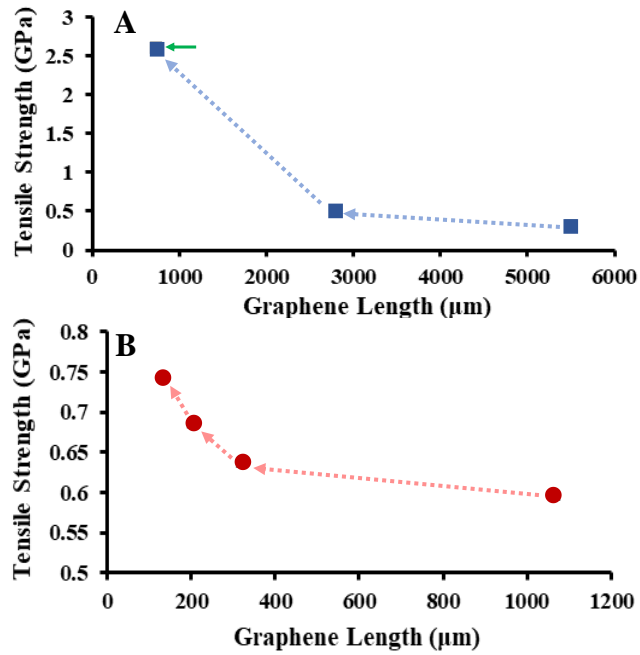


Figure 36 Breaking strength of graphene fibers as a function of fiber length. Dotted arrows indicate order of sequential uniaxial tensile tests on the same fibers with $A_{\text{graphene}} = 3.2\mu\text{m}^2$ (A) and $A_{\text{graphene}} = 5.2\mu\text{m}^2$. (B). Green arrow indicates a measurement where ductile fracture behavior was observed during tensile testing.

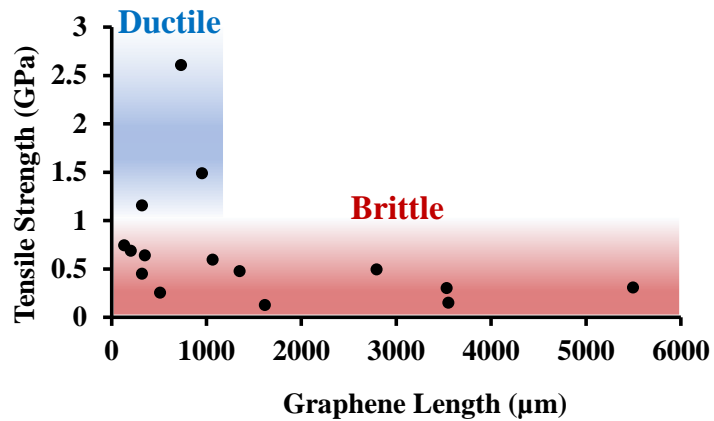


Figure 37 Breaking strength of parent and fragment fibers. Three fiber fragments exhibited ductile behavior and exhibited the largest measured breaking strengths. Brittle fracturing behavior was observed for most fibers.

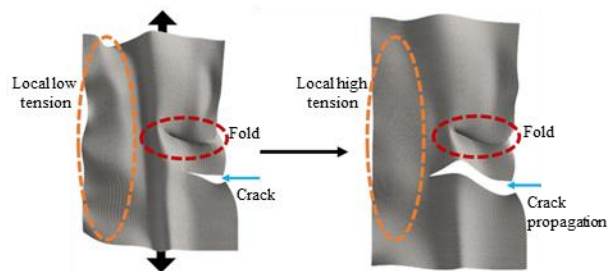


Figure 38 Possible mechanism for the observed plateauing behavior in ductile fibers. The folded graphene region is at high stress (left), causing crack formation. This crack arrests when it approaches the local low-tension region-- which is not folded and therefore under lower stress at the same extension. It is only after significant further extension of the puller (right), that the graphene reaches a sufficient stress to continue the propagation of this crack. During that extension, the load is thought to be constantly rebalancing between kinked portions, preventing catastrophic failure.

Appendix A.5 References

1. Novoselov, K. S.; Geim, A. K.; Morozov, S. V.; Jiang, D.; Zhang, Y.; Dubonos, S. V.; Grigorieva, I. V.; Firsov, A. A., Electric field effect in atomically thin carbon films. *Science* 2004, 306 (5696), 666-669.
2. Zhao, Q.; Nardelli, M. B.; Bernholc, J., Ultimate strength of carbon nanotubes: A theoretical study. *Physical Review B* 2002, 65 (14), 144105.
3. Ajayan, P. M.; Tour, J. M., Nanotube composites. *Nature* 2007, 447, 1066.
4. Cao, G., Atomistic Studies of Mechanical Properties of Graphene. *Polymers* 2014, 6 (9), 2404-2432.
5. Bakoglidis, K. D.; Palisaitis, J.; dos Santos, R. B.; Rivelino, R.; Persson, P. O. Å.; Gueorguiev, G. K.; Hultman, L., Self-Healing in Carbon Nitride Evidenced as Material Inflation and Superlubric Behavior. *ACS Applied Materials & Interfaces* 2018, 10 (19), 16238-16243.
6. Högberg, H.; Lai, C.-C.; Broitman, E.; Ivanov, I. G.; Goyenola, C.; Näslund, L.-Å.; Schmidt, S.; Hultman, L.; Rosen, J.; Gueorguiev, G. K., Reactive sputtering of CS_x thin solid films using CS₂ as precursor. *Vacuum* 2020, 182, 109775.
7. Qian, D.; Wagner, G. J.; Liu, W. K.; Yu, M.-F.; Ruoff, R. S., Mechanics of carbon nanotubes. *Applied Mechanics Reviews* 2002, 55 (6), 495-533.
8. Yu, M.-F.; Lourie, O.; Dyer, M. J.; Moloni, K.; Kelly, T. F.; Ruoff, R. S., Strength and Breaking Mechanism of Multiwalled Carbon Nanotubes Under Tensile Load. *Science* 2000, 287 (5453), 637-640.
9. Zhang, Y.; Pan, C., Measurements of mechanical properties and number of layers of graphene from nano-indentation. *Diamond and Related Materials* 2012, 24, 1-5.

10.Lee, C.; Wei, X.; Kysar, J. W.; Hone, J., Measurement of the Elastic Properties and Intrinsic Strength of Monolayer Graphene. *Science* 2008, 321 (5887), 385-388.

11.Akinwande, D.; Brennan, C. J.; Bunch, J. S.; Egberts, P.; Felts, J. R.; Gao, H.; Huang, R.; Kim, J.-S.; Li, T.; Li, Y.; Liechti, K. M.; Lu, N.; Park, H. S.; Reed, E. J.; Wang, P.; Yakobson, B. I.; Zhang, T.; Zhang, Y.-W.; Zhou, Y.; Zhu, Y., A review on mechanics and mechanical properties of 2D materials—Graphene and beyond. *Extreme Mechanics Letters* 2017, 13, 42-77.

12.Zamani, S.; Won, J. S.; Salim, M.; AlAmer, M.; Chang, C.-w.; Kumar, P.; Amponsah, K.; Lim, A. R.; Joo, Y. L., Ultralight graphene/graphite hybrid fibers via entirely water-based processes and their application to density-controlled, high-performance composites. *Carbon* 2021, 173, 880-890.

13.Xu, Z.; Liu, Y.; Zhao, X.; Peng, L.; Sun, H.; Xu, Y.; Ren, X.; Jin, C.; Xu, P.; Wang, M.; Gao, C., Ultrastiff and Strong Graphene Fibers via Full-Scale Synergetic Defect Engineering. *Advanced Materials* 2016, 28 (30), 6449-6456.

14.Fang, B.; Chang, D.; Xu, Z.; Gao, C., A Review on Graphene Fibers: Expectations, Advances, and Prospects. *Advanced Materials* 2020, 32 (5), 1902664.

15.Li, P.; Liu, Y.; Shi, S.; Xu, Z.; Ma, W.; Wang, Z.; Liu, S.; Gao, C., Highly Crystalline Graphene Fibers with Superior Strength and Conductivities by Plasticization Spinning. *Advanced Functional Materials* 2020, 30 (52), 2006584.

16.Pan, Z. W.; Xie, S. S.; Lu, L.; Chang, B. H.; Sun, L. F.; Zhou, W. Y.; Wang, G.; Zhang, D. L., Tensile tests of ropes of very long aligned multiwall carbon nanotubes. *Applied Physics Letters* 1999, 74 (21), 3152-3154.

17. Araujo, P. T.; Terrones, M.; Dresselhaus, M. S., Defects and impurities in graphene-like materials. *Materials Today* 2012, 15 (3), 98-109.

18. Deng, S.; Berry, V., Wrinkled, rippled and crumpled graphene: an overview of formation mechanism, electronic properties, and applications. *Materials Today* 2016, 19 (4), 197-212.

19. Wang, Y.; Liu, Z., Spontaneous rolling-up and assembly of graphene designed by using defects. *Nanoscale* 2018, 10 (14), 6487-6495.

20. Zandiatashbar, A.; Lee, G.-H.; An, S. J.; Lee, S.; Mathew, N.; Terrones, M.; Hayashi, T.; Picu, C. R.; Hone, J.; Koratkar, N., Effect of defects on the intrinsic strength and stiffness of graphene. *Nature Communications* 2014, 5 (1), 3186.

21. Javvaji, B.; Budarapu, P. R.; Sutrakar, V. K.; Mahapatra, D. R.; Paggi, M.; Zi, G.; Rabczuk, T., Mechanical properties of Graphene: Molecular dynamics simulations correlated to continuum-based scaling laws. *Computational Materials Science* 2016, 125, 319-327.

22. Griffith, A. A.; Taylor, G. I., VI. The phenomena of rupture and flow in solids. *Philosophical Transactions of the Royal Society of London. Series A, Containing Papers of a Mathematical or Physical Character* 1921, 221 (582-593), 163-198.

23. Wong, E. W.; Sheehan, P. E.; Lieber, C. M., Nanobeam Mechanics: Elasticity, Strength, and Toughness of Nanorods and Nanotubes. *Science* 1997, 277 (5334), 1971-1975.

24. Yu, M.-F.; Files, B. S.; Arepalli, S.; Ruoff, R. S., Tensile Loading of Ropes of Single Wall Carbon Nanotubes and their Mechanical Properties. *Physical Review Letters* 2000, 84 (24), 5552-5555.

25. Li, Y.; Wang, K.; Wei, J.; Gu, Z.; Wang, Z.; Luo, J.; Wu, D., Tensile properties of long aligned double-walled carbon nanotube strands. *Carbon* 2005, 43 (1), 31-35.

26. Zhu, H. W.; Xu, C. L.; Wu, D. H.; Wei, B. Q.; Vajtai, R.; Ajayan, P. M., Direct Synthesis of Long Single-Walled Carbon Nanotube Strands. *Science* 2002, 296 (5569), 884-886.

27. Mittal, N.; Ansari, F.; Gowda, V. K.; Brouzet, C.; Chen, P.; Larsson, P. T.; Roth, S. V.; Lundell, F.; Wågberg, L.; Kotov, N. A.; Söderberg, L. D., Multi-scale Control of Nanocellulose Assembly: Transferring Remarkable Nanoscale Fibril Mechanics to Macroscale Fibers. *ACS Nano* 2018, 12 (7), 6378-6388.

28. Xu, Z.; Liu, Z.; Sun, H.; Gao, C., Highly Electrically Conductive Ag-Doped Graphene Fibers as Stretchable Conductors. *Advanced Materials* 2013, 25 (23), 3249-3253.

29. Aboutalebi, S. H.; Jalili, R.; Esrafilzadeh, D.; Salari, M.; Gholamvand, Z.; Aminorroaya Yamini, S.; Konstantinov, K.; Shepherd, R. L.; Chen, J.; Moulton, S. E.; Innis, P. C.; Minett, A. I.; Razal, J. M.; Wallace, G. G., High-Performance Multifunctional Graphene Yarns: Toward Wearable All-Carbon Energy Storage Textiles. *ACS Nano* 2014, 8 (3), 2456-2466.

30. Liu, S.; Wang, Y.; Ming, X.; Xu, Z.; Liu, Y.; Gao, C., High-Speed Blow Spinning of Neat Graphene Fibrous Materials. *Nano Letters* 2021, 21 (12), 5116-5125.

31. Wang, B.; Huang, M.; Kim, N. Y.; Cunniff, B. V.; Huang, Y.; Qu, D.; Chen, X.; Jin, S.; Biswal, M.; Zhang, X.; Lee, S. H.; Lim, H.; Yoo, W. J.; Lee, Z.; Ruoff, R. S., Controlled Folding of Single Crystal Graphene. *Nano Letters* 2017, 17 (3), 1467-1473.

32. Vlassiuk, I.; Polizos, G.; Cooper, R.; Ivanov, I.; Keum, J. K.; Paulauskas, F.; Datskos, P.; Smirnov, S., Strong and Electrically Conductive Graphene-Based Composite Fibers and Laminates. *ACS Applied Materials & Interfaces* 2015, 7 (20), 10702-10709.

33. Dai, Z.; Wang, Y.; Liu, L.; Liu, X.; Tan, P.; Xu, Z.; Kuang, J.; Liu, Q.; Lou, J.; Zhang, Z., Hierarchical Graphene-Based Films with Dynamic Self-Stiffening for Biomimetic Artificial Muscle. *Adv. Funct. Mater.* 2016, 26 (38), 7003-7010.

34. Yang, M.; Wang, Z.; Li, P.; Liu, Y.; Lin, J.; Wang, B.; Ming, X.; Gao, W.; Xu, Z.; Gao, C., Stress relaxation behaviors of graphene fibers. *Carbon* 2021, 182, 384-392.

35. Hwangbo, Y.; Lee, C.-K.; Kim, S.-M.; Kim, J.-H.; Kim, K.-S.; Jang, B.; Lee, H.-J.; Lee, S.-K.; Kim, S.-S.; Ahn, J.-H.; Lee, S.-M., Fracture Characteristics of Monolayer CVD-Graphene. *Scientific Reports* 2014, 4, 4439.

36. Xu, J.; Yuan, G.; Zhu, Q.; Wang, J.; Tang, S.; Gao, L., Enhancing the Strength of Graphene by a Denser Grain Boundary. *ACS Nano* 2018, 12 (5), 4529-4535.

37. Zhang, Z.; Wang, X.; Lee, J. D., An atomistic methodology of energy release rate for graphene at nanoscale. *Journal of Applied Physics* 2014, 115 (11), 114314.

Appendix B Custom micromechanical tester probe calibration

The capacitive displacement sensor can be removed and replaced with a number of different models. These models range in distance sensitivity as well as maximum and minimum operating distance. Each sensor will output a voltage that corresponds to the distance between the sensor and the cantilever. The voltage is calibrated to be zero when the displacement is in the center of the sensors range. At the maximum range between sensor and cantilever, the voltage is at its minimum value, say, -10 V. At the minimum allowable displacement, the voltage is at its maximum, 10 V. The behavior within the calibrated range is linear. With some simple algebra, we can determine the displacement that corresponds to any given voltage. From this point, we need only to determine the spring constant of the cantilevered beam. With the spring constant, we can convert the measured displacement into a force.

The measurement of the spring constant is carried out using standard, NIST traceable weights. The test rig is flipped upside-down, so that weights can be placed directly on top of the beam. As each weight is added, the displacement is measured by the capacitive sensor and is recorded. The spring behaves linearly, and the slope of the weight added versus the displacement measured is the spring constant. Typical spring constants for these custom cantilevers range from around 100 N/M up to 1000 N/m.

Bibliography

- [1] H. Procopiou, A. Boleti, R. Vargiolu, and H. Zahouani, “The role of tactile perception during stone-polishing in Aegean prehistory (5th-4th millennium B.C.),” *Wear*, vol. 271, no. 9–10, pp. 2525–2530, 2011.
- [2] A. Piltan and R. Ghodsi, *An Introduction to MEMS (Micro-electromechanical Systems) MEMS*. PRIME Faraday Partnership, 2002.
- [3] D. J. Fonseca and M. Sequera, “On MEMS reliability and failure mechanisms,” *Int. J. Qual. Stat. Reliab.*, pp. 1–7, 2011.
- [4] C. M. Huang, A. S. Sarathivasan, Y. Huang, R. Doraiswami, M. Osterman, and M. Pecht, “MEMS reliability,” *Mems Packag.*, vol. 12, no. 2, pp. 279–343, 2018.
- [5] S. N. Ramakrishna, L. Y. Clasohm, A. Rao, and N. D. Spencer, “Controlling adhesion force by means of nanoscale surface roughness,” *Langmuir*, vol. 27, no. 16, pp. 9972–9978, 2011.
- [6] S. N. Ramakrishna, P. C. Nalam, L. Y. Clasohm, and N. D. Spencer, “Study of adhesion and friction properties on a nanoparticle gradient surface: transition from JKR to DMT contact mechanics,” *Langmuir*, vol. 29, no. 1, pp. 175–182, 2013.
- [7] Z. Chai, Y. Liu, X. Lu, and D. He, “Reducing adhesion force by means of atomic layer deposition of ZnO films with nanoscale surface roughness,” *ACS Appl. Mater. Interfaces*, vol. 6, no. 5, pp. 3325–3330, 2014.
- [8] O. Laitinen, K. Bauer, J. Niinimäki, and U. A. Peuker, “Validity of the Rumpf and the Rabinovich adhesion force models for alumina substrates with nanoscale roughness,” *Powder Technol.*, vol. 246, pp. 545–552, 2013.
- [9] B. R. Radhika, N. Kumar, S. Dash, A. K. Tyagi, and I. Lin, “Anomalous Behavior of Load-Dependent Friction on Ultra-Nanocrystalline Diamond Film,” no. 9, pp. 1098–1104, 2014.
- [10] H. R. Brown, “Adhesion Between Polymers and Other Substances - A Review of Bonding Mechanisms , Systems and Testing,” *Mater. Forum*, vol. 24, pp. 49–58, 2000.
- [11] D. J. Siegel, L. G. Hector, and J. B. Adams, “Adhesion, atomic structure, and bonding at the (formula presented) interface: A first principles study,” *Phys. Rev. B - Condens. Matter Mater. Phys.*, vol. 65, no. 8, pp. 1–19, 2002.
- [12] R. C. Thomas, J. E. Houston, R. M. Crooks, T. Kim, and T. A. Michalske, “Probing Adhesion Forces at the Molecular Scale,” *J. Am. Chem. Soc.*, vol. 117, no. 13, pp. 3830–3834, 1995.
- [13] K. Viswanathan, H. Ozhalici, C. L. Elkins, C. Heisey, T. C. Ward, and T. E. Long, “Multiple

- hydrogen bonding for reversible polymer surface adhesion,” *Langmuir*, vol. 22, no. 3, pp. 1099–1105, 2006.
- [14] V. M. Muller, I. N. Aleinikova, G. I. Shcherbina, Y. P. Toporov, and B. V. Derjaguin, “The influence of contact electrification on the adhesion of dielectric elastic spheres subjected to external loads before detachment,” *Prog. Surf. Sci.*, vol. 45, no. 1–4, pp. 199–222, 1994.
- [15] Y. Wang *et al.*, “The Instability of Angstrom-Scale Head-Disk Interface Induced by Electrostatic Force,” *IEEE Trans. Magn.*, vol. 51, no. 11, pp. 1–4, 2015.
- [16] T. A. L. Burgo, C. A. Silva, L. B. S. Balestrin, and F. Galembeck, “Friction coefficient dependence on electrostatic tribocharging,” *Sci. Rep.*, vol. 3, pp. 1–8, 2013.
- [17] S. R. Waitukaitis, V. Lee, J. M. Pierson, S. L. Forman, and H. M. Jaeger, “Size-dependent same-material tribocharging in insulating grains,” *Phys. Rev. Lett.*, vol. 112, no. 21, pp. 1–5, 2014.
- [18] F. W. Delrio *et al.*, “The role of van der Waals forces in adhesion of micromachined surfaces,” *Nat. Mater.*, vol. 4, no. August, pp. 629–634, 2005.
- [19] L. Ostrovskaya, V. Perevertailo, V. Ralchenko, A. Saveliev, and V. Zhuravlev, “Wettability of nanocrystalline diamond films,” *Diam. Relat. Mater.*, vol. 16, no. 12, pp. 2109–2113, 2007.
- [20] J. A. Greenwood and J. H. Tripp, “The elastic contact of rough spheres,” *J. Appl. Mech. Trans. ASME*, vol. 34, no. 1, pp. 153–159, 1964.
- [21] B. Derjaguin, V. Muller, and Y. Toporov, “Effect of contact deformation on the adhesion of elastic solids,” *J. Colloid Interface Sci.*, vol. 53, no. 2, pp. 314–326, 1975.
- [22] K. L. Johnson, K. Kendall, and A. D. Roberts, “Surface energy and the Contact of Elastic Solids,” *Proc. R. Soc. Lond. A. Math. Phys. Sci.*, vol. 324, no. 1558, pp. 201–313, 1971.
- [23] D. Maugis, “Adhesion of spheres: The JKR-DMT transition using a dugdale model,” *J Colloid Interface Sci*, vol. 150, no. 1, pp. 243–269, 1992.
- [24] D. S. Grierson, E. E. Flater, and R. W. Carpick, “Accounting for the JKR-DMT transition in adhesion and friction measurements with atomic force microscopy,” *J. Adhes. Sci. Technol.*, vol. 19, no. 3–5, pp. 291–311, 2005.
- [25] J. A. Greenwood and J. B. P. Williamson, “Contact of Nominally Flat Surfaces,” *Proc. R. Soc. Lond. A*, vol. 295, no. 1442, pp. 300–319, 1966.
- [26] K. N. G. Fuller and D. Tabor, “The Effect of Surface Roughness on the Adhesion of Elastic Solids,” *Proc. R. Soc. Lond. A*, vol. 345, no. 1642, pp. 327–342, 1975.
- [27] D. Maugis, “On the contact and adhesion of rough surfaces,” *J. Adhes. Sci. Technol.*, vol. 10, no. 2, pp. 161–175, 1995.

- [28] A. W. Bush, R. D. Gibson, and T. R. Thomas, “The Elastic Contact of a Rough Surface,” *Wear*, vol. 35, pp. 87–111, 1975.
- [29] P. R. Nayak, “Random Process Model of Rough Surfaces,” *J. Lubr. Tech.*, vol. 93, no. 3, pp. 398–407, 1971.
- [30] B. B. Mandelbrot, D. E. Passoja, and A. J. Paullay, “Fractal character of fracture surfaces of metals,” *Nature*, vol. 308, no. 5961, pp. 721–722, 1984.
- [31] M. Ciavarella, “A very simple estimate of adhesion of hard solids with rough surfaces based on a bearing area model,” *Meccanica*, vol. 53, no. 1–2, pp. 241–250, 2018.
- [32] G. Violano and L. Afferrante, “Contact of rough surfaces: Modeling adhesion in advanced multiasperity models,” *Proc. Inst. Mech. Eng. Part J J. Eng. Tribol.*, vol. 233, no. 10, pp. 1585–1593, 2019.
- [33] J. A. Greenwood, “Reflections on and Extensions of the Fuller and Tabor Theory of Rough Surface Adhesion,” *Tribol. Lett.*, vol. 65, no. 4, pp. 1–12, 2017.
- [34] Z. Wei, M. F. He, and Y. P. Zhao, “The effects of roughness on adhesion hysteresis,” *J. Adhes. Sci. Technol.*, vol. 24, no. 6, pp. 1045–1054, 2010.
- [35] D. S. Rimai, D. J. Quesnel, and A. A. Busnaina, “The adhesion of dry particles in the nanometer to micrometer-size range,” *Colloids Surfaces A Physicochem. Eng. Asp.*, vol. 165, no. 1–3, pp. 3–10, 2000.
- [36] B. N. J. Persson and E. Tosatti, “The effect of surface roughness on the adhesion of elastic solids,” *J. Chem. Phys.*, vol. 115, no. 12, pp. 5597–5610, 2001.
- [37] F. W. DelRio, M. L. Dunn, L. M. Phinney, C. J. Bourdon, and M. P. De Boer, “Rough surface adhesion in the presence of capillary condensation,” *Appl. Phys. Lett.*, vol. 90, no. 16, 2007.
- [38] F. P. Bowden and D. Tabor, *The friction and Lubrication of Solids*. 1950.
- [39] J. F. Archard, “Single contacts and multiple encounters,” *J. Appl. Phys.*, vol. 32, no. 8, pp. 1420–1425, 1961.
- [40] M. H. Müser *et al.*, “Meeting the Contact-Mechanics Challenge,” *Tribol. Lett.*, vol. 65, no. 118, 2017.
- [41] J. H. Hafner, C. L. Cheung, A. T. Wooley, and C. M. Lieber, “Structural and Functional Imaging with Carbon Nanotube AFM Probes,” *Prog. Biophys. Mol. Biol.*, vol. 77, pp. 73–110, 2010.
- [42] Y. Ando, T. Tanaka, J. Ino, and K. Kakuta, “Relationships of Friction, Pull-off Forces, and Nanometer-scale Surface Geometry,” *JSME*, vol. 44, no. 2, pp. 453–461, 2001.

- [43] M. Götzinger, W. Peukert, M. Gotzinger, and W. Peukert, “Particle Adhesion Force Distributions on Rough Surfaces,” *Langmuir*, vol. 20, no. 20, pp. 5298–5303, 2004.
- [44] M. George and D. T. Goddard, “The characterisation of rough particle contacts by atomic force microscopy,” *J. Colloid Interface Sci.*, vol. 299, no. 2, pp. 665–672, 2006.
- [45] M. Audry, S. Ramos, and E. Charlaix, “Adhesion between highly rough alumina surfaces : An atomic force microscope study,” *J. Colloid Interface Sci.*, vol. 331, no. 2, pp. 371–378, 2009.
- [46] S. N. Ramakrishna, R. M. Espinosa-marzal, V. V. Naik, P. C. Nalam, and N. D. Spencer, “Adhesion and friction properties of polymer brushes on rough surfaces: A gradient approach,” *Langmuir*, vol. 29, no. 49, pp. 15251–15259, 2013.
- [47] Y. Xia, M. Bigerelle, J. Marteau, P. E. Mazeran, S. Bouvier, and A. Iost, “Effect of surface roughness in the determination of the mechanical properties of material using nanoindentation test,” *Scanning*, vol. 36, no. 1, pp. 134–149, 2014.
- [48] G. Carbone, E. Pierro, and G. Recchia, “Loading-unloading hysteresis loop of randomly rough adhesive contacts,” *Phys Rev E*, vol. 92, no. 6, pp. 624041–624047, 2015.
- [49] S. R. Khanal *et al.*, “Characterization of small-scale surface topography using transmission electron microscopy,” *Surf. Topogr. Metrol. Prop.*, vol. 6, no. 4, p. 045004, 2018.
- [50] T. D. B. B. Jacobs *et al.*, “The effect of atomic-scale roughness on the adhesion of nanoscale asperities: A combined simulation and experimental investigation,” *Tribol. Lett.*, vol. 50, no. 1, pp. 81–93, 2013.
- [51] W. A. Ducker, T. J. Senden, and R. M. Pashley, “Direct measurement of colloidal forces using an atomic force microscope,” *Nature*, vol. 353, pp. 239–241, 1991.
- [52] H. J. Butt, “Measuring electrostatic, van der Waals, and hydration forces in electrolyte solutions with an atomic force microscope,” *Biophys. J.*, vol. 60, no. 6, pp. 1438–1444, 1991.
- [53] G. W. Tormoen, J. Drelich, and J. Nalaskowski, “A distribution of AFM pull-off forces for glass microspheres on a symmetrically structured rough surface,” *J. Adhes. Sci. Technol.*, vol. 19, pp. 215–234, 2005.
- [54] S. N. Ramakrishna, L. Y. Clasohm, A. Rao, and N. D. Spencer, “Controlling adhesion force by means of nanoscale surface roughness,” *Langmuir*, vol. 27, no. 16, pp. 9972–9978, 2011.
- [55] T. D. B. Jacobs *et al.*, “The effect of atomic-scale roughness on the adhesion of nanoscale asperities: A combined simulation and experimental investigation,” *Tribol. Lett.*, vol. 50, no. 1, pp. 81–93, 2013.
- [56] D. Tabor and R. H. S. Winterton, “The Direct Measurement of Normal and Retarded van der Waals Forces,” *Proc. R. Soc. Lond. A. Math. Phys. Sci.*, vol. 312, no. 1511, pp. 435–

450, 1969.

- [57] J. N. Israelachvili and P. M. McGuiggan, “Adhesion and short-range forces between surfaces. part i: New apparatus for surface force measurements,” *J. Mater. Res.*, vol. 5, no. 10, pp. 2223–2231, 1990.
- [58] J. Israelachvili *et al.*, “Recent advances in the surface forces apparatus (SFA) technique,” *Reports Prog. Phys.*, vol. 73, no. 3, 2010.
- [59] G. R. Salazar-Banda, M. A. Felicetti, J. A. S. Gonçalves, J. R. Coury, and M. L. Aguiar, “Determination of the adhesion force between particles and a flat surface, using the centrifuge technique,” *Powder Technol.*, vol. 173, no. 2, pp. 107–117, 2007.
- [60] M. A. Felicetti, G. R. Salazar-Banda, J. R. Coury, and M. L. Aguiar, “Influence of particle size, applied compression, and substratum material on particle-surface adhesion force using the centrifuge technique,” *Ind. Eng. Chem. Res.*, vol. 48, no. 2, pp. 877–887, 2009.
- [61] K. K. Lam and J. M. Newton, “Influence of particle size on the adhesion behaviour of powders, after application of an initial press-on force,” *Powder Technol.*, vol. 73, no. 2, pp. 117–125, 1992.
- [62] K. K. Lam and J. M. Newton, “Investigation of applied compression on the adhesion of powders to a substrate surface,” *Powder Technol.*, vol. 65, no. 1–3, pp. 167–175, 1991.
- [63] A. Gujrati *et al.*, “Comprehensive topography characterization of polycrystalline diamond coatings,” *Surf. Topogr. Metrol. Prop.*, vol. 9, no. 9, p. 014003, 2021.
- [64] A. Gujrati, S. R. Khanal, L. Pastewka, and T. D. B. Jacobs, “Combining TEM, AFM, and Profilometry for Quantitative Topography Characterization Across All Scales,” *ACS Appl. Mater. Interfaces*, vol. 10, no. 34, pp. 29169–29178, 2018.
- [65] S. B. Vishnubhotla, R. Chen, S. R. Khanal, A. Martini, and T. D. B. Jacobs, “Understanding contact between platinum nanocontacts at low loads: The effect of reversible plasticity,” *Nanotechnology*, vol. 30, no. 3, 2019.
- [66] R. C. Voicu, R. Gavrilă, A. C. Obreja, A. M. Baracu, A. Dinescu, and R. Müller, “Design, microfabrication and analysis of polysilicon thin layers for MEMS vibrating structures,” *Analog Integr. Circuits Signal Process.*, vol. 82, no. 3, pp. 611–620, 2015.
- [67] Z. Zhou, D. Chen, X. Wang, and J. Jiang, “Milling positive master for polydimethylsiloxane microfluidic devices: The microfabrication and roughness issues,” *Micromachines*, vol. 8, no. 10, 2017.
- [68] J. Wei *et al.*, “Surface Roughness: A Crucial Factor to Robust Electric Double Layer Capacitors,” *ACS Appl. Mater. Interfaces*, vol. 12, no. 5, pp. 5786–5792, 2020.
- [69] N. I. Chkhalo *et al.*, “Ion-beam polishing of fused silica substrates for imaging soft x-ray and extreme ultraviolet optics,” *Appl. Opt.*, vol. 55, no. 6, p. 1249, 2016.

- [70] Y. Peng, B. Shen, Z. Wang, P. Yang, W. Yang, and G. Bi, “Review on polishing technology of small-scale aspheric optics,” *Int. J. Adv. Manuf. Technol.*, vol. 115, no. 4, pp. 965–987, 2021.
- [71] Y. W. Ji *et al.*, “Comparison of surface roughness and bacterial adhesion between cosmetic contact lenses and conventional contact lenses,” *Eye Contact Lens*, vol. 41, no. 1, pp. 25–33, 2015.
- [72] A. A. G. Bruzzone, H. L. Costa, P. M. Lonardo, and D. A. Lucca, “Advances in engineered surfaces for functional performance,” *CIRP Ann. - Manuf. Technol.*, vol. 57, no. 2, pp. 750–769, 2008.
- [73] B. B. Mandelbrot, *The Fractal Geometry of Nature*. W.H. Freeman and Company, 1982.
- [74] T. D. B. Jacobs, T. Junge, and L. Pastewka, “Quantitative characterization of surface topography using spectral analysis,” *Surf. Topogr. Metrol. Prop.*, vol. 5, p. 013001, 2017.
- [75] B. N. J. Persson, “Theory of rubber friction and contact mechanics,” *J. Chem. Phys.*, vol. 115, no. 8, pp. 3840–3861, 2001.
- [76] B. N. J. Persson, *Sliding Friction*. Springer-Verlag Berlin Heidelberg, 2005.
- [77] B. N. J. Persson, U. Tartaglino, O. Albohr, and E. Tosatti, “Rubber friction on wet and dry road surfaces: The sealing effect,” *Phys. Rev. B - Condens. Matter Mater. Phys.*, vol. 71, no. 3, pp. 1–8, 2005.
- [78] B. N. J. Persson and C. Yang, “Theory of the leak-rate of seals,” *J. Phys. Condens. Matter*, vol. 20, no. 31, p. 315011, 2008.
- [79] S. Dalvi, A. Gujrati, S. R. Khanal, L. Pastewka, A. Dhinojwala, and T. D. B. Jacobs, “Linking energy loss in soft adhesion to surface roughness,” *Proc. Natl. Acad. Sci. U. S. A.*, vol. 116, no. 51, pp. 25484–25490, 2019.
- [80] L. A. Thimons, A. Gujrati, A. Sanner, L. Pastewka, and T. D. B. Jacobs, “Hard-material Adhesion: Which Scales of Roughness Matter?,” *Exp. Mech.*, 2021.
- [81] B. N. J. Persson and M. Scaraggi, “Theory of adhesion: Role of surface roughness,” *J. Chem. Phys.*, vol. 141, no. 12, pp. 1–18, 2014.
- [82] B. N. J. Persson, “Contact mechanics for randomly rough surfaces,” *Surf. Sci. Rep.*, vol. 61, no. 4, pp. 201–227, 2006.
- [83] A. Wang and M. H. Müser, “On the usefulness of the height-difference-autocorrelation function for contact mechanics,” *Tribol. Int.*, vol. 123, pp. 224–233, 2018.
- [84] S. B. Ramiseti, C. Campañá, G. Anciaux, J. F. Molinari, M. H. Müser, and M. O. Robbins, “The autocorrelation function for island areas on self-affine surfaces,” *J. Phys. Condens. Matter*, vol. 23, no. 21, 2011.

- [85] A. Hariri, J. W. Zu, and R. Ben Mrad, “Modeling of dry stiction in micro electromechanical systems (MEMS),” *J. Micromech. Microeng.*, vol. 16, p. 1195, 2006.
- [86] T. Gredig, E. A. Silverstein, and M. P. Byrne, “Height-height correlation function to determine grain size in iron phthalocyanine thin films,” *J. Phys. Conf. Ser.*, vol. 417, no. 1, pp. 1–5, 2013.
- [87] R. F. Ceballos and F. F. Largo, “On The Estimation of the Hurst Exponent Using Adjusted Rescaled Range Analysis, Detrended Fluctuation Analysis and Variance Time Plot: A Case of Exponential Distribution,” no. 8, pp. 424–434, 2018.
- [88] X. Zhang, Y. Xu, and R. L. Jackson, “An analysis of generated fractal and measured rough surfaces in regards to their multi-scale structure and fractal dimension,” *Tribol. Int.*, vol. 105, pp. 94–101, 2017.
- [89] J. Schmittbuhl, J. Vilotte, and S. Roux, “reliability of self-affine measurements,” *Phys Rev E*, vol. 51, no. 1, pp. 131–147, 1995.
- [90] J. C. Gallant, I. D. Moore, M. F. Hutchinson, and P. Gessler, “Estimating fractal dimension of profiles: A comparison of methods,” *Math. Geol.*, vol. 26, no. 4, pp. 455–481, 1994.
- [91] X. Zhang, Y. Xu, and R. L. Jackson, “An analysis of generated fractal and measured rough surfaces,” *Electr. Contacts, Proc. Annu. Holm Conf. Electr. Contacts*, vol. 2016-Decem, pp. 192–197, 2016.
- [92] T. R. Thomas, *Rough Surface*. Imperial College Press; 2nd Revised ed. edition, 1999.
- [93] A. V. Oppenheim, R. W. Schaffer, and J. R. Buck, *Discrete-Time Signal Processing*. Prentice Hall, 1999.
- [94] R. Ding, A. Gujrati, M. M. Pendolino, K. E. Beschorner, and T. D. B. Jacobs, “Going Beyond Traditional Roughness Metrics for Floor Tiles: Measuring Topography Down to the Nanoscale,” *Tribol. Lett.*, vol. 69, no. 3, pp. 1–12, 2021.
- [95] L. Pastewka and M. O. Robbins, “Contact between rough surfaces and a criterion for macroscopic adhesion,” *Proc. Natl. Acad. Sci. U. S. A.*, vol. 111, no. 9, pp. 3298–3303, 2014.
- [96] P. Berthoud and T. Baumberger, “Shear Stiffness of a Solid-Solid Multicontact Interface,” *Proc. Math. Phys. Eng. Sci.*, vol. 454, no. 1974, pp. 1615–1634, 1998.
- [97] M. Benz, K. J. Rosenberg, E. J. Kramer, and J. N. Israelachvili, “The deformation and adhesion of randomly rough and patterned surfaces,” *J. Phys. Chem. B*, vol. 110, no. 24, pp. 11884–11893, 2006.
- [98] S. Akarapu, T. Sharp, and M. O. Robbins, “Stiffness of contacts between rough surfaces,” *Phys. Rev. Lett.*, vol. 106, no. 20, pp. 1–4, 2011.

- [99] M. Nosonovsky and B. Bhushan, “Biologically inspired surfaces: Broadening the scope of roughness,” *Adv. Funct. Mater.*, vol. 18, no. 6, pp. 843–855, 2008.
- [100] J. A. Greenwood and J. B. P. Williamson, “Contact of nominally flat surfaces,” *Proc. R. Soc. London. Ser. A. Math. Phys. Sci.*, vol. 295, no. 1442, pp. 300–319, 1966.
- [101] Y. I. Rabinovich, J. J. Adler, A. Ata, R. K. Singh, and B. M. Moudgil, “Adhesion between nanoscale rough surfaces. I. Role of asperity geometry,” *J. Colloid Interface Sci.*, vol. 232, no. 1, pp. 10–16, 2000.
- [102] Y. I. Rabinovich, J. J. Adler, A. Ata, R. K. Singh, and B. M. Moudgil, “Adhesion between nanoscale rough surfaces: II. Measurement and comparison with theory,” *J. Colloid Interface Sci.*, vol. 232, no. 1, pp. 17–24, 2000.
- [103] R. S. Bradley, “The cohesive force between solid surfaces and the surface energy of solids,” *London, Edinburgh, Dublin Philos. Mag. J. Sci.*, vol. 13, no. 86, pp. 853–862, 1932.
- [104] J. A. Greenwood, “Adhesion of Elastic Spheres,” *Proc. R. Soc. Lond. A*, vol. 453, pp. 1277–1297, 1997.
- [105] Y. Jiang and K. T. Turner, “Measurement of the strength and range of adhesion using atomic force microscopy,” *Extrem. Mech. Lett.*, vol. 9, pp. 119–126, 2016.
- [106] P. W. May, “Diamond thin films : a 21st-century material,” *Phil. Trans. R. Soc. Lond. A*, no. 358, pp. 473–495, 2000.
- [107] K. Turcheniuk and V. N. Mochalin, “Biomedical Applications of Nanodiamond (Review),” *Nanotechnology*, vol. 28, p. 252001, 2017.
- [108] R. Narayan, *Diamond-Based Materials for Biomedical Applications*. Woodhead Publishing, 2013.
- [109] J. Sheikh-Ahmad and J. P. Davim, *Machining Technology for Composite Materials*. Woodhead Publishing, 2012.
- [110] A. V. Sumant *et al.*, “Ultrananocrystalline diamond film as a wear-resistant and protective coating for mechanical seal applications,” *Tribol. Trans.*, vol. 48, no. 1, pp. 24–31, 2005.
- [111] O. Auciello *et al.*, “Are diamonds a MEMS’ best friend?,” *IEEE Microw. Mag.*, vol. 8, no. 6, pp. 61–75, 2007.
- [112] A. Kumar, T. Staedler, and X. Jiang, “Role of relative size of asperities and adhering particles on the adhesion force,” *J. Colloid Interface Sci.*, vol. 409, pp. 211–218, 2013.
- [113] Y. Zou, S. Jayasuriya, C. W. Manke, and G. Mao, “Influence of Nanoscale Surface Roughness on Colloidal Force Measurements,” *Langmuir*, vol. 31, pp. 10341–10350, 2015.
- [114] T. D. B. Jacobs, J. A. Lefever, and R. W. Carpick, “Measurement of the Length and Strength

- of Adhesive Interactions in a Nanoscale Silicon-Diamond Interface,” *Adv. Mater. Interfaces*, vol. 2, no. 9, pp. 1–11, 2015.
- [115] L. Pastewka and M. O. Robbins, “Contact area of rough spheres: Large scale simulations and simple scaling laws,” *Appl. Phys. Lett.*, vol. 108, no. 22, 2016.
- [116] R. H. Byrd, P. Lu, J. Nocedal, and C. Zhu, “A Limited Memory Algorithm for Bound Constrained Optimization,” *SIAM J. Sci. Comput.*, vol. 16, no. 5, pp. 1190–1208, 1995.
- [117] A. Almqvist, F. Sahlin, R. Larsson, and S. Glavatskih, “On the dry elasto-plastic contact of nominally flat surfaces,” *Tribol. Int.*, vol. 40, no. 4, pp. 574–579, 2007.
- [118] F. Pérez-Ràfols, R. Larsson, and A. Almqvist, “Modelling of leakage on metal-to-metal seals,” *Tribol. Int.*, vol. 94, pp. 421–427, 2016.
- [119] B. Weber, T. Suhina, T. Junge, L. Pastewka, A. M. Brouwer, and D. Bonn, “Molecular probes reveal deviations from Amontons’ law in multi-asperity frictional contacts,” *Nat. Commun.*, vol. 9, no. 1, pp. 1–7, 2018.
- [120] Y. Chen, H. J. Busscher, H. C. van der Mei, and W. Norde, “Statistical analysis of long- and short-range forces involved in bacterial adhesion to substratum surfaces as measured using atomic force microscopy,” *Appl. Environ. Microbiol.*, vol. 77, no. 15, pp. 5065–5070, 2011.
- [121] M. Sztilkovics *et al.*, “Single-cell adhesion force kinetics of cell populations from combined label-free optical biosensor and robotic fluidic force microscopy,” *Sci. Rep.*, vol. 10, no. 1, pp. 1–13, 2020.
- [122] P. Toliás *et al.*, “Adhesive force distributions for tungsten dust deposited on bulk tungsten and beryllium-coated tungsten surfaces,” *Nucl. Mater. Energy*, vol. 15, no. January, pp. 55–63, 2018.
- [123] T. D. B. Jacobs, C. Mathew Mate, K. T. Turner, and R. W. Carpick, “Understanding the tip-sample contact: An overview of contact mechanics from the macro- to the nanoscale,” in *Scanning Probe Microscopy for Industrial Applications: Nanomechanical Characterization*, John Wiley & Sons, Inc., 2013, pp. 15–48.
- [124] A. Krell and S. Schädlich, “Nanoindentation hardness of submicrometer alumina ceramics,” *Mater. Sci. Eng. A*, vol. 307, no. 1–2, pp. 172–181, 2001.
- [125] A. Krell and P. Blank, “Grain size dependence of hardness in dense submicronmeter alumina,” *J. Am. Ceram. Soc.*, vol. 78, pp. 1118–1120, 1995.
- [126] Y. Q. Bu, P. Wang, A. M. Nie, and H. T. Wang, “Room-temperature plasticity in diamond,” *Sci. China Technol. Sci.*, vol. 64, pp. 0–4, 2020.
- [127] I. Issa *et al.*, “Room temperature plasticity and phase transformation of nanometer-sized transition alumina nanoparticles under pressure,” *Acta Mater.*, vol. 150, no. May, pp. 308–

316, 2018.

- [128] C. H. Mastrangelo and C. H. Hsu, “Simple experimental technique for the measurement of the work of adhesion of microstructures,” *Tech. Dig. IEEE Solid-State Sens. Actuator Work.*, no. July, pp. 208–212, 1992.
- [129] A. V. Sumant, D. S. Grierson, J. E. Gerbi, J. A. Carlisle, O. Auciello, and R. W. Carpick, “Surface chemistry and bonding configuration of ultrananocrystalline diamond surfaces and their effects on nanotribological properties,” *Phys. Rev. B - Condens. Matter Mater. Phys.*, vol. 76, no. 23, pp. 1–11, 2007.
- [130] P. Atkins and J. DePaula, *physical chemistry for the life sciences*. W.H. Freeman and Company, 2006.
- [131] D. S. Grierson, J. Liu, R. W. Carpick, and K. T. Turner, “Adhesion of nanoscale asperities with power-law profiles,” *J. Mech. Phys. Solids*, vol. 61, no. 2, pp. 597–610, 2013.
- [132] M. Wang, K. M. Liechti, J. M. White, and R. M. Winter, “Nanoindentation of polymeric thin films with an interfacial force microscope,” *J. Mech. Phys. Solids*, vol. 52, no. 10, pp. 2329–2354, 2004.
- [133] A. E. Kovalev and S. N. Gorb, “Charge contribution to the adhesion performance of polymeric microstructures,” *Tribol. Lett.*, vol. 48, no. 1, pp. 103–109, 2012.
- [134] M. Feshanjerdi and A. Malekan, “Contact electrification between randomly rough surfaces with identical materials,” *J. Appl. Phys.*, vol. 125, no. 16, 2019.
- [135] T. Tang, C. Y. C. Y. Hui, and A. Jagota, “Adhesive contact driven by electrostatic forces,” *J. Appl. Phys.*, vol. 99, p. 054906, 2006.
- [136] M. P. de Boer and P. C. de Boer, “Thermodynamics of capillary adhesion between rough surfaces,” *J Colloid Interface Sci*, vol. 311, no. 1, pp. 171–185, 2007.
- [137] F. W. DelRio, M. L. Dunn, and M. P. de Boer, “Capillary adhesion model for contacting micromachined surfaces,” *Scr. Mater.*, vol. 59, no. 9, pp. 916–920, 2008.
- [138] M. Sedighi, V. B. Svetovoy, and G. Palasantzas, “Capillary-force measurement on SiC surfaces,” *Phys Rev E*, vol. 93, no. 062803, pp. 1–6, 2016.
- [139] D. J. Lacks, “Particle clouds: Frictile attraction,” *Nat. Phys.*, vol. 6, no. 5, pp. 324–325, 2010.
- [140] M. He, A. Szuchmacher Blum, D. E. Aston, C. Buenviaje, R. M. Overney, and R. Luginbühl, “Critical phenomena of water bridges in nanoasperity contacts,” *J. Chem. Phys.*, vol. 114, no. 3, pp. 1355–1360, 2001.
- [141] M. Bazrafshan, M. B. de Rooij, and D. J. Schipper, “Adhesive force model at a rough interface in the presence of thin water films: The role of relative humidity,” *Int. J. Mech.*

- Sci.*, vol. 140, pp. 471–485, 2018.
- [142] B. Regan *et al.*, “Plastic Deformation of Single-Crystal Diamond Nanopillars,” *Adv. Mater.*, vol. 32, no. 9, pp. 1–7, 2020.
- [143] G. I. Barenblatt and P. J. M. Monteiro, “Scaling laws in nanomechanics,” *Phys. Mesomech.*, vol. 13, no. 5–6, pp. 245–248, 2010.
- [144] V. M. Muller, V. S. Yushenko, and B. V. Derjaguin, “On the Influence of Molecular Forces on the Deformation of an Elastic Sphere,” *J. Colloid Interface Sci.*, vol. 77, no. 5, p. 91, 1980.
- [145] B. N. Persson, F. Bucher, and B. Chiaia, “Elastic contact between randomly rough surfaces: Comparison of theory with numerical results,” *Phys. Rev. B - Condens. Matter Mater. Phys.*, vol. 65, no. 18, pp. 1841061–1841067, 2002.
- [146] A. Kumar, T. Staedler, and X. Jiang, “Role of relative size of asperities and adhering particles on the adhesion force,” *J Colloid Interface Sci*, vol. 409, pp. 211–218, 2013.
- [147] N. Tayebi and A. A. Polycarpou, “Reducing the effects of adhesion and friction in microelectromechanical systems (MEMSs) through surface roughening: Comparison between theory and experiments,” *J. Appl. Phys.*, vol. 98, no. 7, 2005.
- [148] M. Kohzaki, K. Higuchi, S. Noda, and K. Uchida, “Tribological characteristics of polycrystalline diamond films produced by chemical vapor deposition,” *J. Mater. Res.*, vol. 7, no. 7, pp. 1769–1777, 1992.
- [149] Z. Chai, Y. Liu, X. Lu, and D. He, “Reducing Adhesion Force by Means of Atomic Layer Deposition of ZnO Films with Nanoscale Surface Roughness,” *ACS Appl. Mater. Interfaces*, vol. 6, no. 5, pp. 3325–3330, 2014.
- [150] Y. Y. Zhang, X. L. Wang, H. Q. Li, and B. Wang, “Adhesive behavior of micro/nano-textured surfaces,” *Appl. Surf. Sci.*, vol. 329, pp. 174–183, 2015.
- [151] A. Bechikh, O. Klinkova, Y. Maalej, I. Tawfiq, and R. Nasri, “Sandblasting parameter variation effect on galvanized steel surface chemical composition, roughness and free energy,” *Int. J. Adhes. Adhes.*, vol. 102, pp. 1–31, 2020.
- [152] J. J. Robles-Ruíz, V. E. Arana-Chavez, A. L. Ciamponi, J. Abrão, and L. K. Kanashiro, “Effects of sandblasting before orthophosphoric acid etching on lingual enamel: In-vitro roughness assessment,” *Am. J. Orthod. Dentofac. Orthop.*, vol. 147, no. 4, pp. S76–S81, 2015.
- [153] M. He, Z. Zhang, D. Zheng, N. Ding, and Y. Liu, “Effect of sandblasting on surface roughness of zirconia-based ceramics and shear bond strength of veneering porcelain,” *Dent. Mater. J.*, vol. 33, no. 6, pp. 778–785, 2014.
- [154] G. Degutis *et al.*, “CVD diamond growth from nanodiamond seeds buried under a thin

- chromium layer,” *Diam. Relat. Mater.*, vol. 64, no. 2016, pp. 163–168, 2016.
- [155] S.-Y. Lee and K. Anbumony, “Accurate control of remaining resist depth for nanoscale three-dimensional structures in electron-beam grayscale lithography,” *J. Vac. Sci. Technol. B Microelectron. Nanom. Struct.*, vol. 25, no. 6, p. 2008, 2007.
- [156] I. Khazi, U. Muthiah, and U. Mescheder, “3D free forms in c-Si via grayscale lithography and RIE,” *Microelectron. Eng.*, vol. 193, no. September, pp. 34–40, 2018.
- [157] M. R. Houston, R. T. Howe, and R. Maboudian, “Effect of hydrogen termination on the work of adhesion between rough polycrystalline silicon surfaces,” *J. Appl. Phys.*, vol. 81, no. 8, pp. 3474–3483, 1997.
- [158] D. Gao, C. Carraro, R. T. Howe, and R. Maboudian, “Polycrystalline silicon carbide as a substrate material for reducing adhesion in MEMS,” *Tribol. Lett.*, vol. 21, no. 3, pp. 226–232, 2006.
- [159] C. H. Mastrangelo and C. H. Hsu, “A simple experimental technique for the measurement of the work of adhesion of microstructures,” *Tech. Dig. IEEE Solid-State Sens. Actuator Work.*, pp. 208–212, 1992.
- [160] E. J. Thoreson, J. Martin, and N. A. Burnham, “The role of few-asperity contacts in adhesion,” *J Colloid Interface Sci*, vol. 298, no. 1, pp. 94–101, 2006.
- [161] L. J. Vandeperre, F. Giuliani, S. J. Lloyd, and W. J. Clegg, “The hardness of silicon and germanium,” *Acta Mater.*, vol. 55, no. 18, pp. 6307–6315, 2007.